Towards calibrating stellar population models in the near-IR: clues from globular clusters and early-type galaxies

Mariya Lyubenova

München 2009

Towards calibrating stellar population models in the near-IR: clues from globular clusters and early-type galaxies

DISSERTATION

an der Fakultät für Physik
der Ludwig-Maximilians-Universität

zur Erlangung des Grades
Doktor der Naturwissenschaften
Dr. rer. nat.

vorgelegt von

Mariya Boyanova Lyubenova
aus
Sofia, Bulgarien

München, Januar 2009

1st referee:	Prof. Dr. Ralf Bender
2nd referee:	Priv. Doz. Dr. Achim Weiss
Day of oral examination:	21 January 2009

Abstract

This thesis presents a study of the near-IR spectral properties of six globular clusters (GCs) and 21 early-type galaxies in the local Universe, 10 of which are in low density environments and 11 are in the Fornax cluster of galaxies. Our observations were acquired using integral field unit (IFU) and long-slit spectrographs. The common goal of the various projects was to verify the predictions of current stellar population models in the near-IR using GCs and early-type galaxies data. We provide the first spectral library of the integrated near-IR light of globular clusters with ages ≥ 1 Gyr.

Using VLT/SINFONI we obtained integrated luminosity weighted spectra of six GCs in the Large Magellanic Cloud (LMC). Three of them are old (≥ 10 Gyr) and metal poor ([Z/H] $\sim$ –1.4), the other three have intermediate ages ($1 <$ age < 3 Gyr) and higher metallicity ([Z/H] $\sim$ –0.4). We have measured the strength of the near-IR K-band features Na I, Ca I and ^{12}CO (2–0) and compared the D_{CO} index, used to measure the strength of ^{12}CO (2–0), with the predictions of the stellar population models of Maraston (2005). We find reasonable agreement between the data and the model predictions for old and metal poor GCs. For intermediate age and half solar metallicity GCs we find a marked disagreement with the models. While the models predict an increase of the index with younger ages, we find a strong drop of index strength at ~ 1 Gyr. We consider that this is due to the different spectral properties of galactic carbon rich AGB stars, used to empirically calibrate the models, and the ones present in LMC globular clusters. This conclusion is based on the different D_{CO} index strength that we measure for the carbon stars in our LMC sample and the galactic carbon stars for a given $(J - K)$ colour.

Our study of early-type galaxies in low density environments and in the Fornax cluster reveals that the near-IR Na I and D_{CO} indices follow similar index-σ scaling relations as optical metallicity indices. The Na I index shows a good positive correlation with the metallicity at old ages and additionally increases for younger ages in contrast to the behaviour of optical metal indices. We derive an empirical calibration for the Na I index as function of metallicity and suggest that a diagnostic diagram, based on the optical Hβ index and the near-IR Na I index, will be a good age-metallicity estimator once more detailed SSP models in the near-IR become available. The D_{CO} index exhibits similar trends with metallicity, albeit with a shallower slope and more complex behaviour at young ages. We find evidence of saturation of the D_{CO} index above twice solar metallicity.

Utilising the superb spatial resolution of adaptive optics assisted IFU observations in the near-IR we observed the centre of the Fornax cD galaxy NGC 1399. We confirm the presence of a central velocity dispersion drop within $r \leq 0\farcs2$ and reveal drops in

the Na I and D_{CO} index with the same extent and location. We suggest that the centre of NGC 1399 harbours a cold subsystem with a distinct stellar population, which is either more metal poor, or younger and more metal poor than the main body of the galaxy. We detect a negative gradient of the Na I index within $r \leq 1\farcs4$. Using our calibration of Na I vs. metallicity we derive a metallicity gradient, which appears to be shallower than the typical metallicity gradients measured at larger radii in other early-type galaxies.

Zusammenfassung

Das Thema dieser Dissertation ist eine spektrale Studie im nahen Infrarotbereich von sechs Kugelsternhaufen und 21 Galaxien frühen Typs, davon 10 Feldgalaxien und 11 Galaxien des Fornax Galaxienhaufens. Die Beobachtungen wurden mit einem Flächen-Spektrographen und einem Spaltspektrographen ausgeführt. Das Ziel der verschiedenen Projekte dieser Studie ist die Überprüfung der Vorhersagen von stellaren Entwicklungsmodellen. In dieser Arbeit wird der erste Katalog von integrierten, alten (≥ 1 Gyr) Kugelsternhaufenspektren im nah-infraroten Spektralbereich veröffentlicht. Mit Hilfe des Flächen-Spektrographens SINFONI am Very Large Telescope (VLT) wurden integrierte Spektren von sechs Kugelsternhaufen in der großen magellanschen Wolke (GMW) beobachtet. Von diesen gehören drei zur alten (≥ 10 Gyr) und metallarmen ([Z/H] $\sim$ –1.4) Population, die anderen drei haben ein mittleres Alter (1 - 3 Gyr) und sind metallreicher ([Z/H] $\sim$ –0.4). Die Stärke der Na I, Ca I und ^{12}CO (2–0) Absorptionslinien im K-Band wurde bestimmt und der D_{CO} Linienindex wurde mit Modellvorhersagen von Maraston (2005) verglichen. Die Beobachtungen der alten und metallarmen Kugelsternhaufen zeigen eine akzeptable Übereinstimmung mit den Modelvorhersagen. Die Kugelsternhaufen mittleren Alters weichen jedoch stark von den Modellen ab. Während die Modelle einen Anstieg des Indexes voraussagen, wird jedoch ein markanter Abfall des Indexes bei einem Alter von ~1 Gyr beobachtet. Dies wird auf die Unterschiede zwischen den in den Modellen verwendeten Spektren kohlenstoffreicher AGB Sterne und denen in Kugelsternhaufen der GMW vorkommenden zurückgeführt. Diese Aussage basiert auf der Beobachtung, dass galaktische und GMW Kohlenstoffsterne bei gleicher ($J - K$) Farbe verschiedene D_{CO} Index-Stärken zeigen. Die Beobachtungen von frühen Feldgalaxien und Fornax Haufengalaxien zeigen, dass die Na I und D_{CO} Indizes ähnlichen Index-σ Relationen folgen wie Metallindizes im optischen Wellenlängenbereich. Der Na I Index zeigt eine hervorragende, positive Korrelation mit der Häufigkeit von Metallen für alte Galaxien; im Gegensatz zu Metallindizes im optischen Bereich steigt der Na I Index mit abnehmendem Alter der Galaxie an. Es wird eine empirische Eichung des Na I Index als Funktion der Häufigkeit von Metallen beschrieben und ein Zweiindex-Diagramm aus dem optischen Hβ Index und dem nah-infraroten Na I Index zur Alters und Metallizitätsbestimmung vorgeschlagen. Der D_{CO} Index als Funktion der Metallizität zeigt ein ähnliches Verhalten, jedoch mit einer deutlich schwächeren Abhängigkeit und auch mit einem komplexeren Verhalten bei jüngerem Alter der Galaxie. Es gibt Anhaltspunkte für eine Saturierung des D_{CO} Index oberhalb doppelt solarer Metallizität. Die zentrale Galaxie des Fornax Haufens wurde mit einem Flächen-Spektrographen beobachtet, wobei durch adaptive Optik eine exzellente räumliche Auflösung erreicht wurde. Die Existenz eines zentralen Minimums in der Geschwindigkeitsdispersion für $r \leq 0\farcs2$ wird bestätigt und Minima der Na I und D_{CO} Indizes über denselben räumlichen Bereich festgestellt. Ein Szenario in dem der Galaxienkern aus einem kalten, entweder metallarmen oder metallarmen und jüngeren Untersystem besteht wird als Erklärung vorgeschlagen.

Contents

Chapter 1

Introduction

The main topic of this thesis are the near-IR spectral properties of integrated stellar populations in the nearby Universe, the use of stellar population models to derive estimates of the ages and metallicities, and the empirical calibration of population models in the near-IR. In this introduction we give a brief description of the current techniques of exploring stellar populations and some of the problems they meet. In the beginning of each Chapter of the thesis we give a further, more detailed introduction to the topic.

1.1 Galaxies – the building blocks of the visible Universe

The quest for the galaxies has begun in 1755, when the German philosopher Immanuel Kant suggested that the Milky way was a disk of stars and expanded his hypothesis further to the other nebulae, suggesting that they are also similar disks of stars. After Edwin Hubble's work in the 1930's, we know that these nebulae are indeed distant assemblies of stars, showing a bewildering variety of shapes and structures. However, the question how these systems have formed and evolved still remains open.

Edwin Hubble ordered the galaxies he saw through the telescope in a classification scheme (Hubble 1936, see Figure 1.1). To the left hand side of his famous "tuning fork" diagram he placed the elliptical galaxies (E), ordered by increasing ellipticity. They were followed by two branches of spiral galaxies, one ordinary (S) and one with barred spirals (SB). The connecting class were the lenticular galaxies (S0). This classification scheme was initially considered to have an evolutionary meaning. The arrow of time was directing from left to the right: from almost circular ellipticals to widely open spirals. Later more sophisticated diagrams became available, based on the physical parameters of the galaxies (e.g. Kormendy & Bender 1996), however Hubble's diagram is still the most commonly used when classifying galaxies, based on their morphology.

When viewed from its evolutionary side, this diagram is no longer reflecting our understanding of galaxy evolution. For example, there is evidence that large elliptical galaxies have formed through the merger of other (possibly spiral) galaxies (e.g. Toomre 1977; Schweizer 1989; Kauffmann et al. 1993; Steinmetz & Navarro 2002). However, for historical reasons, we still name as early-type galaxies those with elliptical and lenticular shape, and as late-type the spirals. The former are thought to bear the fos-

sil record of the formation and the evolution of structures in the Universe. The latter exhibit complex and still ongoing star formation. Throughout this thesis we will focus on the galaxies of early types and explore their properties using near-IR spectroscopy.

1.2 The stellar content of nearby early-type galaxies

There are two main approaches for studying galaxy formation and evolution. The first one is to explore the properties of early-type galaxies at low redshift. Their evolutionary history is imprinted on the stellar populations, their kinematics and dynamical state, like a fossil record. The second approach is to use the limit of the speed of light as a time machine and probe different stages of the evolution *in situ*, by taking snapshots of the earlier evolutionary phases, through observations of distant galaxies.

In this thesis we used the first approach – to explore nearby early-type galaxies, by means of their present stellar populations. In the last decades this search was mainly performed in the optical wavelength window, due to the availability of the needed instrumentation. But even with the appearance of 8 m-class telescopes and the Hubble Space Telescope, the majority of the galaxies, almost all outside of the Local Group, remain still unresolvable. Thus we have to rely only on their integrated light. Significant progress has been made with the development of the evolutionary population synthesis models (EPS) (e.g. Tinsley & Gunn 1976; Worthey 1994; Bruzual & Charlot 2003; Maraston 2005). This technique allows us to model the spectrophotometric properties of stellar populations, using knowledge about the stellar evolution.

The simplest approach to the EPS models is the simple stellar population (SSP). With SSPs we describe populations of stars which share the same chemical composition and age (e.g. Renzini 1981). By matching the strength of carefully selected combinations of features in the observed galaxy spectra, or integrated colours, to the output of the EPS codes, one can derive estimates of stellar population properties such as ages, metallicities, stellar mass functions, etc. But still many of the results remain uncertain, due to the fact that in the optical light the contribution from several important stellar evolutionary stages is almost equal. For example, the integrated colours and spectral features of an old and metal poor population are similar to those of a younger and metal rich population. This is called age-metallicity degeneracy. Significant efforts have been made in the last decade towards resolving this issue (e.g. Worthey et al. 1994). Today the interpretation of the integrated light of early-type galaxies benefits from the identification of optical spectral features, whose strength depends mainly on the age of the stellar population, like Hβ, or mainly on the chemical composition, like Mg and Fe lines. A whole system of optical spectral indicators, the Lick/IDS indices (Burstein et al. 1984), has been developed. Using it, major results have been achieved in determining the evolutionary history of early-type galaxies (e.g. Kuntschner & Davies 1998; Trager et al. 2000; Kuntschner et al. 2001; Thomas et al. 2005). Further progress has been achieved by including the effects of non-solar element abundance ratios (e.g. Trager et al. 2000; Kuntschner 2000; Thomas et al. 2003, 2004; Schiavon 2007). However, most age sensitive spectral indicators are also influenced by the metallicity, and vice versa. Possible exceptions are

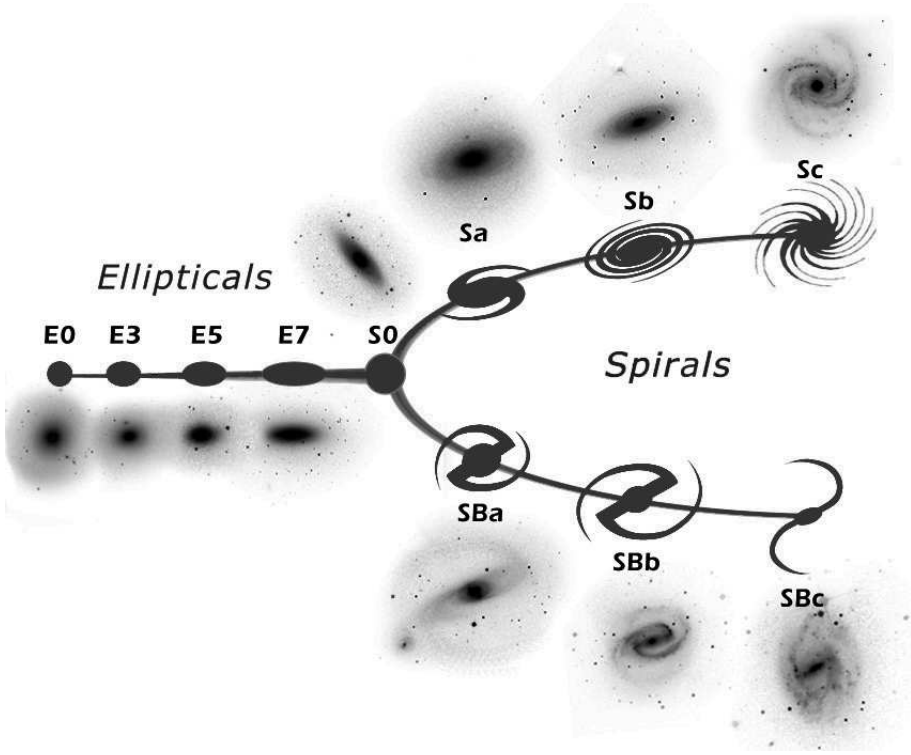

Figure 1.1: Edwin Hubble's tuning fork diagram, used to classify galaxies. Image credits: STScI

high S/N indicators such as Hγ_{HR} (Vazdekis & Arimoto 1999). There is a need of new indicators, which react only to one parameter of the stellar population, with no or insignificant contribution from the others.

The near-IR wavelength range offers a new insight into the evolutionary paradigm. The *K*-band light of stellar populations with ages between 0.3 and 2 Gyr is dominated by one single component, thermally pulsating stars on the asymptotic giants branch (TP-AGB) (Maraston 2005). For populations with age ≥ 3 Gyr the near-IR light is dominated by stars on the red giant branch (RGB). Their contribution stays approximately constant over large time scales (Maraston 2005). By isolating the spectrophotometric signature of these stellar evolutionary phases one can hope to gain a better understanding of the properties of the integrated stellar populations. This knowledge is of paramount importance for the study of high redshift galaxies, close to the times when the major star-formation has occurred. The earliest attempts to systematically qualify and quantify the near-IR spectral properties of a sample of early-type galaxies date back to the late 1990's (e.g. Mobasher & James 1996, 2000; James & Mobasher 1999, 2000, see also Frogel et al. (1978) for narrow band imaging study). Recent studies of early-type galaxies in the local Universe have shown that some near-IR indices react to the presence of young (0.2 – 3 Gyr) stars (Silva et al. 2008). Mármol-Queraltó et al. (2008) have shown that the deep absorption feature at 2.3 μm, caused by the CO molecule in the stellar atmospheres, is dependant on the metallicity. However, the interpretation of these results clearly awaits the predictions of more sophisticated EPS models.

Presently they still have the largest uncertainties in the near-IR, due to the lack of well calibrated spectral libraries.

1.3 Calibrating stellar population models

The modern stellar population models are constructed by either using the isochrone synthesis technique, or the fuel consumption approach.

In the isochrone synthesis technique the properties of the stellar population are determined by summing up the flux, contributed by stars with different masses, which populate a given isochrone. The majority of the today available stellar population models use this approach (e.g. Vazdekis et al. 1996; Fioc & Rocca-Volmerange 1997; Bruzual & Charlot 2003). To build such models there is a need for large spectral libraries of stars, from which one determines how the spectral energy distribution (SED) depends on parameters like stellar effective temperature, gravity and metallicity. Then this information is coupled with theoretical stellar evolutionary isochrones and stellar flux distribution to produce the SED of the model population. This method produces stellar population models, which are tuned to the specific chemistry and star formation history of the Milky Way, because it relies on the spectral properties of stars in our galaxy. It has been shown that massive early-type galaxies exhibit an enhanced abundance of the α-elements (O, Ne, Mg, Si, S, Ca, and Ti) over iron, as compared to the Milky Way (e.g. Worthey et al. 1992). A possible way to overcome the α-enhancement in the models is to use theoretical stellar spectra, which are computed for different α/Fe ratios (e.g. Coelho et al. 2005; Munari et al. 2005; Brott & Hauschildt 2005). The advantage is that one can explore the synthetic spectra at any spectral resolution and they do not suffer from limitations in the signal to noise ratio. However, other limitations, like uncertainties in the model atmosphere calculations, exist. Stellar population models involving synthetic stellar spectra have already been produced. (e.g. González Delgado et al. 2005; Zhang et al. 2005; Coelho et al. 2007).

In the alternative method the fuel consumption theorem (Renzini & Buzzoni 1986) is used to evaluate the flux contributions of post main sequence (PMS) stars. Such models are the ones computed by Buzzoni (1989) and Maraston (1998, 2005). The "fuel" is the amount of hydrogen and helium, which is consumed through nuclear burning in the different stellar phases. This method has several advantages, the most important of which is the inclusion of some important, but theoretically less well known stellar evolutionary phases, like the TP-AGB phase. This phase is much more difficult to include in the spectral synthesis method, because the complete stellar tracks are not available, due to difficulties in theoretical modelling of mass-loss, third dredge-up, and thermal pulses (e.g. Cassisi et al. 2001). When using the fuel consumption approach the PMS phases are linked to the main sequence phase with analytical relations, which enables the inclusion of the former after calibrating them with observations. The TP-AGB stars are particularly important for the study of stellar populations in the near-IR, where their contribution can reach up to 40 % of the total K-band light (e.g. Maraston 2005).

Whatever approach one uses for the computation of theoretical stellar population

SEDs, large and well calibrated stellar spectral libraries are needed, containing stars at different evolutionary stages and with different chemical composition. When calibrating and checking the predictions of the models a shortcut can be taken by observing globular clusters (GCs). Stars do not form in isolation, but in large complexes, and thus all of them share the same initial chemical composition and age. Their evolution is controlled by their initial mass. The GCs are the closest counterparts in the nature of the theoretical simplifications, called SSPs.

Globular clusters in the local Universe are unique laboratories to explore the evolution of stellar populations. The large advantage they offer is that with current instruments we are able to resolve their constituting stars and thus obtain detailed information on their age and chemical composition. This is the most direct way to calibrate reliably the SSP models. It has been shown to be very effective in the optical wavelength range (e.g. Puzia et al. 2005). However, recent studies have shown that globular clusters may not be as simple as we expect them to be. For example Anderson (1997) and Bedin et al. (2004) have shown the existence of a double main sequence in the Galactic globular cluster ω Centauri. Deep colour-magnitude diagrams have revealed multiple stellar populations in a number of GCs in the LMC (e.g. Bertelli et al. 2003; Mackey et al. 2008; Milone et al. 2008). The star formation history of the secondary and possible tertiary stellar populations is not clear yet. According to their chemical composition, they are considered to originate from material expelled from the first generation of stars via AGB winds or type II supernovae explosions (e.g. Ventura et al. 2002; D'Ercole et al. 2008), or from material, pre-processed in massive, rapidly rotating stars (e.g. Decressin et al. 2007). Other processes, which transform the initial globular clusters also exist. For example Kruijssen & Lamers (2008) show that the preferential loss of low-mass stars (due to mass-segregation) affects cluster photometry and mass-to-light ratio evolution.

Such effects cannot be neglected when calibrating future stellar population models with GCs data. However, until a better understanding of these phenomena becomes available, we will not be able to fully understand their influence on the final SEDs. Globular clusters in the local Universe still remain the best available empirical approximation for a SSP and throughout this thesis we will not discuss further complications, caused by e.g. multiple stellar populations or star losses.

1.4 A 3D view of the stellar populations in the local Universe

We can use the fossil record of the galaxy formation and evolution, conserved in the integrated stellar population properties, to test different galaxy formation scenarios. For example in the classical monolithic collapse models (e.g. Larson 1974; Carlberg 1984), stars form during the collapse, while gas dissipates to the centre of the galaxy, being continuously enriched by the evolving stars. Dissipative collapse therefore predicts strong negative metallicity gradients that correlate with galaxy mass (e.g. Chiosi & Carraro 2002; Kawata & Gibson 2003), negative or positive α-element enhancement gradients (e.g. Pipino et al. 2008), and small positive age gradients due to

the speed of the collapse (e.g. Thomas 1999). Within the framework of the hierarchical ΛCDM models (e.g. Cole et al. 2000; Bower et al. 2006; De Lucia et al. 2006) massive elliptical galaxies are created by mergers. Earlier simulations suggest that this would lead to erasing or diluting metallicity gradients (e.g. White 1980). Also the dissipation of gas towards the centre of the merger remnant could trigger star formation in the core and create age gradients (e.g. Barnes & Hernquist 1991; Mihos & Hernquist 1994)

Traditionally, for the studies of the radial gradients in early-type galaxies long-slit spectroscopy has been used (e.g. Gorgas et al. 1990; Carollo et al. 1993; Norris et al. 2006; Sánchez-Blázquez et al. 2006; Reda et al. 2007). However, this technique explores just a small fraction of the galaxy light, since the data depend on the slit orientation and width and have only one spatial dimension. With the fast development of Integral Field Unit (IFU) spectrographs a completely new window for the exploration of the full 2-dimensional galaxy properties has opened up. Stellar population gradients, as well as kinematic disturbances, can be identified just in one go. A good example for the power of this observational technique is given by the SAURON project (Bacon et al. 2001; de Zeeuw et al. 2002). Using spatial maps of the strength of the optical Hβ, Fe, and Mg lines Kuntschner et al. (2006) have shown that the early-type galaxies in their sample have generally negative gradients of the metallicity indicators and typically flat maps of the Hβ line.

Another strength of the IFUs in resolving spatially early-type galaxies is revealed when coupled with adaptive optics (AO). Current technologies allow for the best correction of the Earth's atmosphere smearing effect when observing in the near-IR. The VLT instrument SINFONI (Eisenhauer et al. 2003; Bonnet et al. 2004), used to obtain the majority of the data for this thesis, collects data in the near-IR spectral wavelength region. Although its field-of-view (FoV) is not very large ($8'' \times 8''$ in the largest setup), it provides an adjustable spatial scale, which can be as small as $0.''025$ per spatial slice (the resulting FoV is then $0.''8 \times 0.''8$). Such resolving power until recently was only accessible to the HST. Despite the limitations of the small FoV, this instrument is very well suited for the exploration of compact systems, such as the central regions of nearby galaxies and their globular clusters. We can also study the kinematics and the stellar populations within the sphere of influence of the super massive black holes in the most massive early-type galaxies. It offers the possibility to test the predictions of the theories of galaxy formation and evolution to the very centres of the early-type galaxies, by exploring their metallicity and age gradients. To obtain this information once more the need of good stellar population models in the near-IR is implied.

1.5 Aims and outline of this thesis

With this thesis we have set up the goal to study the near-IR spectrophotometric properties of the stellar populations in a variety of globular clusters and galaxies in the local Universe by means of integral field and long slit spectroscopy. Using our findings and integrated spectral libraries we are going to test the predictions of current stellar population models in the near-IR wavelength range.

In Chapter 2 we give an outline of the technique of integral field spectroscopy, its

specifications in the near-IR, and describe SINFONI, the instrument with which the majority of the data for this thesis were acquired.

In Chapter 3 we provide the definitions of various line strength indices in the near-IR *K*-band and explain the measurement procedures. There we also explain the different problems one may have when calibrating indices to a common system and the corrections, which have to be applied before an index value is ready for scientific analysis.

Chapter 4 is dedicated to the analysis of the integrated spectra of six globular clusters in the Large Magellanic Cloud – an irregular galaxy in the Local Group with half solar metallicity. The aim of this project is to empirically study the behaviour of the near-IR spectral indices, described in Chapter 3, as a function of the age and the metallicity of the clusters. These spectra are the first self-consistent data set of spectra of simple stellar populations, as the globular clusters are, in the near-IR and can serve as calibrators for stellar population models. We use them to test the predictions of current stellar population models, by means of line strength indices, and explore the possible reasons for disagreements.

In Chapter 5 we study the near-IR central spectral properties of a sample of early-type galaxies in low density environments, obtained using long slit spectroscopy. There we explore the dependencies of different line strength indices from the central velocity dispersion of the galaxies, as well as optical to near-IR index diagrams and their interpretation. We also compare our data with literature data for Fornax cluster early-type galaxies and search for common trends, which may lead to a better understanding of the main drivers of near-IR spectral indices.

Chapter 6 reveals the nuclear properties of the central giant elliptical galaxy in the Fornax cluster, NGC 1399. With the help of our adaptive optics assisted integral field spectroscopy we investigate the two dimensional kinematics within the sphere of influence of the super massive black hole, found in its nucleus. Using our knowledge from Chapter 4 and 5 about the dependence of near-IR line strengths on the age and the metallicity of the population, we explore the cold subsystem, found in the nucleus of NGC 1399.

Finally, in Chapter 7 we summarise our findings about the near-IR spectroscopic properties of globular clusters and early-type galaxies in different environments and discuss their application to the calibration of stellar population models. We also refer to our on-going and future projects, aiming at a better understanding of the formation and evolutionary mechanisms of early-type galaxies.

The work presented in this thesis was undertaken between September 2005 and November 2008 whilst the author was a research student under the supervision of Dr. Harald Kuntschner and Dr. David R. Silva in the European Southern Observatory and the International Max Planck Research School on Astrophysics at the Ludwig-Maximilians-Universität Munich.

The majority of the work contained in this thesis is the authors own. All observations with VLT/SINFONI have been acquired in service mode (Prop. ID 078.B-0205(A), PI H. Kuntschner and SINFONI Science Verification). The observations of the field galaxies discussed in Chapter 5 have been obtained by David R. Silva. The long-

slit spectra of early-type galaxies in the Fornax cluster were originally published in Silva, Kuntschner, & Lyubenova (2008) and were kindly provided by Harald Kuntschner. The measurements of the velocity profile of NGC 1399 presented in Section 6.3.1 were obtained using the pPXF code written by Michelle Cappellari. The line strengths measurements and velocity dispersion corrections programs, which we used throughout this thesis, are based on codes written by Harald Kuntschner.

Chapter 2

Near-IR 3D spectroscopy with SINFONI

2.1 SINFONI – instrument description

Behind the abbreviation SINFONI stands the name of the **S**pectrograph for **IN**tegral **F**ield **O**bservations in the **N**ear **I**nfrared (Eisenhauer et al. 2003; Bonnet et al. 2004). This integral field unit (IFU) is mounted in the Cassegrain focus of Unit Telescope 4 (Yepun) on VLT at Paranal La Silla Observatory. Its gratings are in the near-IR spectral domain (1 – 2.5 μm) and cover the *J*, *H* and *K*-bands, plus an additional grating, covering both *H* and *K*-bands. This instrument allows us to simultaneously obtain spectroscopy over a continuous field of view through one of the four gratings, which leads to a spectrum for each spatial pixel (or spaxel, as often called in the IFU community). Later from these spectra one can reconstruct an image of the object under study.

This IFU instrument uses the image slicing technique, which means that the image in the focal plane of the telescope is sliced into slitlets with the help of mirrors. In the case of SINFONI there are 32 slitlets. After this the light from the slitlets is realigned to form a pseudo-slit and dispersed in multiple spectra. Each slitlet is imaged over 64 pixels on the detector. Thus one obtains $32 \times 64 = 2048$ spectra of the imaged region on the sky. A schematic outline of the light path in the instrument is shown on Figure 2.1. The instrument is equipped with a Hawaii 2RG (2k×2k) detector. Each wavelength band is fitting fully on its 2048 pixels.

The spatial scale of the SINFONI observations is adjustable. One can choose between three spatial samplings: 0.″25, 0.″1 and 0.″025 per spatial pixel, resulting in a field-of-view (FoV) of 8″ × 8″, 3″ × 3″ and 0.″8 × 0.″8, respectively. The data, presented in this thesis and obtained with SINFONI, were collected with two different spatial scales. For the observations of globular clusters in the Large Magellanic Cloud we used the 0.″25 scale to achieve higher spatial coverage. For the giant elliptical galaxy in the Fornax cluster, NGC 1399, we used the 0.″1 scale with the aim of achieving better spatial sampling, since in this case we are interested in the small scale properties in the centre of the galaxy.

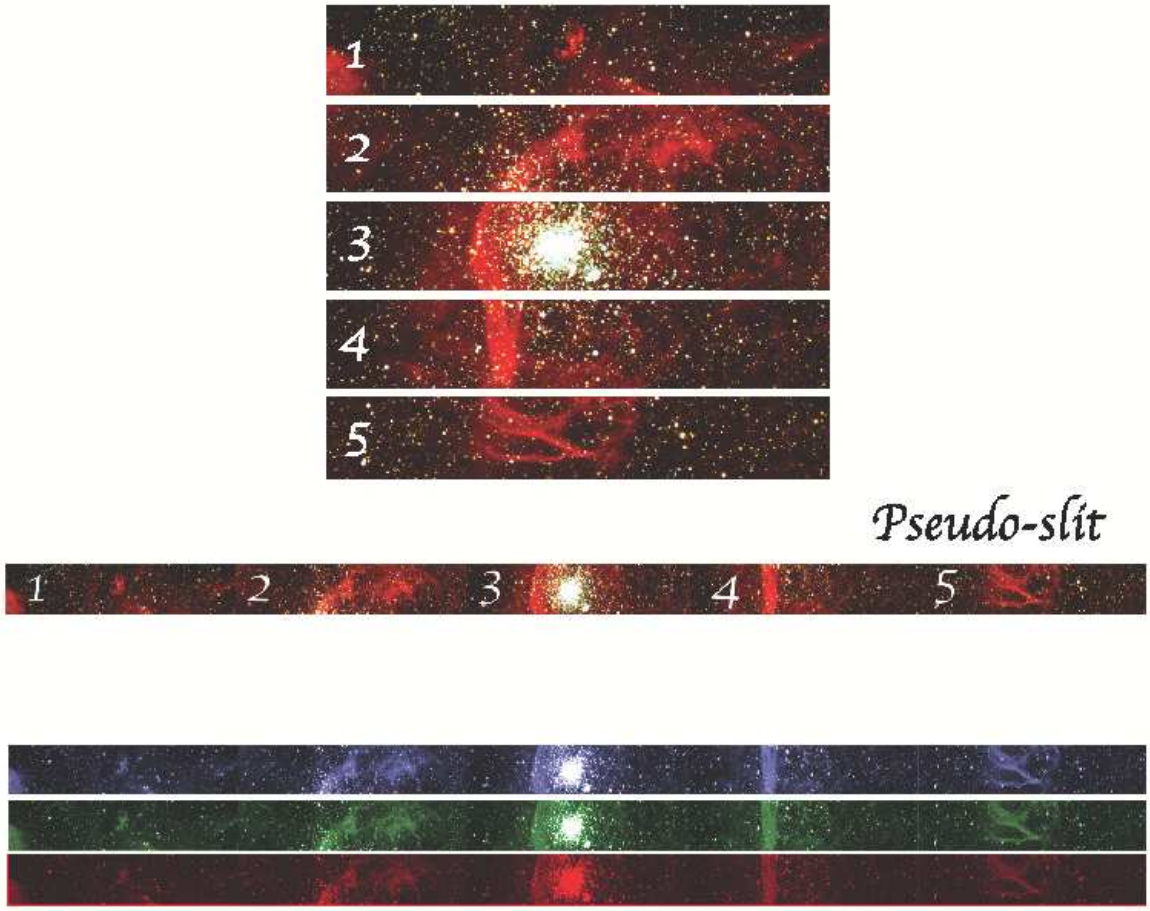

Figure 2.1: Overview of the image slicing technique. The top picture shows how the Large Magellanic Cloud cluster NGC 1850 would look like, divided into slices by the SINFONI image slicer. After that the slices are realigned to form a pseudo-slit and dispersed to form spectra. During data reduction the image is reconstructed with the help of a software (see also Figure 2.2). NGC 1850 was observed with VLT/FORS1. The picture used here is a colour composite from *B*, *V* and *Hα* filters. (NGC 1850 image credits – ESO.)

2.2 Adaptive optics

The diffraction limited resolution of the VLT is 0.″057 at a wavelength of 2.2 μm. But the observed resolution is severely affected by the atmospheric turbulence and easily can reach $\sim$ 1″ and more. The real strength of SINFONI is revealed when using the Adaptive Optics (AO) module. Its purpose is to correct the smearing effect of the unstable Earth's atmosphere and thus give us more detailed and sharper images of the object under study.

In Natural Guide Star (NGS) mode the AO correction is performed with the help of a natural star. Ideally, this star should be as close as possible to the science target, usually less then 10″ away and bright, with R-band magnitude less than 14^m. If the target itself is bright enough and peaked enough, it can also serve as an AO reference object. Modest AO corrections are still possible with stars located at up to 30″ away and having $R \sim 17^m$, but then the success of the correction is very much dependent from the natural seeing. In case of good observing conditions and the availability of a nearby and bright AO reference star, the resulting point spread function (PSF) will be very close to the diffraction limit of the telescope. A very good correction in the K-band has a Strehl ratio $\sim$ 30%.[1]

This mode, however, limits the amount of targets one can observe and obtain spatially detailed spectroscopy, because it is strongly dependent on the existence of nearby bright reference star. To overcome this limitation, recently SINFONI was equipped with a sodium laser. In the Laser Guide Star (LGS) mode the AO reference object is an artificial star, created by the laser. Due to the brightness of the artificial star, $V \sim 11^m$, and its proximity to the centre of the target, the probability of getting a minimum correction of at least 25 % Strehl ratio in the K-band increases to 65 % in contrast with nearly 3 % probability with NGS. However there are some physical limitations to the performance of the LGS. Since the artificial star is created at a relatively low altitude, $\sim$ 90 km above the ground, the light, which reaches the telescope has a conical shape and travels trough different turbulent layers than the one, originating from the science target. This effect, called the Cone Effect, leads to an error in the phase estimation. It is responsible for the saturation of the AO correction at $\sim$ 45% in the K-band.

Observations without an adaptive optics correction are also possible with SINFONI. In this case the spatial resolution of the observations is limited by the natural seeing.

2.3 3D data cubes

The output data format of SINFONI records both spatial and spectral dimensions. For each spatial pixel (spaxel) the spectrum is recorded, therefore giving the third dimension to the data. This is then referred to as 3D spectroscopy. The X and Y axis of the data cube store the spatial information, right ascension and declination, or the image of the object under study. Along the third axis we have a spectrum for each spatial pixel.

[1] The Strehl ratio is used to indicate the image quality in the case of aberrations of the light wavefront. Its definition is: the ratio of peak diffraction intensities of an aberrated versus a perfect wavefront.

The advantage of the data cube is that a variety of data analysis techniques are applicable. By collapsing the cube in the Z direction, we obtain a reconstructed image of the science object. Than we can treat this image with the ordinary broad band photometry techniques. Furthermore, each slice of the data cube along the spectral direction is a monochromatic image of the object. Thus we can easily extract one or several narrow band images, centred around some specific spectral features. This principle is shown on Figure 2.2, where a colour composite image of the young star cluster in the Large Magellanic Cloud NGC 1850 (top) is dispersed and stored in a schematic data cube (bottom). As an example, three filters have been simulated – the broad bands B (blue) and V (green) and the narrow band $H\alpha$ (red).

For each spatial pixel there is and associated spectrum, which contains kinematical and chemical composition information about the science target. By exploring these spectra, we can reconstruct the velocity profile of the object, as well as its stellar population properties. After comparison with stellar population models we can directly look at the age or metallicity distribution.

2.4 The near-IR sky

2.4.1 Observational techniques in the near-IR

One of the main contributors to the detector counts, counted by an infrared array, when observing an astronomical target in the near-IR, is the very bright night sky, which very often may produce more counts than the scientific target itself. Bellow 2.2 μm the sky emission is dominated by OH emission lines. Red-wards from this wavelength the thermal background from the atmosphere and the telescope dominates.

In order to correct for this contributions, the usual observational technique is to point the telescope consecutively to the target and an empty region on the sky, i.e. to nod the telescope, and afterwards subtract the latter from the former. This is the so called OS technique (O stands for object, S – for sky). In the case of 3D spectroscopy one may also estimate the sky contribution from the science frame itself, if the object does not cover it fully. This might be useful, for example, when a star is observed, a very good AO correction was achieved, and at least half of the spaxels have only sky contribution. In this way one saves the observational time only for the science targets. But in the case of extended objects, such as galaxies or star clusters, it is necessary to observe separately sky frames. Otherwise one risks to remove the signature of the object.

Another imprint on the near-IR science spectra, originating in the Earth's atmosphere, are the telluric absorption lines. These are the most prominent features in the near-IR and are especially deep in the blue end of the K-band. Unfortunately their depth varies with time and they do not scale linearly with the air-mass. Thus we have to observe telluric calibration stars as close as possible in time and space to the science target observation and with the same instrument setup. To ease data reduction it is preferable to observe hot stars, that have early spectral types, and show very weak or no emission or absorption lines. We know that their continuum in the K-band is

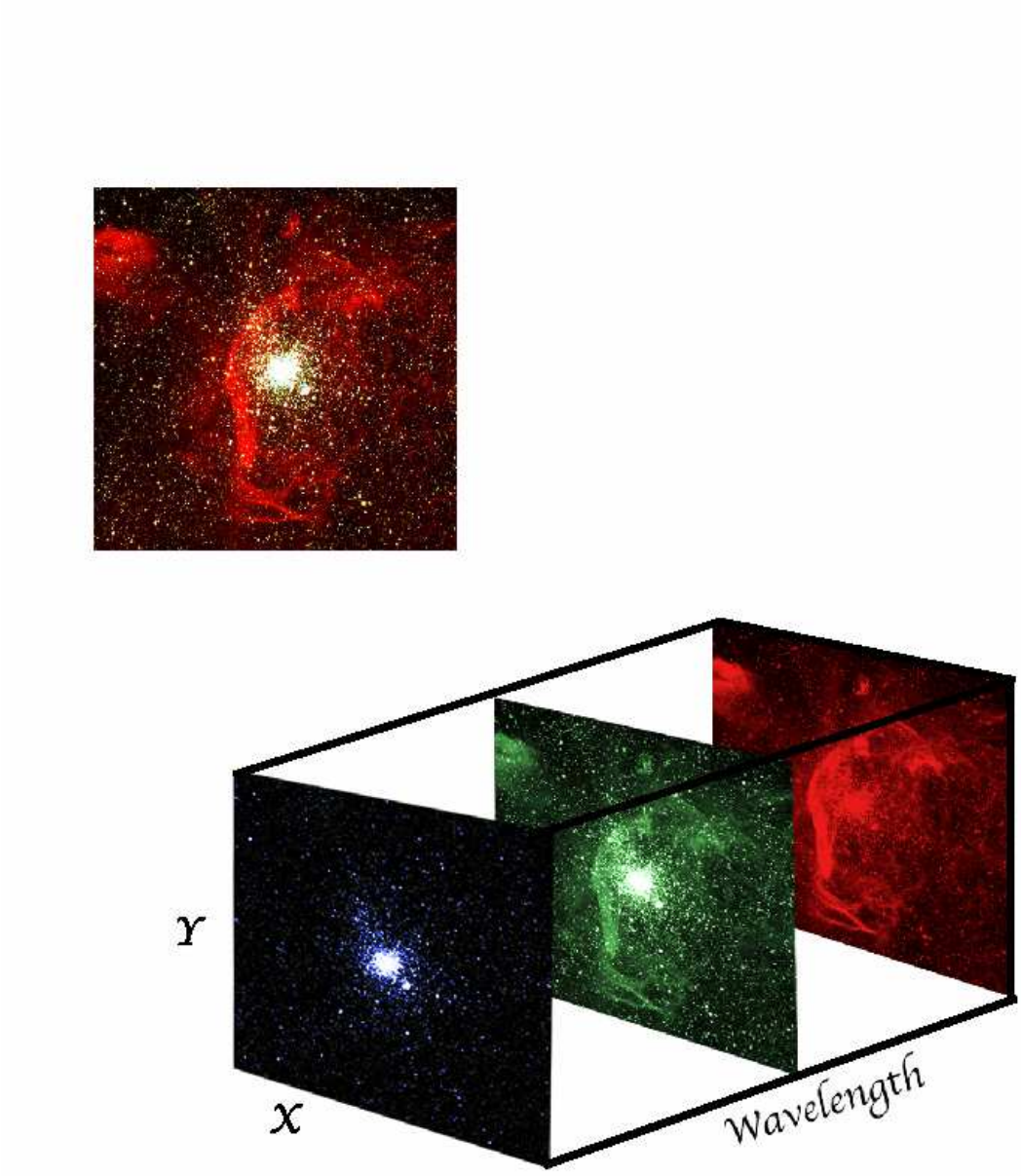

Figure 2.2: Principle of the data cube. The X and Y axis keep the spatial information, while along the Z direction a spectrum for each spaxel is stored. This cartoon shows how NGC 1850 looks in different wavelength planes of the data cube. While the blue band contains light only from the young, hot stars, in the narrow filter $H\alpha$ the glow of the surrounding gas is also visible. (NGC 1850 image credits – ESO.)

well approximated by the Rayleigh-Jeans part of the black body spectrum, associated with their effective temperature. They exhibit only one prominent feature, the hydrogen Bracket γ absorption line at 2.166 μm. The other near-IR bands host some more hydrogen and helium lines. These stellar spectral lines may be a problem if covering spectral features of interests belonging to the science object. Then we have to remove them from the spectrum. After that we also have to remove the telluric star's continuum shape. This is done with the division of the stellar spectrum by scaled black body spectrum, which has the same temperature as the star. In this way one obtains a normalised spectrum, which contains only features, originating in the Earth's atmosphere. The final step is to divide the science spectrum by the telluric spectrum. In this way we also perform a relative flux calibration.

2.4.2 Importance of good sky subtraction and telluric correction

When the goal of the observations is to obtain precise photometry or to measure accurately line strengths (this definition will be given in Chapter 3, for now we will only say that it is similar to equivalent width), it is very important to achieve as good as possible removal of the signature of the night sky. For example if one overestimates the sky background, this will lead to a decrease in the continuum level and to an increase of the line strength of a given absorption feature. Underestimating the sky by only 4 % will lead to a decrease of 1 Å in the line strength for the Na I feature at $\sim 2.2\,\mu$m which has a typical strength of 3 – 5 Å for Fornax cluster galaxies (Silva et al. 2008).

Another source of error is the inaccurate telluric correction. It may introduce new features in the science spectra, and more importantly for features that cover large wavelength span can lead to a change in the continuum shape and again give wrong line strengths.

2.5 The SINFONI data reduction pipeline

To reduce the 3D spectroscopy data for this thesis we used the purpose built data reduction software for SINFONI – the ESO SINFONI pipeline (Modigliani et al. 2007). It comprises 7 major routines, called recipes, which execute the data reduction and 10 additional sub-routines, called utilities, some of which are part of the above recipes, and perform some useful tasks. We will describe only those, which we have used in our data reduction.

2.5.1 Overview of the pipeline tasks

RECIPES

sinfo_rec_detlin

The purpose of this recipe is to estimate when the detector becomes non linear. Input are ~20 flat-field images with increasing intensity. The output is a map of the non

linear bad pixels, which has the tag BP_MAP_NL. These images are part of the SINFONI science calibration plan and are taken once per month.

sinfo_rec_distortion

Input for this recipe are ~70 images of a calibration fiber, while it moves along the y-direction of the image slicer. In this way we compute the optical distortions (DISTORTION) and the distances between the slitlets (SLITLETS_DISTANCE). These calibration frames are acquired also once per month.

sinfo_rec_mdark

3 dark frames are taken daily for each exposure time and with their help the recipe creates a master dark frame (MASTER_DARK) and a bad pixels map (BP_MAP_HP).

sinfo_rec_mflat

The input data set consists of 10 on/off lamp flat fields, taken each day, together with the output from **sinfo_rec_detlin** BP_MAP_NL, the output from **sinfo_rec_mdark** BP_MAP_HP and some other static calibration files. The useful output from this recipe are a master flat field image (MASTER_FLAT_LAMP) and a master bad pixels frame (MASTER_BP_MAP).

sinfo_rec_wavecal

The purpose of this recipe is to create a wavelength map image, where the intensity corresponds to the wavelength. As input we give one on and one off image of the arc lamp in the relevant passband (for the K-band it is a neon lamp), which are taken each day, together with the MASTER_FLAT_LAMP and the MASTER_BP_MAP from the recipe above, the distortions map from the **sinfo_rec_distortion** recipe, and a couple of static calibration files, such as a slitlet position table and a reference arc lines table. The output files, which we use in the next step, contain the wavelength map (WAVE_MAP) and the position of each slitlet on the detector (SLIT_POS).

sinfo_rec_jitter

This recipe executes the full data reduction on the science frames and creates the data cubes. As an input we give our science observations, consisting of a sequence of on-target and sky frames and the relevant calibration files, obtained during the previous steps. These are the master bad pixels and flat field maps, a wavelength map, the table with slitlets positions and distances and the optical distortions table.

This recipe has many parameters, but the most important ones for our work were the parameters responsible for the sky background correction. With their default values the recipe estimates the sky contribution from the science frame itself, by computing the median of each wavelength slice and subtracts it from the spatial plane. In the case of objects, covering a large area of the field-of-view, this may lead to the removal of

the object itself. In order to force the recipe to use the user provided sky frames, one has to switch the parameter `--product-density` to 3, set the `--objnod-aj_method` to 1 and `--objnod-scale_sky` to FALSE.

Then the recipe generates Object-Sky pairs, choosing the closest in time sky frame for each object frame and subtracts the sky from the object. After that it applies the flat field, bad pixels, and distortion corrections. The next step is to reconstruct the object image and write it in a data cube, where the third axis stores the spectrum. Then wavelength calibration is applied to each intermediate data cube and, if chosen, also a supplementary sky residuals cleaning is applied (this procedure is described in Section 2.5.2). The final step is the co-addition of all intermediate data cubes resulting in one averaged data cube. When setting `--product-density` to 3, the output of this recipe contains large number of files – 14 output files for each input object frame, plus the final combined data cube, a reconstructed image of the object, an extracted 1D spectrum, a table with Strehl ratio information, a table with the extracted spectrum and efficiency computations. In this way we can control the data reduction quality for each individual input object frame and exclude some or fine-tune the pipeline parameters for better results.

UTILITIES

The pipeline offers a big variety of utilities, which perform little operations with data cubes, spectra and images. For images these are image arithmetic and reconstruction of an image from the data cube in a selected wavelength range. For data cubes – cube arithmetic, combination of data cubes following user defined mosaic pattern, and additional sky residuals cleaning of the data cubes. For 1D spectra we can divide by a black body spectrum with a given temperature and shift the spectrum by an user defined amount.

The task, which we have used most extensively was the **sinfo_utl_cube2spectrum**, which extracts a 1D spectrum from a data cube. One can choose between a rectangular or a circular aperture, by specifying either the edges of the rectangle, or the centre and radius of the circle. The next choice is about the mathematical operations, performed on the selected spaxels – averaging, computing the median or mean, or just summing up. Setting up minimum and maximum rejection thresholds is also possible.

2.5.2 Cleaning sky line residuals

The usual way of removing the sky emission from the science object frames is by subtracting a sky frame. However, due to instabilities in the instrument (flexures), this simple subtraction may lead to significant line residuals, resembling P-Cygni profiles. The reason for this is that SINFONI is mounted on the Cassegrain focus of VLT and thus moves around together with the telescope. This movement may lead to shifts of up to a substantial fraction of a pixel. To overcome this problem, recent versions of the SINFONI pipeline include an improved sky residuals correction procedure, based on the method described by Davies (2007). It works on already sky subtracted object data cubes and needs a sky data cube (this is one of the intermediate output files from the

sinfo_rec_jitter recipe). Then the routine executes the following steps.

First, it estimates the noise in the object frame and flags the pixels, where the intensity is more than two times the object's noise above the background. Then the sky pixels are identified and selected. With the default value of the parameters this recipe selects at least 80 % of the sky pixels. If the routine does not find enough, it performs a new selection and increases them to the chosen threshold ratio. The next step is to calculate the averaged object and sky spectra. Then the thermal contribution to the sky background is estimated and subtracted from the sky spectrum. This happens after first the sky spectrum is smoothed with the help of a box filter, then Boltzmann function is fitted and finally the fit is subtracted from the sky spectrum.

In order to properly compute the shift between the object and the sky spectrum, the routine chooses the wavelength ranges where the rotational and vibrational transitions of the OH molecule occur. In this way the use of inappropriate spectral lines is avoided. Then the pixel shift between the object and the sky is computed by cross correlation of the two spectra. After that a scaling factor, which has to be applied to remove fully the sky lines, is computed. The final step is to shift and scale the sky data cube with the corresponding amounts and subtract it from the object data cube.

This routine is incorporated in the **sinfo_rec_jitter** recipe, but also exists as a separate utility (**sinfo_utl_skycor**).

Chapter 3

Line strength indices in the near-IR

3.1 Introduction

The question about the formation and evolution of early type galaxies through cosmic time is one of the topics of most heated discussion in contemporary astrophysics. Many theories about galaxy formation and evolution exist. However, their predictions need to be verified by observations. In order to be able to track in detail the star formation and assembly history of galaxies, we would need to observe and derive the properties of the individual stars in a variety of galaxies in different environments. However, with up-to-date telescopes and instrumentation, we are only able to resolve stellar populations within the Local Volume up to 10 Mpc (e.g. Rejkuba et al. 2005; Mouhcine et al. 2007; Harris 2008, for galaxies beyond the Local Group). For the rest of the Universe we have to rely only on studies of the unresolved stellar light.

The method, which provided a big step forward towards our understanding of early type galaxy evolution, was the evolutionary population synthesis. Developed after the 1970's, this approach uses comparisons of theoretical spectral energy distributions (SEDs) of simple stellar populations (SSPs) to the real, observed spectra of stellar clusters and galaxies. The most successful diagnostic tool, that has been developed, was the Lick/IDS system of spectral indices in the optical wavelength range (e.g Faber et al. 1985; Worthey et al. 1994; Trager et al. 1998). It consists of 21 spectral indices originally, covering the strongest features in the optical, and has been extended later. The line strengths in this system are measured like equivalent widths. The definition of each index consists of a central passband on the feature, which is flanked to the blue and to the red by pseudo-continuum passbands. First the average flux in the pseudo-continuum passbands is computed following Equation 3.1

$$F_P = \frac{1}{\lambda_2 - \lambda_1} \int_{\lambda_1}^{\lambda_2} F_\lambda \, d\lambda, \tag{3.1}$$

where λ_1 and λ_2 are the wavelength ranges of each passband. The local continuum is determined after drawing a straight line between the midpoints of the blue and the red continuum levels. The index is then the difference in flux between the passband and this continuum level:

$$EW = \int_{\lambda_1}^{\lambda_2} \left(1 - \frac{F_{I\lambda}}{F_{C\lambda}}\right) d\lambda, \tag{3.2}$$

where $F_{C\lambda}$ is the straight line connecting the blue and red pseudo-continuum levels, $F_{I\lambda}$ is the observed flux per unit wavelength and λ_1 and λ_2 are the limiting wavelengths of the feature passband. Usually indices are expressed as equivalent widths in Ångstroms, but also in magnitudes for indices, measuring the strength of molecular features. Finally, the raw index values are brought to a common system after correcting for the internal velocity dispersion of the astronomical target and the spectral resolution of the spectrograph. The resolution, adopted by the Lick/IDS system, is 8.4 Å ($FWHM$) at 5000 Å. In order to obtain the luminosity weighted age or metallicity of a given galaxy, the values of the indices are compared to the theoretical model predictions. There are indices sensitive to the overall metallicity of the population, like Mg b or various Fe indices, and others, which react stronger to the age, like the hydrogen Balmer lines. This approach has been proved to be effective in braking the so called age-metallicity degeneracy.

3.2 K-band index definitions

3.2.1 Atomic indices

Near-IR arrays have undergone a fast development in the last years and the availability of more and better near-IR spectrographs make the near-IR wavelength range more attractive to the astrophysicist, offering a new window into the exploration of early type galaxy evolution. Single stellar population models in this wavelength range are already available (e.g. Bruzual & Charlot 2003; Maraston 1998, 2005), however a system similar to the Lick indices does not exist yet. Figure 3.1 shows spectra of giant stars of different spectral types in the wavelength region 2.1 – 2.4 μm, taken from the SpeX IRTF Spectral Library (Rayner et al. 2007). The most prominent features are indicated: the hydrogen Brackett γ line, sodium features, iron lines, the calcium triplet, magnesium and some of the CO band-heads. Their central wavelengths are listed in Table 3.1.

Spectral indices are defined in such a way, that they can measure reliably the line strengths of a given spectral feature in a variety of astronomical targets. Different authors have defined and measured line strengths in the near-IR in different ways (e.g. Förster Schreiber 2000; Frogel et al. 2001; Silva et al. 2008; Mármol-Queraltó et al. 2008). Throughout this study we will use the definitions made by Frogel et al. (2001) for the Na I and Ca I features. The index definitions for Fe I A, Fe I B and Mg I are taken from Silva et al. (2008). The wavelength ranges of these near-IR indices are listed in Table 3.2.

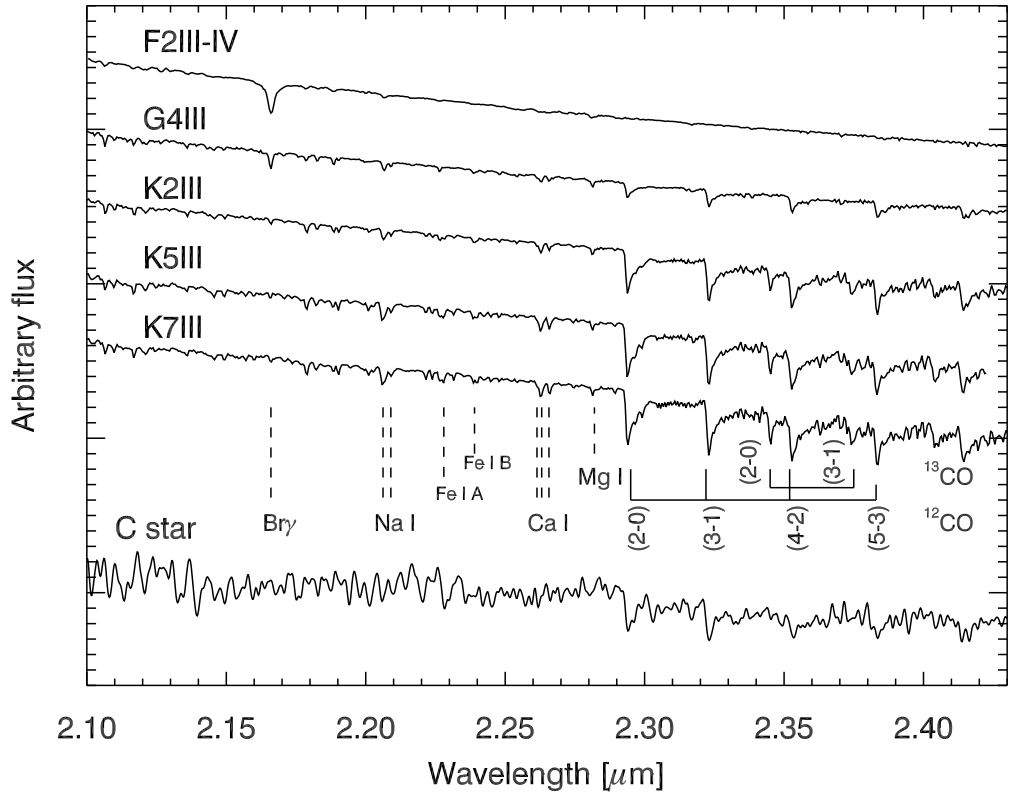

Figure 3.1: Spectra of giant stars from different spectral types, taken from the SpeX IRTF Spectral Library (Rayner et al. 2007). The location of several spectral features is indicated. The spectrum at the bottom of the plot is of a carbon star in the LMC cluster NGC 2162, observed with SINFONI and smoothed to the spectral resolution of the SpeX Library. The increased amount of features, as compared to the other spectra, is not due to low S/N, but these are real absorption lines, due to CH, CN, etc.

Table 3.1: Main spectral features in the *K*-band.

Species	λ (μm)
Br γ	2.1661
Na I	2.2062
Na I	2.2090
Fe I A	2.2263
Fe I B	2.2387
Ca I	2.2614
Ca I	2.2631
Ca I	2.2657
Mg I	2.2814
^{12}CO (2–0)	2.2935
^{12}CO (3–1)	2.3226
^{13}CO (2–0)	2.3448
^{12}CO (4–2)	2.3525
^{13}CO (3–1)	2.3739
^{12}CO (5–3)	2.3829

Table 3.2: Near-IR atomic index definitions.

Index	Blue continuum	Central bandpass	Red continuum	Source
Na I	2.1910 – 2.1966	2.2040 – 2.2107	2.2125 – 2.2170	Frogel et al. (2001)
Ca I	2.2450 – 2.2560	2.2577 – 2.2692	2.2700 – 2.2720	Frogel et al. (2001)
Fe I A	2.2133 – 2.2176	2.2250 – 2.2299	2.2437 – 2.2497	Silva et al. (2008)
Fe I B	2.2133 – 2.2176	2.2368 – 2.2414	2.2437 – 2.2497	Silva et al. (2008)
Mg I	2.2700 – 2.2720	2.2795 – 2.2845	2.2850 – 2.2874	Silva et al. (2008)

Note: Wavelengths are listed in μm.

3.2.2 The ^{12}CO (2–0) molecular index

The index, which measures the strength of the ^{12}CO (2–0) band-head, which we use in our analysis of stellar populations in early type galaxies, has a slightly different definition, as compared to atomic indices. Figure 3.1 shows the unusual and asymmetric shape of this very broad feature. For this reason Frogel et al. (2001) defined four pseudo-continuum bands on the blue side of the central passband. The local continuum level is determined in a similar way, as in the Lick system, but instead of using two pseudo-continuum passbands, here we use four and the pseudo-continuum on the red side is an extrapolation from the blue side. The wavelength intervals of this index definition are listed in Table 3.3.

Recently, Mármol-Queraltó et al. (2008) published a study of the sensitivity of different index definitions for this feature to various sources of errors, i.e. wrong continuum shape or large velocity dispersions. They define a new index, called a generic discontinuity, and show that, compared to previous definitions it is less sensitive to large velocity dispersions of the astronomical target or the spectral resolution of the instrument, recession velocity errors, and incorrect continuum shape, caused by e.g. imperfect telluric correction. The Frogel ^{12}CO (2–0) index is prone to be affected by all of the above sources of errors, due to its very broad wavelength coverage (Silva et al. 2008). Thus we have to be very careful in the error analysis. For this reason Mármol-Queraltó et al. (2008) have chosen a narrower feature passband, which blue end is shifted blue-wards in comparison with the definition of Frogel et al. (2001), to minimise the effects of incorrect de-redshifting (see Figure 3.3, bottom plot). They consider two pseudo-continuum passbands again on the blue side of the feature passband. The passband limits of the index defined by Mármol-Queraltó et al. (2008) are also given in Table 3.3.

3.3 Index measurement procedure

The principle of computing the value of a near-IR index is the same as in the optical Lick system. Figure 3.2 shows as an example the Ca I index. The central passband, marked with vertical solid lines, is surrounded by a blue and a red pseudo-continuum passband (the vertical dashed lines). The average fluxes in the two pseudo-continuum bands are computed following Equation 3.1 and are marked on the figure with a blue and a red cross, respectively. The local continuum level is defined by drawing a straight line between the centres of the pseudo-continuum bands at the levels of the average fluxes. Then Equation 3.2 is applied to get the index value. Before measuring the index the spectra were brought to zero rest-frame velocity. During the index measurement procedure we have corrected the indices for the line of sight velocity distribution (LOSVD) and the spectral resolution of the instruments. These steps will be discussed in more details in Section 3.4.

The ^{12}CO (2–0) index, defined by Frogel et al. (2001), is measured in a similar way. Figure 3.3, top plot, shows the extent of the pseudo-continuum passbands with differ-

Table 3.3: Different index definitions for ^{12}CO (2–0).

Index name	Continuum bands	Feature bandpass	Source
^{12}CO (2–0)	2.2300 – 2.2370	2.2910 – 2.3020	Frogel et al. (2001)
	2.2420 – 2.2580		
	2.2680 – 2.2790		
	2.2840 – 2.2910		
D_{CO}	2.2460 – 2.2550	2.2880 – 2.3010	Mármol-Queraltó et al. (2008)
	2.2710 – 2.2770		

Note: Wavelengths are given in μm.

ent line styles. The portion of the spectrum, which is in between the wavelength ranges of the feature bandpass, is shown with a red colour. The average fluxes in the pseudo-continuum passbands, computed with the help of Equation 3.1, are shown with blue crosses. Then the continuum level is determined as the line, which intersects the four points, and is extrapolated to reach the feature passband. The raw ^{12}CO (2–0) index value is obtained as for the other indices and needs velocity dispersion correction as well.

The generic discontinuity, that Mármol-Queraltó et al. (2008) define, measures the ratio between the average fluxes in the continuum and the absorption bands, using the following formula:

$$D_{CO} \equiv \frac{\frac{\sum_{i=1}^{n_c} \int_{\lambda_{c,i_1}}^{\lambda_{c,i_2}} F_{c,i}(\lambda)\, d\lambda}{\sum_{i=1}^{n_c} \lambda_{c,i_2} - \lambda_{c,i_1}}}{\frac{\sum_{i=1}^{n_a} \int_{\lambda_{a,i_1}}^{\lambda_{a,i_2}} F_{a,i}(\lambda)\, d\lambda}{\sum_{i=1}^{n_a} \lambda_{a,i_2} - \lambda_{a,i_1}}}, \tag{3.3}$$

where D_{CO} is the generic discontinuity, $F_{a,i}(\lambda)$ are the fluxes in the n_a absorption bands (in their case $n_a = 1$) and $F_{c,i}(\lambda)$ are the fluxes in the n_c continuum bands (in their case $n_c = 2$). λ_{x,i_1} and λ_{x,i_2} are the lower and upper limits of the i^{th} passband, where x stands for a or c. The locations of the different wavelength ranges for ^{12}CO (2–0) index definitions are shown on Figure 3.3.

We measure index errors based on error spectra with the help of Monte Carlo simulations, where we take into account recession velocity errors, velocity dispersion errors and photon noise.

3.4 Index calibration to a common system

The observed spectrum of a stellar population is the convolution of the integrated spectrum of all the stars in the population by their LOSVD and the instrumental broadening. These effects broaden the spectral feature of interest and in general reduce the observed line strength compared to the intrinsic value. In order to compare our observations with other studies, often obtained with different instruments, and eventually

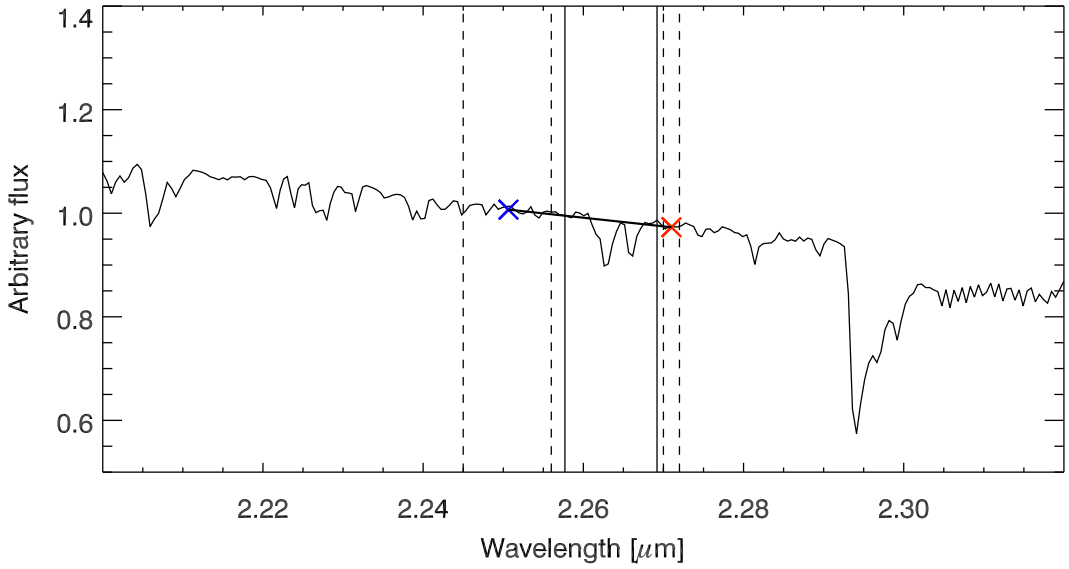

Figure 3.2: Outline of the index measurement procedure. The spectrum of a K7III star is shown, together with the wavelength ranges of the Ca I index. The vertical solid lines mark the extent of the central passband. The vertical dashed lines show the blue and red pseudo-continuum passbands. During the measurement procedure the level of the flux in the blue and red passbands is determined, marked here with blue and red crosses, respectively, and a straight line between these two values is drawn to define the local continuum level.

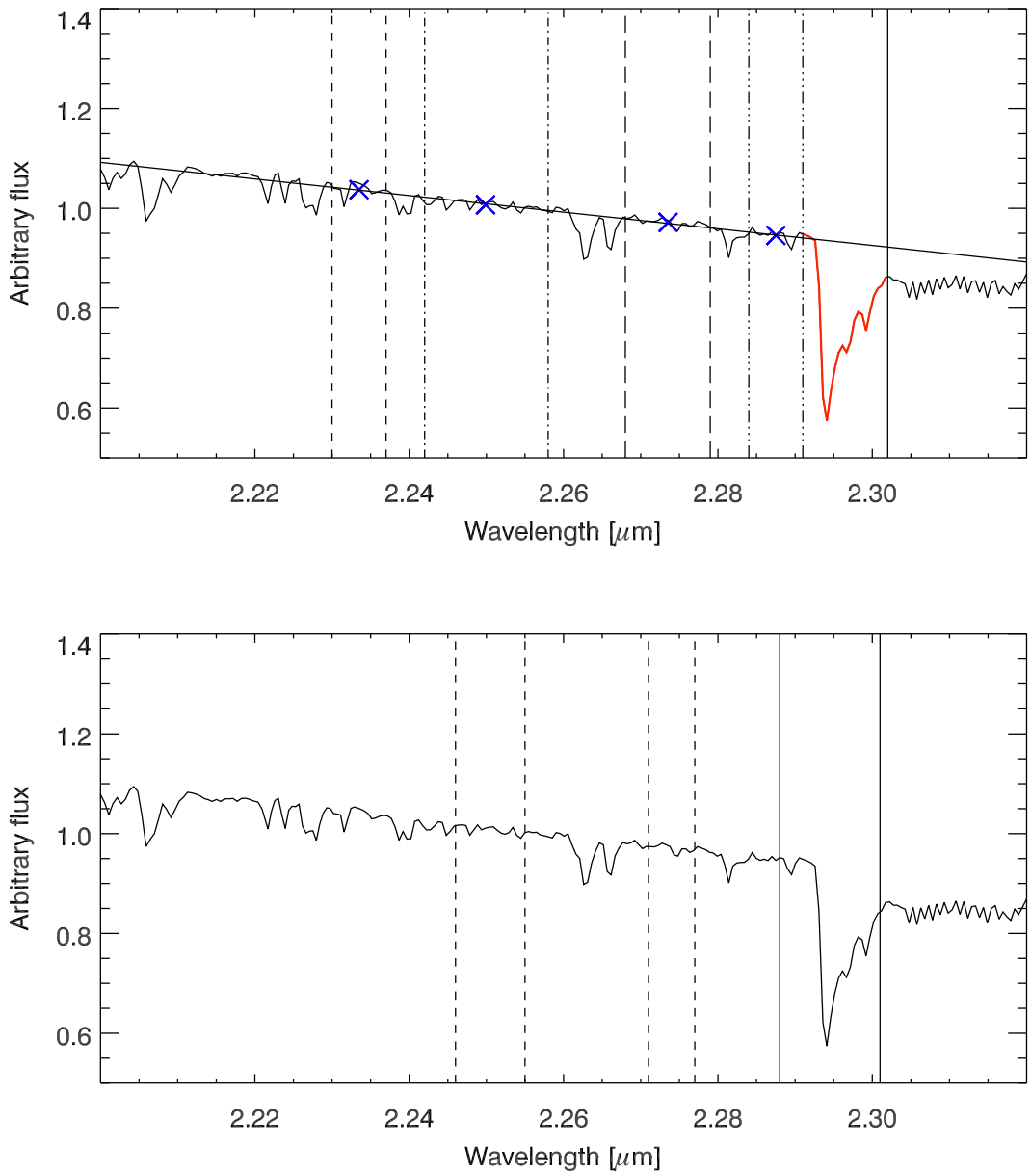

Figure 3.3: Different index definitions for the ^{12}CO (2–0) feature. *Top panel*: Index definition by Frogel et al. (2001). The extents of the four pseudo-continuum passbands are shown with different line styles. The average flux level in each one of them is marked with a blue cross. The extrapolated continuum is shown with a solid line. The blue edge of the ^{12}CO (2–0) feature passband overlaps with the red edge of the neighbouring continuum passband, thus it is not overplotted. For guidance the portion of the spectrum, which falls between the ranges of the feature passband is shown with a red colour. The wavelength, which delimits the passband on the red side is shown with a solid vertical line. *Bottom panel*: Wavelength ranges of the generic discontinuity D_{CO}, defined by Mármol-Queraltó et al. (2008). The pseudo-continuum passbands are marked with dashed lines, while the feature passband is surrounded by solid lines.

with population synthesis models, one needs to calibrate the data to a common system. Here we list the most important steps towards index calibration.

3.4.1 Spectral resolution

In the literature there is a lack of a large data set of near-IR spectra and index values of stars and galaxies, which would set the standards. The recently published study of Mármol-Queraltó et al. (2008) is currently the largest spectral library with 220 stars, covering a range in effective temperatures and metallicities. They have observed the majority of the stars with the 3.5 m telescope at Calar Alto Observatory with Ω-CASS. The spectral resolution of this instrument is 6.8 Å in the *K*-band. The earliest attempts for a systematical study of the near-IR spectral properties of early-type galaxies date back in the end of 1990's (Mobasher & James 1996, 2000; James & Mobasher 1999, 2000). However, a progress has been made only recently using more advanced near-IR instruments (e.g. Silva et al. 2008). These authors have observed and measured the line strengths of 11 early type galaxies in the Fornax cluster. This study was made using VLT/ISAAC, which offers a spectral resolution of 6.9 Å ($FWHM$) at 2.2 μm. In order to be consistent with the above studies, we have chosen to broaden our observations, where needed, to 6.9 Å ($FWHM$).

3.4.2 Rest frame velocity

Before measuring any spectral index, we have to determine the radial velocity of the spectrum and correct for it, since the wavelength ranges for each index are given with respect to zero radial velocity. We have used two methods to derive the observed radial velocities for the objects, studied in this work. For the Fornax cluster galaxy NGC 1399 we have used the Penalised Pixel-Fitting method (pPXF) developed by Cappellari & Emsellem (2004). The success of this method relies on the provision of a good set of template spectra, which match the galaxy spectra as well as possible. Then the code computes and fits an optimal velocity template spectrum, from which it measures the radial velocity, as well as higher moment of the LOSVD. More details about this procedure, the wavelength regions of the fits and selection of velocity template stars will be given in Section 6.3.1, where we describe the data.

For the globular clusters and stars in the Large Magellanic Cloud, as well as for the sample of field ellipticals, discussed in Chapter 5, we have used a different method, due to the lower quality of the spectra. In principle we were able to extract a reliable kinematical information from part of these observations with pPFX, but for the sake of uniformity we decided to use the Fourier cross correlation technique for the whole data set. Using the task `fxcor`, which is part of the IRAF environment, we have determined the radial velocity of each object in the LMC observational sample. This task performs a Fourier cross correlation on the input object spectrum and a template star in the region 2.2 – 2.4 μm, where the most prominent features in the *K*-band reside and allow for good cross-correlation. The results from the two techniques, `fxcor` and pPFX, were very similar for the spectra, on which we used both.

3.4.3 Velocity dispersion measurements and corrections

In order to compare index measurements between different objects we have to calibrate them to zero velocity dispersion. For this purpose we need to know first, the observed properties of the LOSVD and second, the correction factor to be applied. Then the corrected index is:

$$I_{corrected} = I_{observed} \times C, \tag{3.4}$$

where C is the correction factor.

We measured the velocity dispersions for the objects together with the radial velocities measurements. This was done using pPXF and only in the case of the elliptical galaxy NGC 1399. The velocity dispersions of LMC globular clusters, the largest of which is 8.1 km s^{-1} in NGC 2005 (Dubath et al. 1997), imply negligible correction factors, as shown in Figure 3.4. But some of the elliptical galaxies in our sample have central velocity dispersions reaching $\sim$400 km s^{-1}, like NGC 1399 (Kuntschner 2000), which implies the need of significant corrections. Kuntschner (2004) show that significant non-Gaussian terms of the LOSVD can have significant influence on the line strengths as well. This means that not only the first two moments of the LOSVD, namely velocity and σ, are important for the proper correction of line strengths, but also the higher order Gauss-Hermit terms. However, reliable estimates of h_3 and h_4 are possible only for relatively high S/N data (see discussion in Sections 6.2.4 and 6.3.1). We have measured the full set of the first four moments of the LOSVD, v, σ, h_3 and h_4, in all of the two-dimensional spectra of NGC 1399, since in this case we are interested in their spatial changes. Early-type galaxies exhibit structures in their LOSVD moments maps (Emsellem et al. 2004). For the rest or our sample we measured simply v and σ. We ignored the higher order moments because in the central spectra of early-type galaxies the asymmetries in the shapes of the LOSVD cancel and we can assume $h_3 = 0$ and $h_4 \sim 0$ for our purposes.

To determine the correction factor from Equation 3.4 we have used the method developed by Kuntschner (2004). Following this method, we have taken a sample of velocity template stars, assuming that their LOSVDs are $\sigma = 0$, $h_3 = 0$ and $h_4 = 0$ and then broadened them to velocity dispersions ranging up to 440 km s^{-1} in steps of 20 km s^{-1}, and h_3 and h_4 values between -0.20 and +0.20. Then from each resulting spectrum we derive a correction factor for each index such that

$$C_{j,k}(\sigma, h_3, h_4) = \frac{I_{j,k}(\sigma = 0, h_3 = 0, h_4 = 0)}{I_{j,k}(\sigma, h_3, h_4)}, \tag{3.5}$$

where $I_{j,k}$ is the index measured for the star k and index j. A third order polynomial fit to all the values of C_j seems to be a good description of the data:

$$C_{j,k}(\sigma, h_3, h_4) = 1.0 + \sum_{i=1}^{3} a_{i,j}\sigma^i + \sum_{i=1}^{2} b_{i,j}\sigma^i h_3 + \sum_{i=1}^{2} c_{i,j}\sigma^i h_4, \tag{3.6}$$

where $a_{i,j}$,$b_{i,j}$ and $c_{i,j}$ are the correction coefficients for the index j. They are listed in Table 3.4. Thus the final corrected indices are computed following:

$$I_{j,corr} = I_{j,obs} \times C_j(\sigma, h_3, h_4) \tag{3.7}$$

We have derived correction coefficients for five of the near-IR indices, defined in Section 3.2 – Na I, Ca I, Fe I A, Fe I B and ^{12}CO (2–0). The Mg I index is too weak and reliable measurements and corrections are not possible, thus we have excluded it from the analysis. For the object spectra where we do not measure h_3 and h_4 we have used only the first three coefficients from Table 3.4 (i.e. $h_3 = 0$ and $h_4 = 0$). Figure 3.4 gives an overview of the correction factors for the five indices as a function of the velocity dispersion (figure taken from Silva et al. (2008)).

Table 3.4: LOSVD corrections coefficients for near-IR indices

j	Name	a_1	a_2	a_3	b_1	b_2	c_1	c_2
1	Na I	-1.2877E-04	2.7216E-06	2.3059E-09	-1.4584E-03	3.2313e-06	6.6710E-04	1.0431E-05
2	Ca I	-1.4209E-03	1.9185E-06	4.1321E-09	1.1321E-03	2.6828e-06	-1.2206E-03	1.3120E-05
3	Fe I A	-8.7484E-04	4.4710E-06	2.7938E-09	-2.3459E-03	8.7774e-06	8.0801E-04	1.1374E-05
4	Fe I B	-2.6148E-03	1.2048E-05	-5.1560E-09	2.2815E-03	1.4769e-06	4.1776E-03	-4.9050E-07
5	^{12}CO (2–0)	-6.5607E-05	9.9898E-07	3.6315E-10	1.7987E-04	-2.1733E-07	8.6552E-04	2.1408E-06

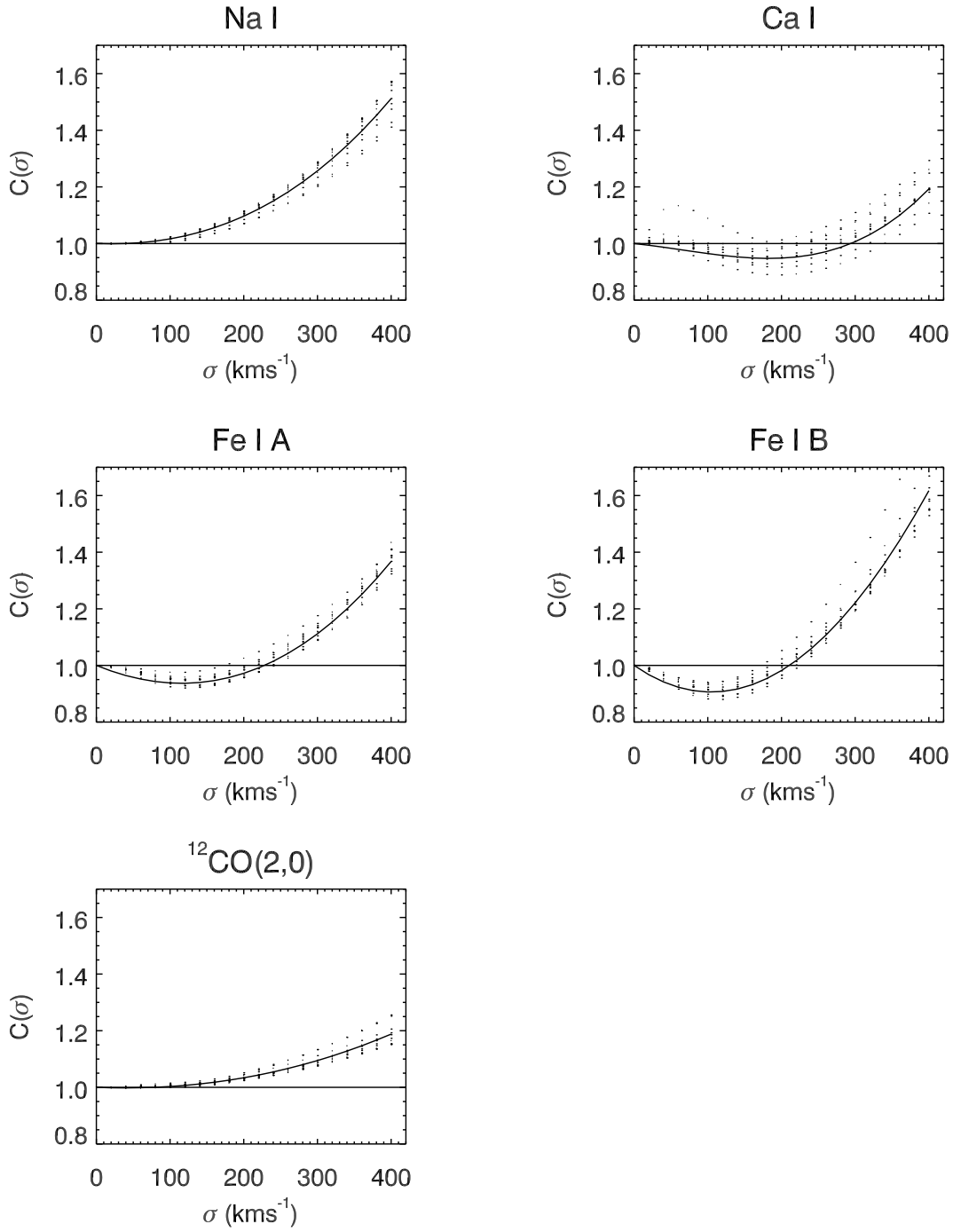

Figure 3.4: Velocity dispersion corrections for near-IR indices from Silva et al. (2008). The dots represent individual stars, broadened to different σ. Here the higher order moment h_3 and h_4 are neglected. The solid line is a third order polynomial fit to the data and is used to apply the LOSVD corrections.

Chapter 4

Integrated near-IR spectra of six globular clusters in the LMC

4.1 Motivation of the project

Since the 90's, the interpretation of the integrated light of galaxies (in the nearby universe or at high redshift) heavily relies on evolutionary population synthesis (EPS) models. Such models were pioneered by Tinsley (1980) and the method has been heavily extended since then (e.g. Bruzual & Charlot 1993; Worthey 1994; Vazdekis et al. 1996; Maraston 2005; Schiavon 2007). They are used to determine ages, element abundances, stellar masses, stellar mass functions, etc., of those stellar populations that are not resolvable into single stars with today's instrumentation, i.e. most of the universe outside the Local Group. To build such EPS models we use simple stellar populations (SSP). There are two essential advantages of focusing on SSPs. First, SSPs can be reliably calibrated. They can be compared directly with nearby globular cluster (GC) data for which accurate ages and element abundances are independently known from studies of the resolved stars. This step is crucial to fix the stellar population model parameters that are used to describe model input physics and which cannot be derived from first principles (e.g., convection, mass loss and mixing). Second, SSPs can be used to build more complex stellar systems. Systems made up by various stellar generations can be modelled by convolving SSPs with the adopted star formation history (e.g. Kodama & Arimoto 1997; Bruzual & Charlot 2003). Models describing accurately the integrated light properties, including medium to high resolution spectra and/or line-strength indices, are and will be our only tool to investigate and analyse the star-formation history over cosmological time-scales.

This approach has worked well in the optical regime of spectroscopy and has led to well calibrated models (see e.g. Puzia et al. 2002; Thomas et al. 2003; Maraston 2005). With the application of such models to observed spectra we derive reasonable estimates of the main stellar population parameters (age, chemical composition and M/L ratio) in the nearby universe (e.g., Kuntschner 2000; Thomas et al. 2005; Cappellari et al. 2006) as well as at higher redshifts (e.g., Maraston 2005). Of course, uncertainties remain due to the degeneracy of age and metallicity effects in the optical wavelength range (e.g., Worthey 1994). The integrated near-IR light in stellar populations with ages

≥ 1 Gyr is dominated by one stellar component, cool giant stars, whose colour and line indices are mainly driven by one parameter: metallicity (Frogel et al. 1978). Near-IR colours and indices also have the advantage of being more nearly mass-weighted, i.e., the near-IR mass-to-light ratio is closer to one (see e.g., Worthey 1994). So, by combining the optical as well as near-IR information one can resolve the currently remaining degeneracies and hope to gain a better understanding of star-formation histories. However, currently available stellar population models have arguably the largest uncertainties in the near-IR (exact treatment of RGB and AGB populations) and thus it is of paramount importance to provide high-quality observational data to validate and improve the state-of-the-art models.

Our goal is to provide an empirical near-IR spectral library for integrated stellar populations with ages ≥ 1 Gyr to serve as benchmark for stellar population models. Globular clusters in the Local Group are an ideal laboratory for this project since ample information from studies of the resolved stars is available. Yet, integrated spectroscopic observations of the Galactic GCs in the near-IR are very challenging due to their large apparent sizes on the sky.

The Large Magellanic Cloud (LMC), located at about 50 kpc away from the Milky Way, is a much better observational choice. It is often classified as an irregular galaxy, due to its messy structure. It also exhibits a prominent bar in the centre, suggesting that earlier it might have actually been a barred spiral galaxy, disrupted by the tidal field of the Milky Way (Bekki & Chiba 2005). It shows evidences for a very complex and still ongoing star formation activity. The LMC GCs have an advantage (for the scope of this project) with respect to Galactic GCs - they span a larger range in ages. Studies of the globular clusters system show one old component with age > 10 Gyr. After this time there was a "dark age" with just one cluster formed before a new burst of cluster formation that has started around 3 – 4 Gyr ago (Da Costa 1991).

Our project aims at empirically constraining the spectrophotometric properties of the LMC globular clusters in the near-IR as a function of age and metallicity. The results, presented in this thesis, are part of a pilot study, whose goal is to validate the observational and analysis strategy.

4.2 Sample selection

Since we are mainly interested in the application of SSP models to the integrated light of early-type galaxies, we will restrict our sample in this pilot study to intermediate age and older clusters. The sample has been selected from the Bica et al. (1996, 1999) catalogues by choosing the SWB class (Searle et al. 1980) to be V, VI or VII. In this way we ensure that the target systems will have ages ≥ 1 Gyr. We further required the clusters to be bright ($M_V < -5.8$) and reasonably concentrated (effective radius ≤ 35″). Where no literature data were available, the concentration was checked by eye on DSS images. Another selection criterion was the availability of auxiliary data, because we need detailed information on age and chemical composition. Such is available

Table 4.1: LMC GCs observing log.

Name	UT date	V	$(B-V)$	SWB	Age	[Z/H]
(1)	(2)	(3)	(4)	(5)	(6)	(7)
NGC 1754	2006 Nov 18	11.57	0.75	VII	10	-1.42[a], -1.54[b]
NGC 2005	2006 Nov 29	11.57	0.73	VII	10	-1.35[a], -1.92[b], -1.80[c], -1.33[d]
NGC 2019	2006 Dec 10	10.86	0.76	VII	10	-1.23[a], -1.18[b], -1.37[c], -1.10[d]
NGC 1806	2006 Dec 06	11.10	0.73	V	1.1	-0.23[b], -0.71[e]
NGC 2162	2006 Dec 05	12.70	0.68	V.V	2	-0.23[b], -0.46[f]
NGC 2173	2006 Dec 06	11.88	0.82	VI	1.1	-0.24[b], -0.42[f], -0.51[g]

Notes: (1) Cluster name, (2) date of observation, (3) integrated V-band magnitude, (4) $(B-V)$ colour and (5) SWB type taken from (Bica et al. 1996, 1999), (6) Age of the cluster in Gyr, based on the SWB type (Frogel et al. 1990), (7) [Z/H] derived using different methods: [a] Olsen et al. (1998) – slope of the RGB; [b] Olszewski et al. (1991) – low-resolution Ca II triplet; [c] Johnson et al. (2006) – high-resolution Fe I; [d] Johnson et al. (2006) – high-resolution Fe II; [e] Dirsch et al. (2000) – Strömgren photometry; [f] Grocholski et al. (2006) – low-resolution Ca II triplet; [g] Mucciarelli et al. (2008) – high-resolution spectroscopy.

from e.g. Grocholski et al. (2006); Johnson et al. (2006); Mucciarelli et al. (2006, 2008); Mackey et al. (2008). All of the selected clusters have HST/WFPC2 and/or ACS imaging (e.g. Olsen et al. 1998; Mackey & Gilmore 2003), integrated optical spectroscopy, and spectra of the individual giant stars (e.g. Olszewski et al. 1991; Beasley et al. 2002; Johnson et al. 2006; Mucciarelli et al. 2008). We can also benefit from near-IR studies, both imaging and spectroscopy, of the giant stars in these clusters (e.g. Frogel et al. 1990; Mucciarelli et al. 2006), as well as of their integrated light (Persson et al. 1983; Mucciarelli et al. 2006; Pessev et al. 2006). Taking into account the above criteria we have selected six clusters as targets for this pilot project, aiming at validating the strategy for observations and analysis. Three of the clusters are metal poor ([Z/H] ~ -1.4) and have ages of more than 10 Gyr. The other three are more metal rich ([Z/H] ~ -0.4) and younger, with ages up to 2 Gyr. There are different age and metallicity estimates for the clusters in our sample in the literature, depending of the methods used. Here we will list the ages based on SWB types, given in Frogel et al. (1990) and a compilation of metallicities, obtained from the literature. A summary of the clusters' properties is given in Table 4.1 together with the date of our observations with SINFONI 3D spectrograph on ESO VLT Yepun (UT4) telescope.

One of the main challenges of this project is the sparse sampling of bright AGB and RGB stars, due to the limited field-of-view (FoV) of our observational setup and the stochastic effects. Integrated spectra of clusters with less than $10^4\,L_\odot$ are likely to be dominated by statistical fluctuations in the number of bright stars (Renzini 1998; Puzia et al. 2002). These particular phases of the stellar evolution are one of the main contributors to the integrated light of an intermediate age stellar population in the near-IR (e.g. Maraston 2005). To sample as much of the cluster light in a reasonable observing time, we made a mosaic of 3×3 VLT/SINFONI pointings centred on each

cluster. We estimated the light, sampled by this central mosaic (24'' × 24'') for all of the clusters with the help of Equation 4.1, taken from Puzia et al. (2002, their equation 3) and using 20'' radius aperture K-band photometry of Pessev et al. (2006).

$$L_T = BC_K \cdot 10^{-0.4\cdot(m_K-(m-M)-M_{K,\odot}-A_K)} \tag{4.1}$$

m_K is the observed K-band integrated magnitude of the cluster, $(m - M) = 18.5$ is the adopted distance modulus to the LMC (van den Bergh 1998; Alves 2004), A_K is the extinction for each cluster, $M_{K,\odot} = 3.41^m$ is the K-band absolute magnitude of the Sun (value taken from Maraston 1998). The bolometric correction BC_K is applied in order to obtain the total bolometric luminosity L_T of the cluster. It depends on the adopted age and metallicity of the stellar populations. In our case it is 0.6 for the group of the old and metal poor clusters (NGC 1754, NGC 2005 and NGC 2019) and 0.3 for the more metal rich and intermediate age clusters NGC 1806, NGC 2062 and NGC 2173 (Maraston 1998, 2005).

For all but two clusters we find that the sampled luminosity is $> 10^4\, L_\odot$ (see Table 4.2). Only the young clusters NGC 2162 and NGC 2173 are at the limit or bellow this value. In order to improve the statistical probability of getting the majority of the RGB and AGB stars, we observed, in addition to the central mosaics, up to 8 of the brightest stars surrounding each cluster and outside of the central mosaic. Their selection was based on $K - (J - K)$ colour-magnitude diagrams from the 2MASS Point Source Catalogue (Skrutskie et al. 2006) of all the stars with reliable photometry and located inside the tidal radius of each cluster (r_t taken form McLaughlin & van der Marel 2005, see Table 4.2). We selected the stars with $(J - K) > 0.9$ and $K > 12.5^m$ as an initial separation criterion from the LMC field population (See Figure 4.1 and 4.2).

The inclusion of these additional bright stars in our sample has a twofold purpose. The original idea, as described above, is to provide a better sampling of the integrated cluster light by in- or excluding these bright stars (after a careful decision process, based on kinematical and chemical composition assumptions). Second, the stars, which turn out not to be members of any cluster, are representative for the LMC field population in the vicinity of our GCs. Thus we obtain an independent field AGB stars sample for comparison with the globular clusters. The main properties of these additional stars are listed in Table 4.3.

Figures 4.1 and 4.2 show that the stars from the SINFONI central mosaic observations (red dots) do not always fall on the red giant branch of the colour-magnitude diagrams of the clusters and are shifted to bluer colours, resembling the LMC field population. We consider this is due to the imperfect 2MASS photometry, caused by crowding effects within the dense cluster regions.

A colour-magnitude diagram for all of the objects in our sample, stars and central mosaics, is shown in Figure 4.5. For the J and K-band magnitude of the central mosaics we have adopted the 20'' radius aperture photometry of Pessev et al. (2006), which, as shown on Figure 4.4, matches reasonably well our central mosaics. The bright stars are denoted with diamond symbols (the colour coding shows next to which cluster a

Table 4.2: LMC GCs structural and photometric properties.

Name	r_h	r_t	K_{r_t}	K_{20}	L_{mosaic}	R_{int}	K_{M06}	$(J-K)$	$(H-K)$
(1)	(2)	(3)	(4)	(5)	(6)	(7)	(8)	(9)	(10)
NGC 1754	11.″2	142.″9	9.01	10.21	2.9×10^4	20″	–	–	–
NGC 2005	8.″65	98.″8	8.92	9.80	4.2×10^4	20″	–	–	–
NGC 2019	9.″72	121.″6	8.31	9.21	7.2×10^4	20″	–	–	–
NGC 1806	–	–	7.57	9.19	3.7×10^4	100″	7.076	1.055	0.271
NGC 2162	21.″37	197.″2	9.65	11.18	0.6×10^4	120″	9.071	1.253	0.372
NGC 2173	34.″35	393.″5	8.86	10.69	0.9×10^4	60″	9.050	1.033	0.297

Notes: (1) Cluster name, (2) half-light radius and (3) tidal radius of the King-model cluster fit from the catalogue of McLaughlin & van der Marel (2005), (4) *K*-band integrated magnitude within the tidal radius from Pessev et al. (2006). For NGC 1806, where r_t is unknown, we list the magnitude within 200″ radius. The same applies for NGC 2173, because aperture equal to the tidal radius does not exist, (5) *K*-band magnitude from Pessev et al. (2006) with aperture radius 20″, which matches reasonably well our central SINFONI mosaics, (6) sampled bolometric luminosity within the clusters central mosaics in $L_\odot$, computed following Equation (4.1), (7) integration radius, up to which we have added stars from the additional bright AGB stars sample, (8), (9) and (10) photometry with fixed aperture radius of 90″ of Mucciarelli et al. (2006).

given star was observed). Their photometry comes from the 2MASS Point Source Catalogue and magnitudes are dereddened following the same method as Pessev et al. (2006) – extinction values were obtained from the Magellanic Clouds Photometric Survey (Zaritsky et al. 1997) and adopting the extinction law of Bessell & Brett (1988). The slanted line in this figure represents the separation between oxygen- and carbon-rich stars of Cioni et al. (2006). According to this criterion we have five carbon rich stars in our sample.

Figure 4.3 shows optical DSS *R*-band images of our cluster sample. The black cross and box on each cluster image match the centre and the extent of the SINFONI mosaic coverage, respectively. The red squares mark some of the additional bright stars, observed around the clusters. For the sake of clarity on this figure we show only the closest ones. The green circle and cross show the centring and 20″ radius aperture, which Pessev et al. (2006) used to obtain integrated magnitudes of each cluster. The cyan circles show the 90″ radius aperture used by Mucciarelli et al. (2006). We use these photometric studies to compare our spectroscopy with integrated colours and magnitudes. The largest offset between our centring and the ones listed by the other authors is in the case of the poorly populated cluster NGC 2173, where the offset is 17″ (in all other cases this offset is smaller than 5″). In Figure 4.4 we show the 2MASS *K*-band images, obtained from the 2MASS Extended Source Catalogue. All symbols and colours are the same as on Figure 4.3. It is interesting to note the obvious differences between the optical and the near-IR light of these clusters. At optical wavelengths the clusters look much larger and brighter, while in near-IR they are much more concen-

trated and, in the case of the intermediate age clusters, dominated by just a few very bright stars.

4.3 Observations and data reduction

4.3.1 Observations

The observations of the selected globular clusters and stars were obtained in service mode in the period October 2006 – January 2007 with SINFONI in three near-IR bands – *J*, *H*, and *K*. As a starting point we decided to analyse the data in the *K*-band and from here on we will discuss only this sub-set. The results from the other two filters will be presented in a following study.

The SINFONI *K*-band grating covers the wavelength range from 1.95 to 2.45 μm at a dispersion of 2.45 Å/pix. The spectral resolution around the centre of the filter is R$\simeq$ 3500, as measured from arc lamp frames. Due to the relatively large apparent sizes of LMC GCs on the sky, they could not be observed within one single SINFONI FoV, even the largest one available, covering 8″ × 8″. In order to be able to sample at least one effective radius for the majority of the clusters we decided to use a 3 × 3 mosaic of the largest FoV of SINFONI, thus covering the central 24″ × 24″ for each cluster. Given the goal to sample the total light, and not to get the best possible spatial resolution, all the observations were performed in natural seeing mode, i.e. with no AO correction. The integration time was chosen based on the requirement to achieve a signal-to-noise ratio of at least 50 in the final integrated spectra. The optimal exposure time for one pointing of the mosaic was 150 s, divided into three integrations of 50 s, dithered by 0.″25 to reject bad pixels. With the short integration time we assure less sensitivity to the very bright and variable near-IR night sky.

As described in Section 2.4, in order to correct for the effects of the night sky, we have to observe empty sky regions very close in time and space to our scientific observations. Fig 4.6 gives an overview of the pattern, which we have used to design one observation block (OB). First we start with 50 s integration on a "sky" region, then the telescope moves to the centre of the cluster and executes three 50 s integrations, dithered by 1 spatial pixel (0.″25) in each direction. Then it goes back to the sky field and does not observe the same point, as the previous "sky", but a different point, shifted by 8″, and goes again to the cluster, where it makes the next three integrations on the next mosaic pointing (also shifted by 8″ with respect to the centre of the cluster). This pattern is repeated nine times in total, with the only difference being the changing direction of the 8″ shift. At the end we observed one more, "closing" sky frame. After that the OB continues with the bright stars. For them we used the same sequence of one sky frame plus three object integrations. The difference here is the integration time, which was 10 s per individual integration, leading to a total on source time of 30 s. The same exposure time was used for the sky frames, associated with the stars. The sky fields for each cluster are located outside its tidal radius (see Table 4.2) and were checked by eye to be devoid of bright stars.

The final number of files that we have acquired within one OB is 37 frames for the

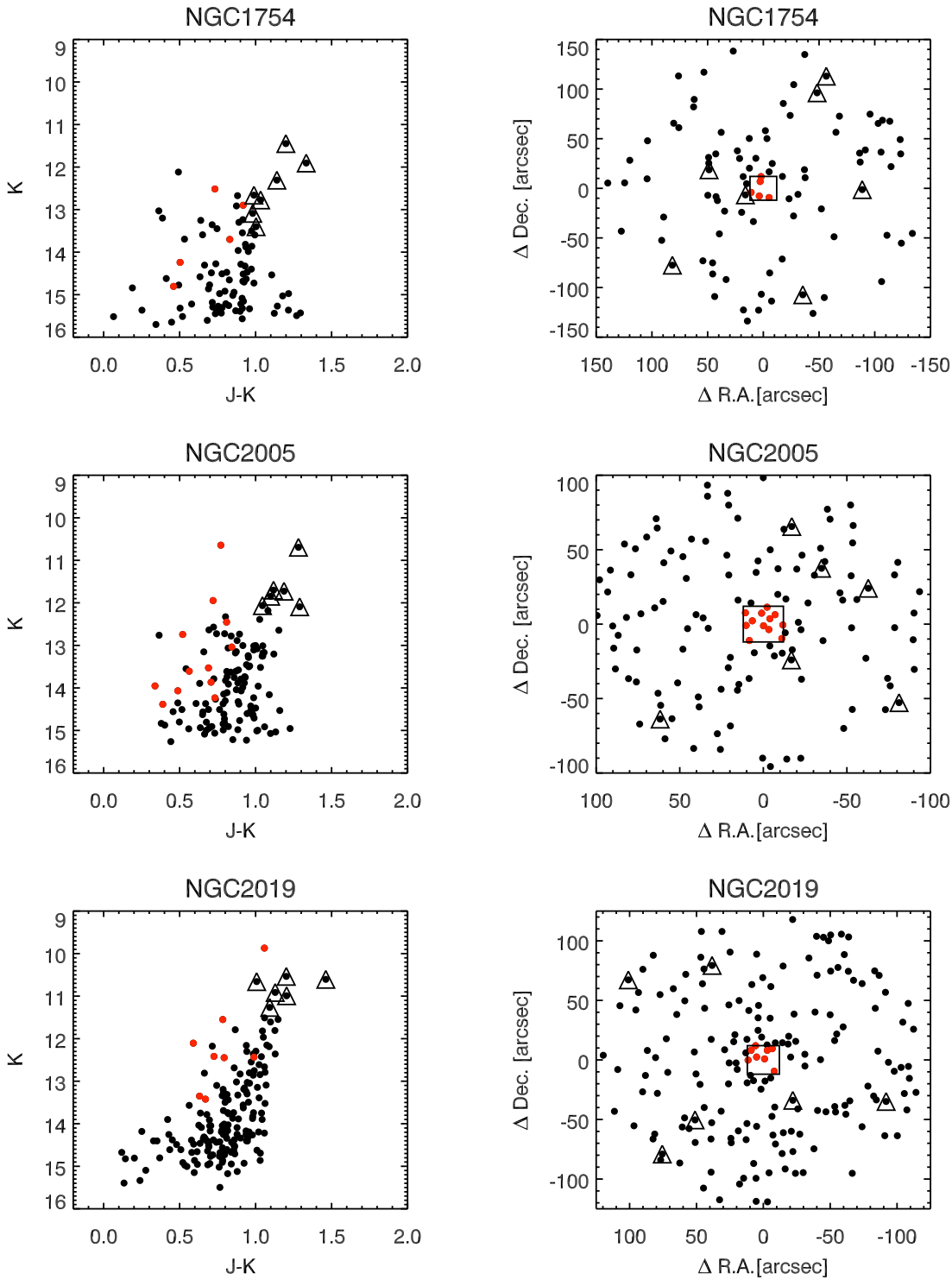

Figure 4.1: Colour-magnitude diagrams and spatial distribution of the bright stars, selected to be observed around the old and metal poor clusters. Magnitudes and positions are extracted from the 2MASS Point Source Catalogue (Skrutskie et al. 2006). The filled circles represent all the stars with reliable photometry located within the tidal radius of the clusters. The red filled circles represent the stars which are within the SINFONI 24″ × 24″ FoV, centred on the clusters. The triangular symbols mark the additional bright stars, which were observed.

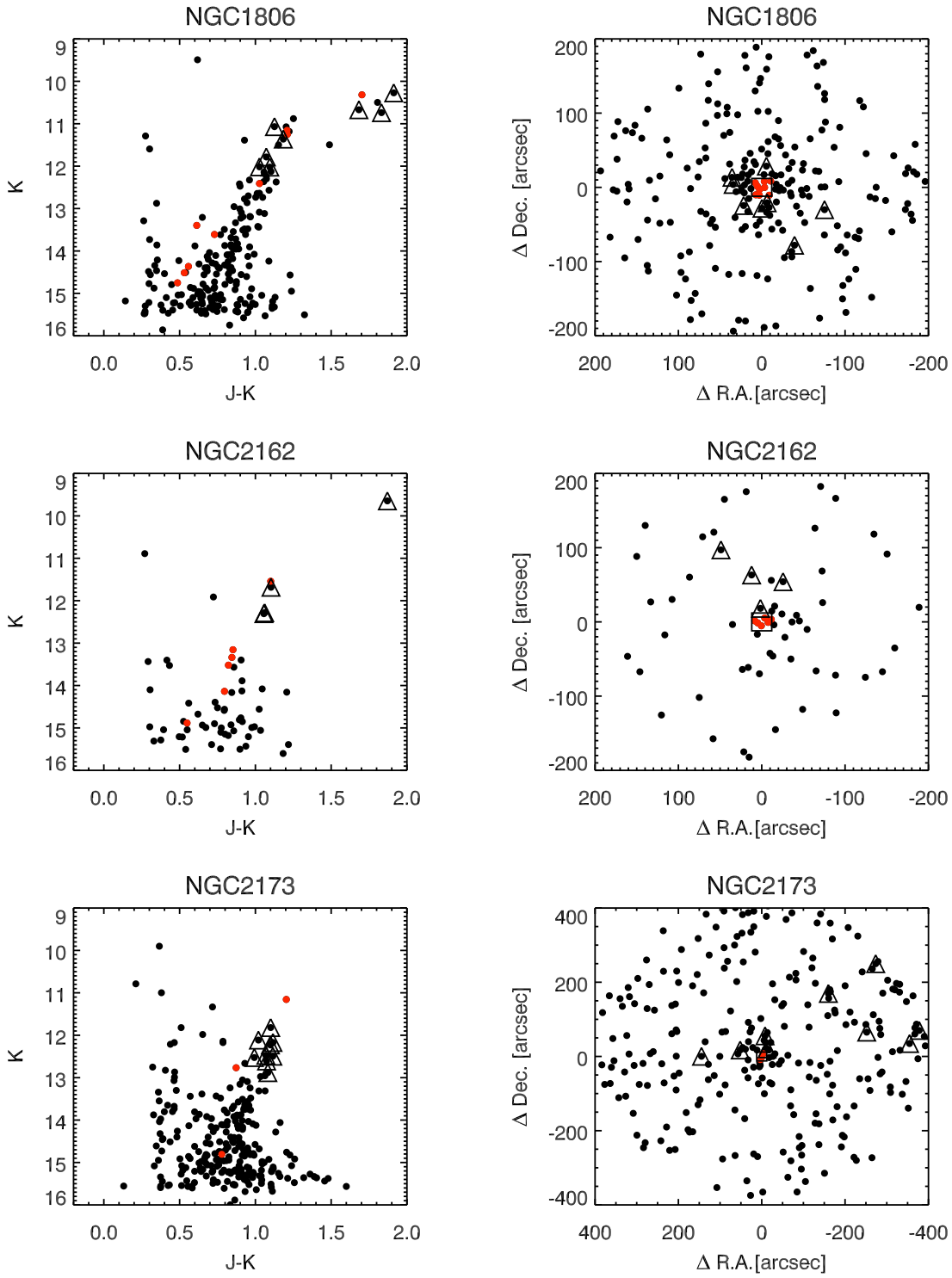

Figure 4.2: The same figure as Figure 4.1, but for the intermediate age and more metal rich clusters.

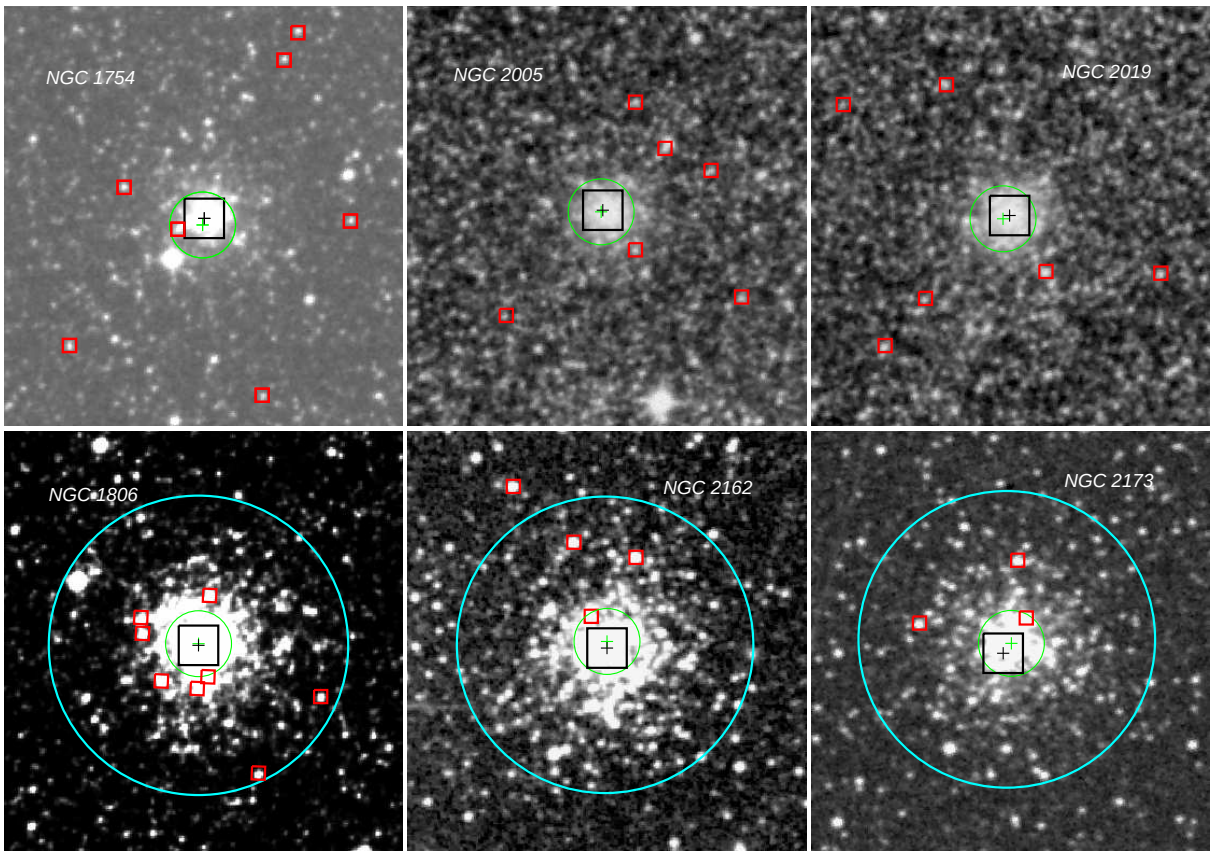

Figure 4.3: Optical *R*-band images of our cluster sample (taken from DSS). The black boxes and crosses represent our SINFONI 24″ × 24″ mosaic FoV and centring, respectively. The red squares mark the closest of the additional bright stars we have observed around each cluster. The green circles and crosses represent the 20″ radius aperture and the centre used in the photometry by Pessev et al. (2006). The cyan circles on the images of the intermediate age clusters (bottom line) represent the 90″ radius aperture of Mucciarelli et al. (2006). The size of each image is 3.′5 × 3.′5.

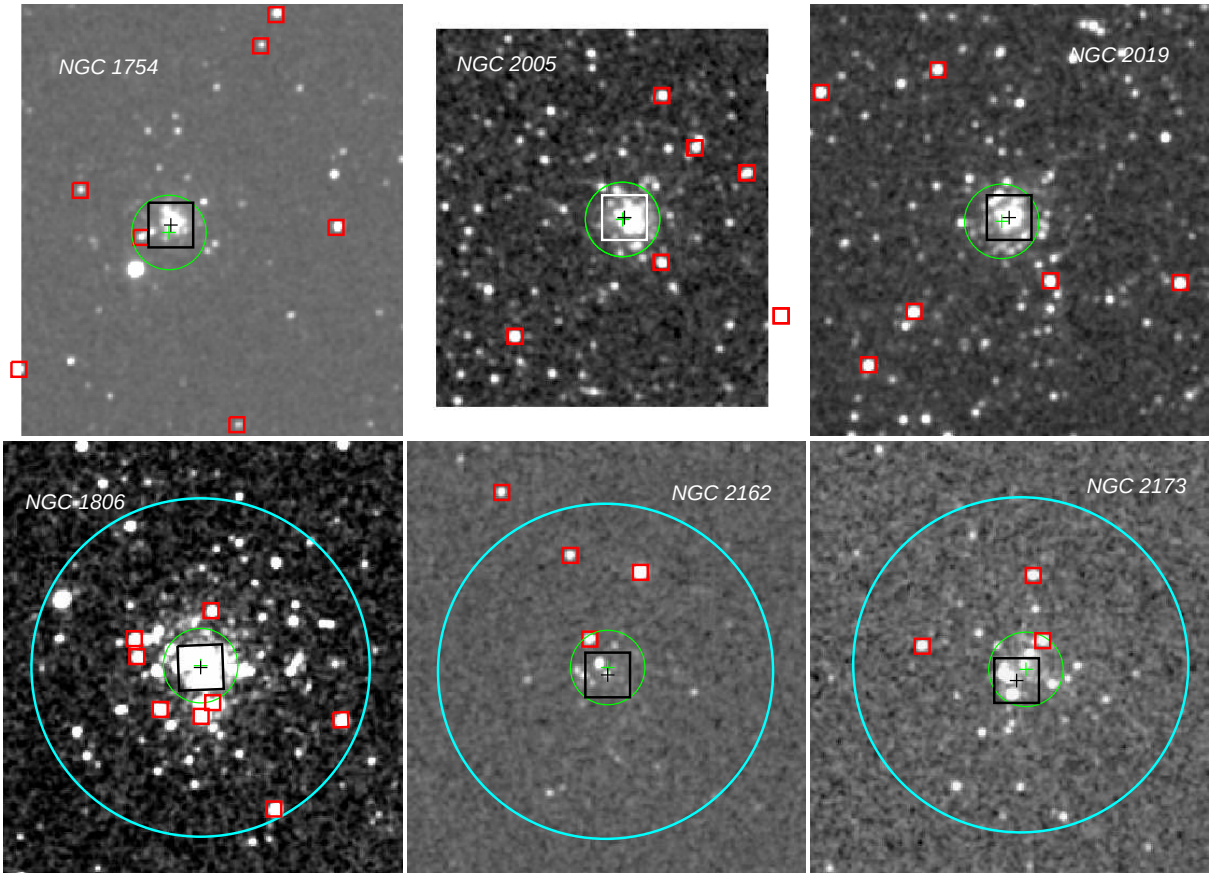

Figure 4.4: *K*-band 2MASS images of our cluster sample. Colour and symbol coding is the same as on Figure 4.3. North is up, east – to the left. Note the very bright star at south-east from the central SINFONI mosaic for NGC 1754. This star was identified as a foreground, Milky Way star, and was excluded from data analysis. Note also the difference between the optical, Figure 4.3, and near-IR images of the clusters. The image sizes are the same.

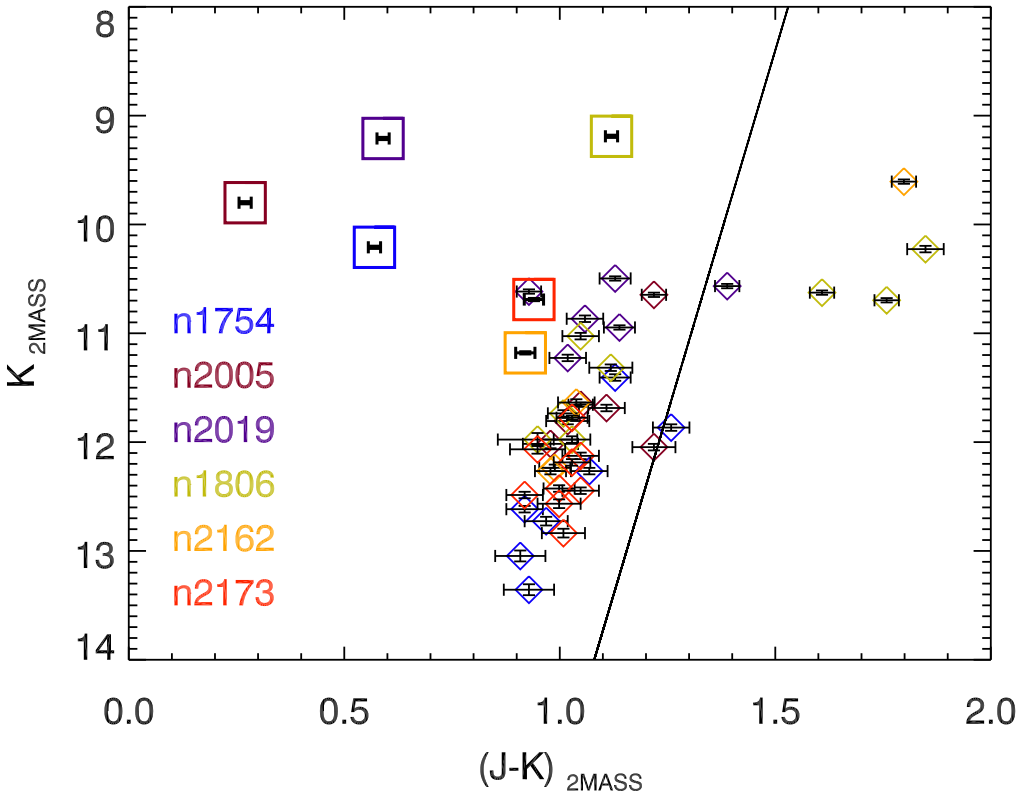

Figure 4.5: Colour-magnitude diagram for the additional stars and central mosaics of our sample. The photometry of the six GCs (coloured square symbols) comes from the catalogue by Pessev et al. (2006). Data about the additional bright stars (diamond symbols) come from the 2MASS Point Source Catalogue (Skrutskie et al. 2006). Colour coding of the symbols for the bright stars matches the cluster in whose vicinity they were observed.

central parts of each cluster (27 object exposures plus 10 sky exposures) and 4 frames for each additional star (3 star plus one sky). The total execution time for the longest OB did not exceed 1.5 hours. This gives us security that the telluric correction, derived from the telluric stars, observed after each OB (see Table 4.4) will be sufficiently accurate. The telluric stars were observed at similar airmass as the clusters.

4.3.2 Data reduction

In Section 2.4 we have already discussed the most important steps while reducing near-IR data. An overview of the resulting spectra after the different data reduction steps is shown in Figure 4.7. There we plot the raw spectrum, how it looks like after sky subtraction, the telluric spectrum (described in the next section) and the final, fully reduced one.

Basic data reduction was performed with the ESO SINFONI Pipeline v. 1.9.2, described in Section 2.5. Calibration products such as distortion maps, flat fields and bad pixel maps, were obtained with the relevant pipeline tasks ("recipes"). The input files have been retrieved from the SINFONI archive and are part of the general SINFONI calibration plan. To reduce the clusters and additional star data, we divided the OBs into cluster frames (the 27 object plus 10 sky exposures) and star frames (the 3 star exposures plus one sky per star). This is needed due to the different integration times for these two sub-sets. In principle, the pipeline is able to perform the data reduction for the whole sub-OB, consisting either of the cluster, or star frames just in one run. However, this is restricted by the RAM of the computer, which runs the pipeline and is quite time consuming. For example, on a PC equipped with 2048 MB RAM and an Intel Core2 2.7 GHz processor, the **sinfo_rec_jitter** recipe, which performs the full data reduction, needs ~1.5 hours to process 37 input frames and deliver a fully reduced, combined data cube.

Another argument against this straight forward data reduction is the fact that in this way we do not always achieve a good enough sky lines correction. This is why we preferred to reduce each mosaic pointing separately and combine them later. In this way we control the quality of each on source frame sky correction and where needed we tuned some of the parameters of the pipeline. In summary, we have fed the **sinfo_rec_jitter** recipe with data sets, consisting of one mosaic pointing (3 on source integrations plus 2 bracketing "skies") and the needed calibration files. Then the recipe extracts the raw data, applies distortion, bad pixels and flat-field corrections, wavelength calibration, and stores the combined sky-subtracted spectra in a 3-dimensional data cube. The same pipeline steps were also used to reduce the observations of the additional bright stars and telluric stars.

The main difficulty during the sky corrections arises from the fact that our observations were sky dominated, combined together with the small amount of flux in some of the frames. For these cases we have found that by appropriately setting the `--skycor-llx`, `--skycor-lly`, `--skycor-urx` and `--skycor-ury` parameters

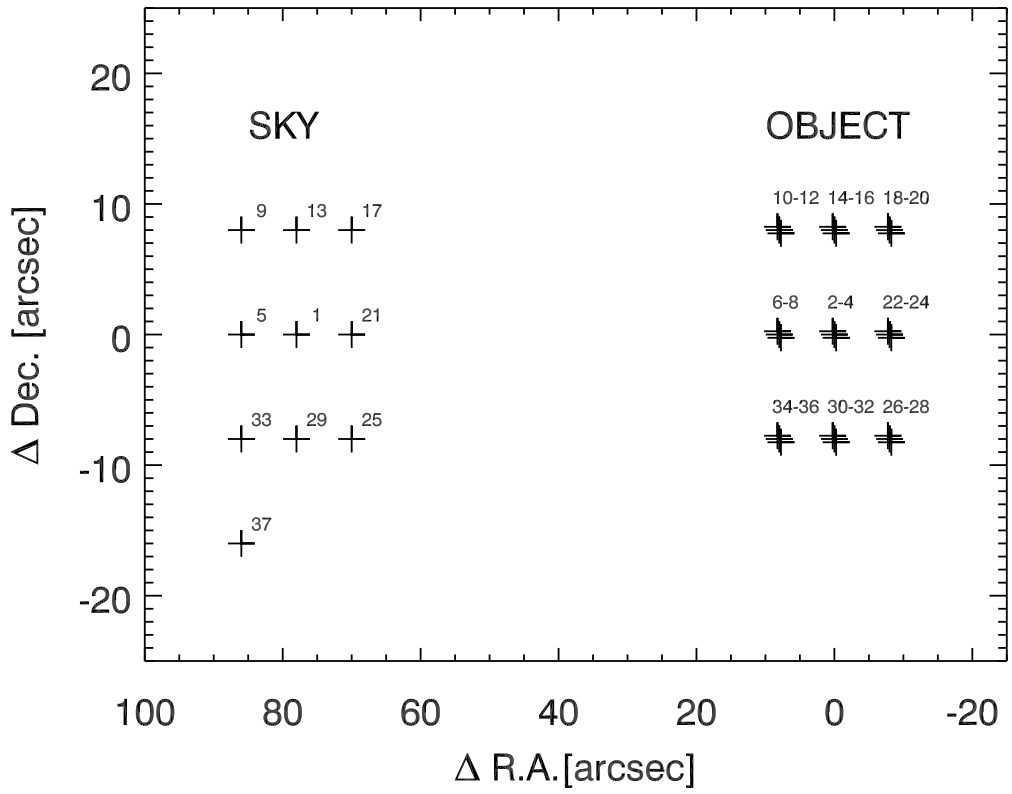

Figure 4.6: Schematic view of the mosaic pattern used to observe the centres of the globular clusters. Each cross represents one SINFONI integration. The sky fields are located outside the tidal radius of the clusters. For this plot we have reduced the distance to the sky field for the sake of clarity of the graphic.

Table 4.3: Additional field RGB and AGB stars observing log.

Name	R. A.	Dec.	K	$(J-K)$	Cluster
(1)	(2)	(3)	(4)	(5)	(6)
2MASS J04540127-7026341	73.505318	-70.442825	11.449	1.199	NGC 1754
2MASS J04540771-7024398	73.532158	-70.411079	11.906	1.333	″
2MASS J04543522-7027503	73.646779	-70.463989	12.308	1.140	″
2MASS J04542864-7026142	73.619361	-70.437286	12.774	1.033	″
2MASS J04540935-7024566	73.538986	-70.415741	13.089	0.981	″
2MASS J04541188-7028201	73.549526	-70.472260	13.402	1.003	″
2MASS J04540536-7025202	73.522358	-70.422279	13.502	0.974	″
2MASS J05302221-6946124	82.592574	-69.770134	10.694	1.282	NGC 2005
2MASS J05300708-6945327	82.529509	-69.759094	11.701	1.118	″
2MASS J05295466-6946014	82.477772	-69.767067	11.726	1.187	″
2MASS J05300704-6944031	82.529344	-69.734200	11.845	1.099	″
2MASS J05300360-6944311	82.515028	-69.741997	12.065	1.045	″
2MASS J05295822-6944445	82.492596	-69.745720	12.093	1.290	″
2MASS J05320670-7010248	83.027934	-70.173569	10.536	1.202	NGC 2019
2MASS J05313862-7010093	82.910920	-70.169266	10.606	1.462	″
2MASS J05315232-7010083	82.968035	-70.168999	10.658	1.007	″
2MASS J05321152-7010535	83.048034	-70.181534	10.914	1.129	″
2MASS J05321647-7008272	83.068648	-70.140907	10.992	1.204	″
2MASS J05320418-7008151	83.017435	-70.137543	11.266	1.093	″
2MASS J05021232-6759369	75.551343	-67.993591	10.272	1.913	NGC 1806
2MASS J05020536-6800266	75.522366	-68.007416	10.671	1.683	″
2MASS J05015896-6759387	75.495707	-67.994102	10.739	1.832	″
2MASS J05021623-6759332	75.567629	-67.992561	11.069	1.126	″
2MASS J05021870-6758552	75.577939	-67.982002	11.363	1.184	″
2MASS J05021846-6759048	75.576934	-67.984673	11.784	1.072	″
2MASS J05021121-6759295	75.546733	-67.991539	12.017	1.027	″
2MASS J05021137-6758401	75.547393	-67.977821	12.023	1.095	″
2MASS J06002748-6342222	90.114520	-63.706192	9.647	1.871	NGC 2162
2MASS J06003156-6342581	90.131523	-63.716152	11.684	1.103	″
2MASS J06003316-6342131	90.138168	-63.703663	12.283	1.061	″
2MASS J06003869-6341393	90.161217	-63.694271	12.307	1.056	″
2MASS J05563892-7258155	89.162190	-72.970978	11.819	1.101	NGC 2173
2MASS J05575667-7258299	89.486158	-72.974976	12.114	1.020	″
2MASS J05570233-7257449	89.259709	-72.962486	12.171	1.116	″
2MASS J05575784-7257548	89.491014	-72.965248	12.229	1.099	″
2MASS J05563368-7257402	89.140358	-72.961189	12.474	1.069	″
2MASS J05581142-7258328	89.547613	-72.975800	12.495	1.115	″
2MASS J05583257-7258499	89.635732	-72.980530	12.526	0.993	″
2MASS J05572334-7256006	89.347255	-72.933517	12.609	1.074	″
2MASS J05565761-7254403	89.240070	-72.911217	12.881	1.082	″

Notes: (1) 2MASS catalogue star name, (2) and (3) stellar coordinates, (4) K-band magnitude, (5) $(J-K)$ colour (all data as listed in the 2MASS Point Source Catalogue), (6) cluster, next to which the star was observed.

(these indicate the edges of the object spectrum location), we can achieve a better sky correction.

4.3.3 Telluric corrections

The next data reduction step is to remove the absorption lines originating in the Earth's atmosphere. These lines are especially deep in the blue part of the *K*-band (blue-wards from 2.1 μm). For this purpose we observed after each science target a telluric star, which is of hotter spectral type (usually AV – BV, see Table 4.4). Since these stars are hot stars, we know that their continuum in the *K*-band is well approximated by the Rayleigh-Jeans part of the black body spectrum, associated with their effective temperature. They show only one prominent feature, the hydrogen Bracket γ absorption line at 2.166 μm. For each telluric star spectrum first we modelled this line with a Lorentzian profile, with the help of the IRAF task `splot`, and then subtracted the model from the star's spectrum. Then we divided the cleaned star spectrum by a black body spectrum with the same temperature as the star to remove its continuum shape. Thus we obtained a normalised telluric spectrum. The last step before applying it to the science spectra was to scale and shift in the dispersion direction each telluric spectrum for each data cube by a small amount (< 0.5 pix, 1 pix = 2.45 Å) to minimise the residuals of the telluric lines. We performed this with the help of an IRAF script, written by D. R. Silva (for more details see Silva et al. 2008). As an input to the script we provided 1D spectrum, extracted from each data cube, the relevant telluric spectrum and the wavelength region, where the cross-correlation of the two spectra should be done. For this purpose we selected the region where the telluric absorption features are especially deep, 1.99 – 2.08 μm. After that each individual cluster mosaic and star data cube was divided by the so optimised telluric spectrum. In this way we achieved also a relative flux calibration.

One telluric star, HD 44533, used for the telluric correction of NGC 2019 and its surrounding stars, has an unusual shape of the Bracket γ line. It seems to have also some emission together with the absorption. To remove it, we interpolated linearly the region between 2.1606 and 2.1706 μm. In this region there are not many strong telluric lines, however this interpolation will reflect in an imperfect correction of the science spectrum.

4.3.4 Cluster light integration

As a result from the previous data reduction steps we obtained fully calibrated data cubes, where the signatures of the instrument and the night sky are removed as well as possible. At this stage we have one data cube for each additional star and one data cube per telescope pointing on the mosaic for the clusters. The next step is to reconstruct the full mosaic of each cluster. For example, Figure 4.8 shows the reconstructed image of the cluster NGC 1754, together with a 2MASS *K*-band image for comparison. In this image we still see the imprints of the edges of the individual pieces of the mosaic. On

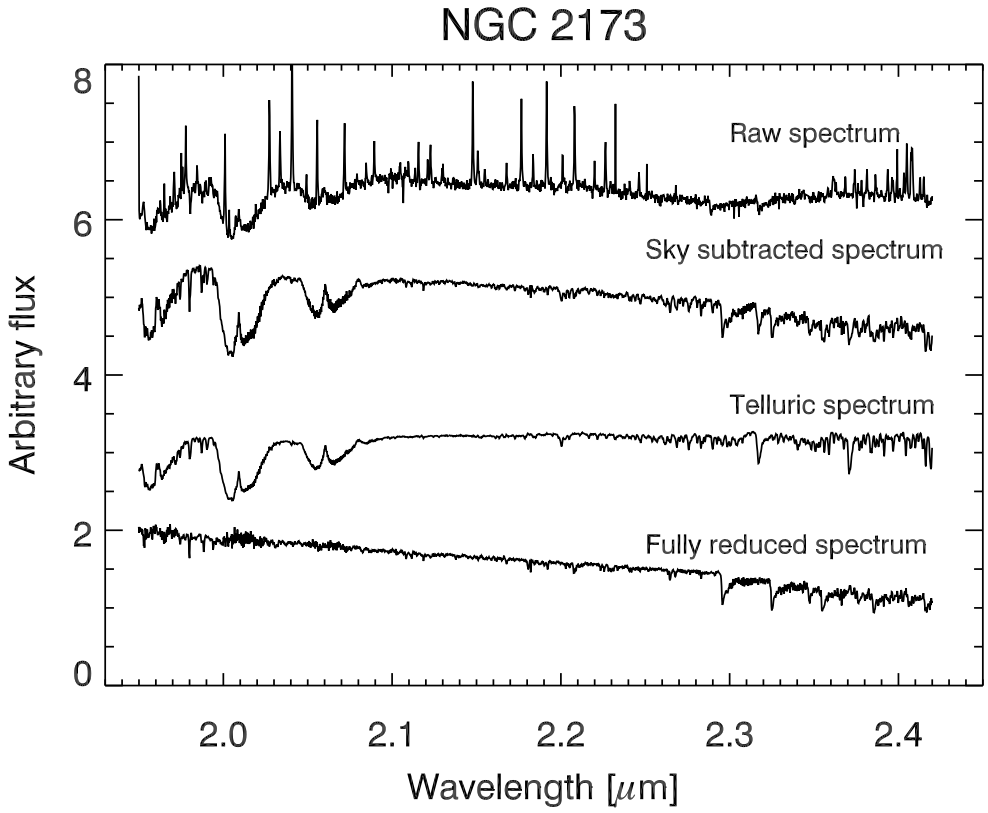

Figure 4.7: Overview of the data reduction steps, applied to obtain fully reduced spectra (in this case, the LMC globular cluster NGC 2173). *From top to bottom*: (1) Raw spectrum, (2) Sky subtracted spectrum after running the SINFONI pipeline. (3) Telluric correction, used to remove the telluric absorption features. (4) Fully reduced spectrum, used for analysis. All data reduction steps have been performed to the full data cubes and then, after the telluric correction, integrated spectra have been derived.

Table 4.4: LMC telluric stars observing log.

Name	Cluster	R. A.	Dec.	SpT
(1)	(2)	(3)	(4)	(5)
HD 40624	NGC 1754	05:54:56.97	-65:53:00.65	A0V
HD 43107	NGC 2005	06:08:44.26	-68:50:36.27	B8V
HD 44533	NGC 2019	06:14:41.94	-73:37:35.44	B8V
HD 42525	NGC 1806	06:06:09.38	-66:02:22.63	A0V
HD 45796	NGC 2162	06:24:55.79	-63:49:41.32	B6V
HD 46668	NGC 2173	06:27:13.64	-73:13:42.08	B8V

Notes: (1)Telluric star name, (2) Cluster for which this star was used, (3) and (4) Coordinates of the star, as listed in Simbad (July 2008), (5) Spectral type.

both images, the 2MASS and even better on the SINFONI image, we see individual stars, which we can extract and study separately.

However, in this project we are not interested in resolving individual stars within the clusters as much as in obtaining luminosity weighted, integrated spectra for each cluster, in order to be able to compare with stellar population models. To achieve this, we first estimated the noise level in each reconstructed image from the mosaic data cube. We consider this noise is due to residuals after the sky background correction. Thus we computed the median residual sky noise level and its standard deviation, after clipping all data points with intensities more than 3σ (assuming that these are the pixels, which contain the star light from the cluster). After that we selected all spaxels, which have intensity more than three times the standard deviation above the median residual sky noise level. We summed them up and normalised to 1 s exposure time. An overview of the final integrated cluster spectra is shown on Figure 4.9. In some of the spectra (NGC 1754 and NGC 2019), we still suffer from sky line residuals, originating from the addition of imperfectly sky corrected spaxels (this may happen with intrinsically low intensity spaxels). In these cases we interpolated the contaminated regions by hand.

Our observations were carried out in service mode with constraint sets allowing seeing up to 2″. For individual stars this led to a failure of the standard recipe, while extracting 1D spectra. Moreover in some cases in the field-of-view there were also other stars. Thus we decided to manually control the selection of star light spaxels. We used the same method, as for the central clusters mosaics, to obtain the spectra of the additional stars.

4.3.5 Error handling

Unfortunately the SINFONI pipeline does not provide error estimates, which carry information about the error propagation during the different data reduction procedures. Thus we have to use empirical ways of computing the errors. For this purpose we derived a wavelength dependant signal-to-noise ratio (S/N) for each cluster integrated spectrum using the empirical method described by Stoehr et al. (2007). This method computes the signal in a given spectrum as the median value of the flux. To derive the noise, first the median absolute difference of the flux values is computed and then it is converted to the standard deviation of the Gaussian (i.e. the desired noise measurement). The noise is assumed to be uncorrelated for nearby flux values and of approximately Gaussian distribution. The final S/N ratio is computed by dividing the signal by the noise.

In this way we have computed the S/N in 200 pixels width bins from the science spectra (corresponding to 0.049 μm wavelength intervals). Then we fitted a linear function to the S/N values in the range $2.1-2.4\,\mu$m where all of the spectral features of interest reside. The error spectrum for each cluster and star was derived by dividing the science spectrum by the so prepared S/N function (for illustration see Figure 4.10). The selection of the bin width was made after experimenting with a few smaller and larger values. In the case of bin widths of 50 or 100 pixels (0.01225 or 0.0245 μm, respectively), the S/N function becomes very noisy. Choosing wider, 300 or 400 pixels bins

flattens the features of the S/N function. In general the S/N decreases with increasing wavelength. This is due to the combination of the spectral energy distribution and the instrument + telescope sensitivity.

4.3.6 Bright AGB stars – cluster members or not?

As discussed in Section 4.2 one of the main problems, when one tries to compile an integrated spectrum of a globular cluster, is the stochastic sampling of bright AGB stars for clusters with modest luminosities. As an example, Renzini (1998) shows that a stellar cluster with $10^5 L_\odot$, solar metallicity and age of 15 Gyr will have about 1200 red giant branch stars (RGB), 30 early asymptotic giant branch stars (E-AGB), and 2 thermally pulsating asymptotic giant branch (TP-AGB) stars. The latter stellar evolutionary phases are particularly important since up to 40% of the total K-band light of a stellar population originates there (Renzini & Fusi Pecci 1988; Maraston 2005). In general, with our observations we sample a good fraction of the light coming from the old clusters (NGC 1754, NGC 2005 and NGC 2019), $\sim 3 - 7 \times 10^4 L_\odot$ (lower limit). Moreover, they are massive and well concentrated, with half-light radii sampled with our SINFONI mosaics. However, we are not performing that well with the intermediate age clusters, where for two of them, NGC 2162 and NGC 2173, we sample even less than $10^4 L_\odot$ (see Table 4.2). Our observations are intrinsically affected by statistical fluctuations in the number of bright stars, due to the modest luminosities of the young clusters. They are not as concentrated, have smaller masses and thus mass segregation, which makes the most massive (and most luminous in the near-IR) stars settle down close to the centre, might have not been effective enough, and thus some of the bright stars may be located at larger radii.

In order to have as complete as possible spectra we observed a number of additional bright stars with near-IR colours and magnitudes in the range expected for AGB stars, located outside of the central mosaics, but still within the tidal radii of the clusters, and checked weather some of them belong to the clusters. The location of the closest ones is shown on Figure 4.4. According to this figure the majority of the clusters' light lay within the SINFONI FoV for most of the clusters. However, two of them, NGC 2162 and NGC 2173, are poorly populated and there is a possibility that their AGB stars are not sampled by our SINFONI mosaics. NGC 1806 in contrast is relatively rich and has a number of bright stars located just outside of the SINFONI mosaic.

We can probe the membership of a given star in two ways. The first criterion is its proximity to the cluster centre, but one does not have to forget that a fore- or background star might also have relatively nearby position due to projection effects. We can gain more confidence by exploring the radial velocities of the nearby stars and the cluster under study. For this purpose we also need to know the observed velocity dispersions of the stars in the clusters. For the old clusters (NGC 1754, NGC 2005 and NGC 2019) we have taken these values from the study of Dubath et al. (1997). They have measured core velocity dispersions from integrated optical spectra, covering the central $5'' \times 5''$ of each cluster. The values are $7.8 \pm 3.0\,\mathrm{km\ s^{-1}}$ for NGC 1754, $8.1 \pm 1.3\,\mathrm{km\ s^{-1}}$ for NGC 2005 and $7.5 \pm 1.3\,\mathrm{km\ s^{-1}}$ for NGC 2019. For the intermediate-age clusters we could not find similar observed velocity dispersions in the literature,

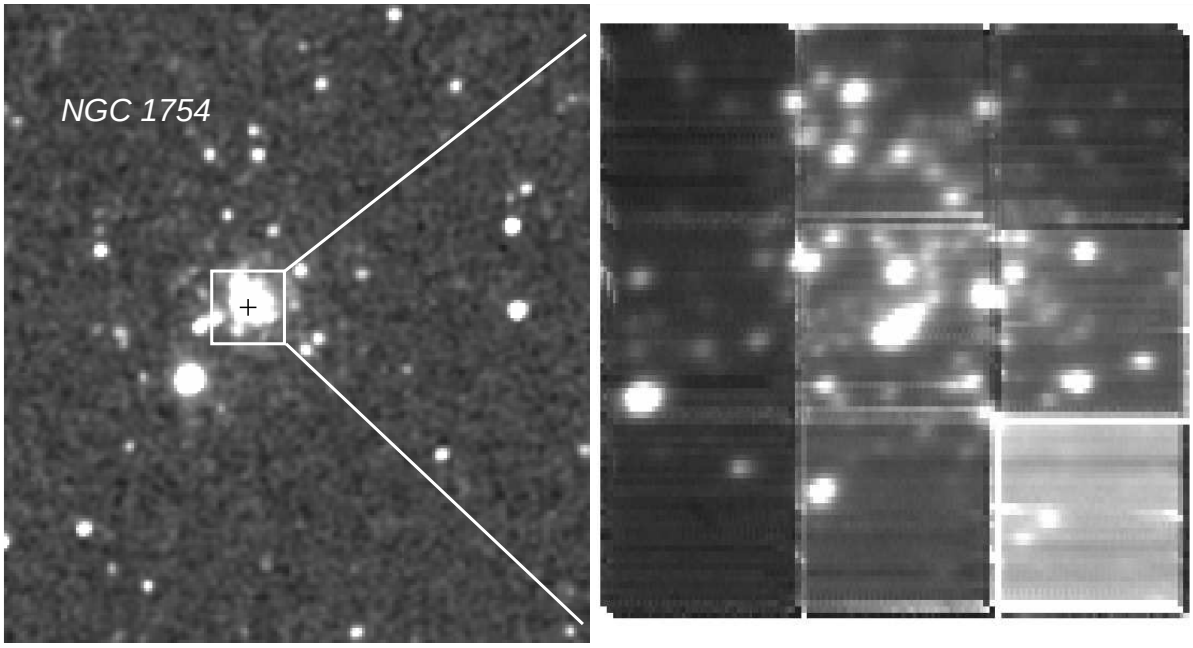

Figure 4.8: Two views of NGC 1754 in the *K*-band. The left image is from the 2MASS Extended Source Catalogue (Skrutskie et al. 2006). The white square marks the field, which our SINFONI mosaic observations cover (24″ × 24″). The right picture is a reconstructed image of the data cube, built up from the SINFONI observations.

so we used the predicted line-of-sight velocity dispersion at the centre of the cluster by McLaughlin & van der Marel (2005). The $\sigma_{p,0}$ that they have calculated is based on the solution of Poisson's and Jeans' equations for a King (1966), power-law or Wilson (1975) model, which yields a dimensionless $\sigma_{p,0}/\sigma_0$. σ_0 can be expressed with the help of the fitted central mass density and the radial scale of the model. In this way the predicted observable dispersion follows immediately. The numbers are 1.1 km s^{-1} for NGC 2162 and 2.0 km s^{-1} for NGC 2173. We did not find a similar estimate for NGC 1806, so we used an arbitrary conservative value of 8 km s^{-1}.

Old and metal poor clusters

We will first discuss the three old clusters, NGC 1754, NGC 2005 and NGC 2019. Figure 4.11 shows the distribution of the stars around these clusters and their radial velocities, measured from our data. The velocity of each cluster, as inferred from our data and uncorrected for heliocentric motion, is shown with a solid line. The horizontal dashed line gives our 1σ velocity measurement error, while the dash-dotted line shows the levels where the velocity of the cluster is higher or lower than 3 times its velocity dispersion. For guidance we have shown also the location of the half-light radii with vertical dotted lines and the tidal radii with vertical dashed lines. We cannot exclude any star around any cluster, according to this plot, bearing in mind their 3σ velocity errors (the error bars, shown on the plot are 1σ errors). However, we see that some of the brightest stars that we have observed are located closer to the clusters tidal radii,

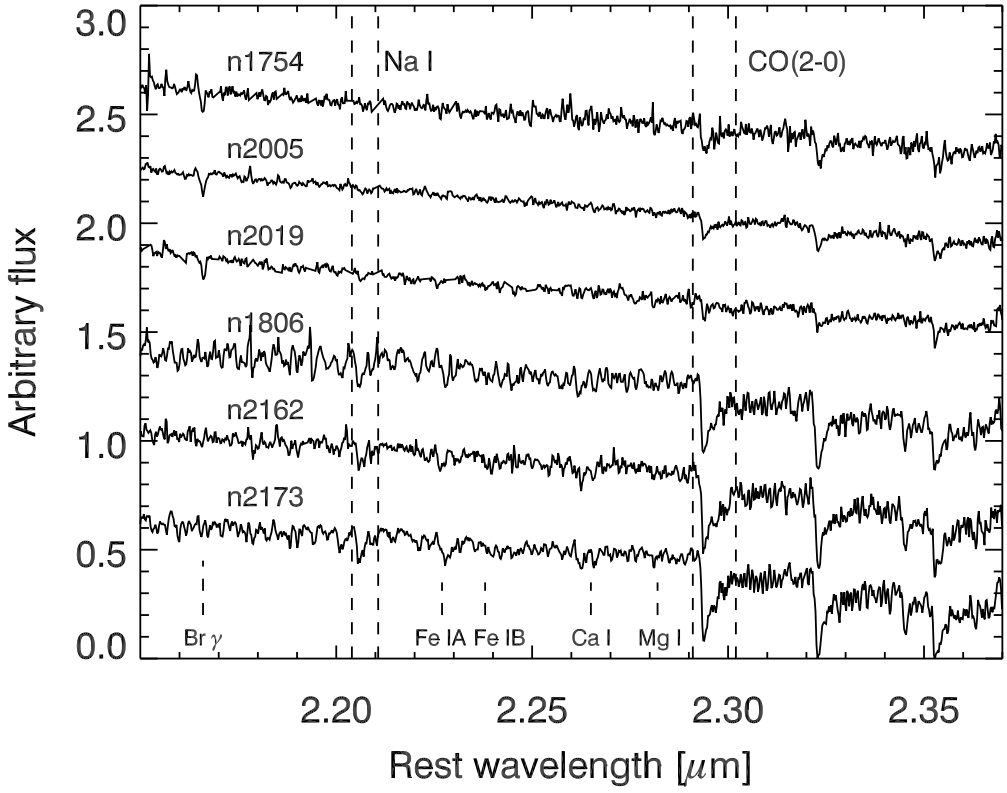

Figure 4.9: Luminosity weighted spectra of the six globular clusters in our sample, integrated over the central 24″ × 24″ (see Figure 4.8). The upper three clusters (NGC 1754, NGC 2005 and NGC 2019) are metal poor ([Z/H]~ −1.4) and old (> 10 Gyr). The lower three (NGC 1806, NGC 2162 and NGC 2173) are more metal rich ([Z/H]~ −0.4) and younger (< 2 Gyr). The vertical dashed lines show the extent of the central passbands of the Na I and ^{12}CO (2–0) features. The position of other lines are also indicated at the bottom.

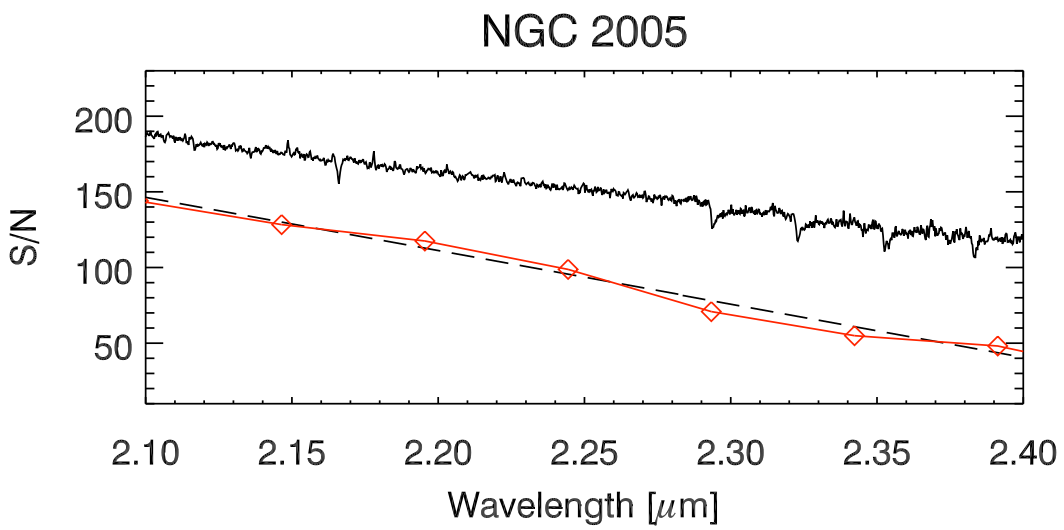

Figure 4.10: Example of the method, which we used to compute error estimates. The red diamonds represent the values of the S/N ratio in every 200 pixels bin (0.049 μm). connected by a red solid line. The dashed line shows the linear fit to the S/N function in the region 2.1 – 2.4 μm. For guidance the integrated spectrum of NGC 2005 is shown in arbitrary units. The error spectrum was derived after the cluster spectrum was divided by the linear fit to the S/N function (dashed line).

than the centres. This is unexpected for old clusters, which have already undergone a core collapse and have their most massive stars concentrated towards the centre of the cluster. Indeed, Mackey & Gilmore (2003) classify the old clusters in our sample as potential post-core-collapse clusters, due to the very well expressed power-law cusps in their centres.

Looking at Figure 4.15, which shows the $(J - K)$ colour of all of the objects in our sample versus their ^{12}CO (2–0) line strength, we see that NGC 2005, denoted with the dark red square, has a blue colour and a low ^{12}CO (2–0). The corresponding stars, plotted with the same colour, have $(J - K)$ and ^{12}CO (2–0) much higher than the cluster and closer to the values for the rest of our sample. This leads us to the conclusion that the additional bright stars, that we observed around NGC 2005, are not likely to be cluster members. In the following we consider these stars as members of the LMC field population and reach the conclusion that the velocity resolution of our observations in not good enough to track the small radial velocity differences between the LMC globular clusters and the field stars in their vicinity.

Similar conclusions can be drawn for the other two old clusters, NGC 1754 and NGC 2019. The bright star just outside the SINFONI filed-of-view for NGC 1754 on Figure 4.4 might be a cluster member, but the S/N of its spectrum is too low (~ 10) and adding it to the final integrated cluster spectrum would not increase the total S/N.

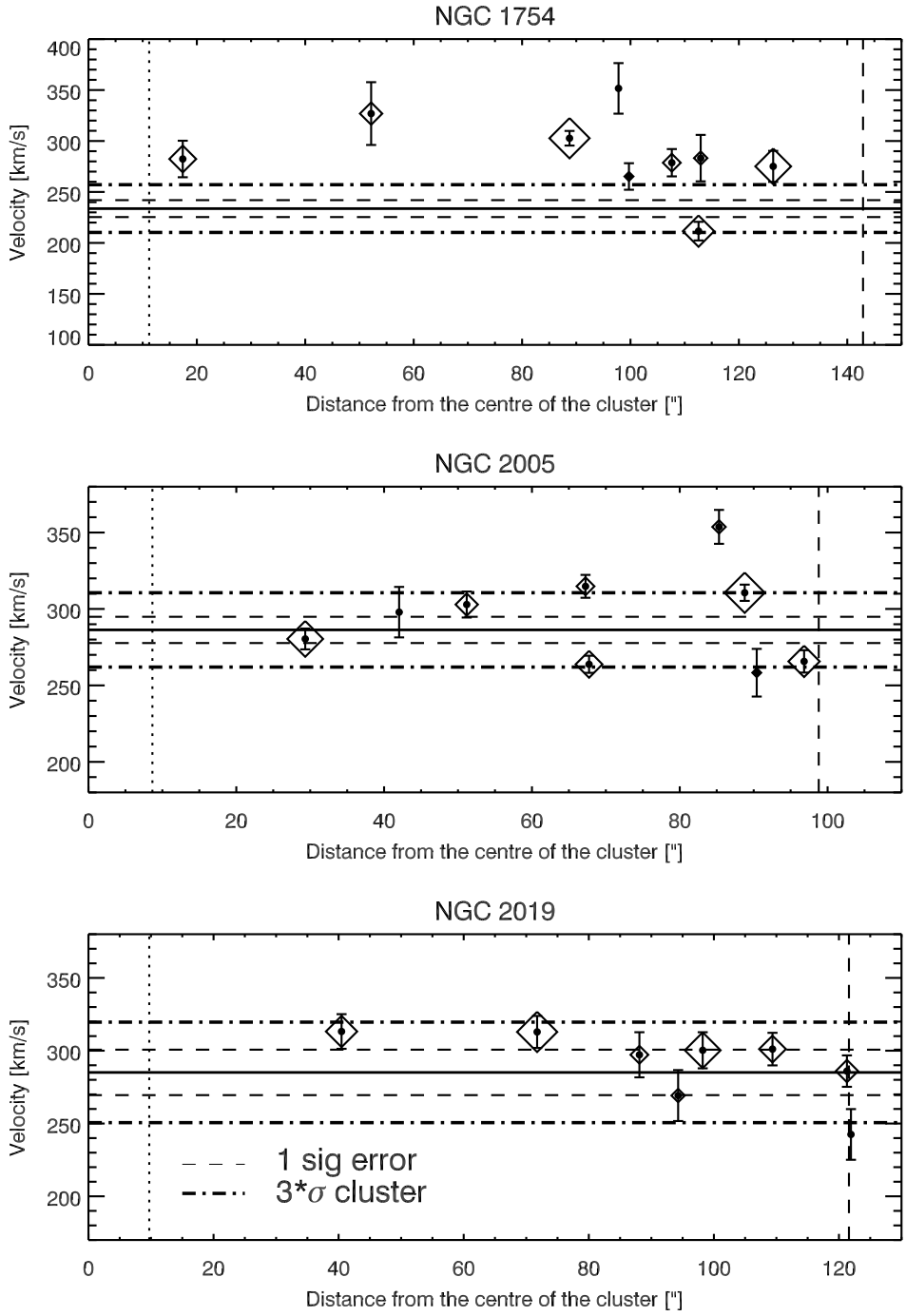

Figure 4.11: Radial velocities (v_r) of the stars observed in the vicinity of the old clusters as a function of their distance from the cluster's centre. The v_r of the cluster, as derived from our data and uncorrected for the heliocentric motion, is denoted with a solid line. 1σ error of the measurement is shown with dashed lines. The dash-dotted lines represent the levels with three times the velocity dispersion of the cluster. The diamond symbols represent the individual stars. The symbol size is proportional to the luminosity of the star (the largest for the brightest). Vertical dotted lines indicate the half-light radius, vertical dashed lines – the tidal radius.

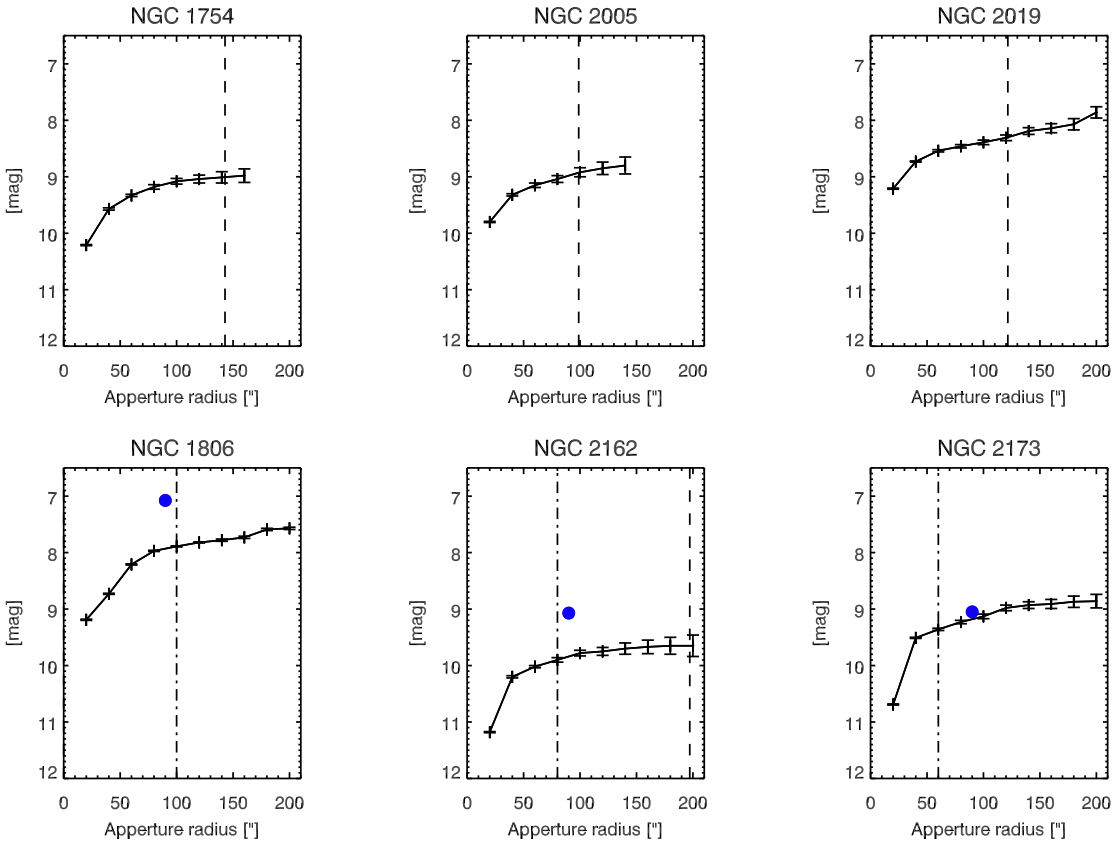

Figure 4.12: *K*-band 2MASS aperture photometry of the six LMC GCs, taken from the catalogue of Pessev et al. (2006). The dashed vertical lines show the extent of the tidal radius of the clusters (see Table 4.2, for NGC 1806 it is unknown, for NGC 2173 $r_t \sim 400''$). The dash-dotted lines in the plots of the three intermediate age clusters (NGC 1806, NGC 2162 and NGC 2173) show the radial distance of the farthest added star to the central mosaics' spectra. The blue filled circles represents the 90″ radius aperture photometry, obtained by Mucciarelli et al. (2006).

Intermediate age clusters

This sub-sample includes the clusters NGC 1806, NGC 2162 and NGC 2173. The last two of them are poorly populated as seen in near-IR light, visible from Figure 4.4, so in their cases the potential inclusion of additional bright stars to the central mosaic is very important for the total cluster light sampling. A detailed photometric study of the RGB and AGB stars in these clusters is available from Mucciarelli et al. (2006). Based on near-IR colour-magnitude diagrams and after decontamination from the field population, they report the number of the stars in these evolutionary phases, as well as their luminosity contribution to the total light of the clusters. They consider all stars brighter than $K \approx 12.3$, which represents the level of the RGB tip (Ferraro et al. 2004), and $(J-K)$ between 0.85 and 2.1 to be AGB stars. The AGB stars further separate in oxygen rich (M-stars) and carbon rich (C-stars). An AGB star becomes C-rich, when the amount of dredged up carbon into the stellar envelope exceeds the amount of oxygen. Then all the oxygen is bound into CO molecules. The remaining carbon is used to form CH, CN and C_2 molecules. This process is more effective in more metal poor stellar populations, thus they are expected to have more C-stars (Maraston 2005). C-stars are important members of intermediate age globular clusters, since their contribution can reach up to 60 % of the total cluster luminosity (Frogel et al. 1990). Another important statement, that Frogel et al. (1990) make, is that C and M type stars are found both in clusters and in the LMC field. Thus it is very difficult to separate cluster stars from the field population. Figure 4.12 gives a very good illustration of this problem. There we plot the K-band curves of growth of the aperture photometry preformed by Pessev et al. (2006) for all of the clusters in our sample. The bottom line of the plots also includes the K-band magnitude, integrated up to 90″ from the clusters' centres in the case of the intermediate age clusters, taken from Mucciarelli et al. (2006). The discrepancy between the two studies is larger in the case of the clusters of SWB type V (NGC 1806 and NGC 2162). According to Frogel et al. (1990) the total light of such clusters is dominated by a few bright stars on the AGB, which very often are carbon stars. In these cases it seems that Pessev et al. (2006) have over-estimated the LMC field contribution to the total cluster light and removed the very bright and red carbon stars from the clusters. To support this hypothesis we can perform a simple test with NGC 2162. According to Mucciarelli et al. (2006) the cluster light is dominated by one single carbon star (more details will be given in the discussion about this cluster bellow). By adding the K magnitude of this star, taken from 2MASS, to the integrated magnitude of the cluster, taken from Pessev et al. (2006), we obtain a final K-band magnitude very close to the one, reported by Mucciarelli et al. (2006). The inclusion of bright stars affects also the colour of the cluster as well. The $(J-K)$ colours, measured by Pessev et al. (2006) are bluer for these two clusters in comparison with the ones, listed by Mucciarelli et al. (2006) and are again bluer than the SSP model predictions for $(J-K)$, made by Maraston (2005). These models have been calibrated with the help of LMC globular clusters data from Frogel et al. (1990). Moreover, as we discuss bellow, the LMC field carbon stars contamination is not expected to be very high at the locations of these clusters. The upper limits, according to the carbon stars frequency maps of Blanco & McCarthy (1983) are of the order of 0.06 up to 0.7 C-type stars for

an area with radius 100″. This leads us to the conclusion that Pessev et al. (2006) have over-estimated the carbon stars field contamination in the case of clusters with SWB type V. For further comparisons of our spectra with photometry we will use the data of Mucciarelli et al. (2006) and integrate bright stars, according to their criteria.

NGC 1806: This cluster is relatively rich in stars, as seen on Figure 4.4. However, there is a lack of information about its spectral properties. So far studies of the stellar populations have been made mainly with photometric methods (e.g. Frogel et al. 1990; Dirsch et al. 2000; Mucciarelli et al. 2006; Mackey et al. 2008), although two bright cluster stars have been observed by Olszewski et al. (1991) to spectroscopically estimate the metallicity of the cluster. Moreover, there is neither information about its dynamical properties in the literature, nor information about its bounds. Thus we have to chose an arbitrary limiting radius for the bright stars integration.

Mucciarelli et al. (2006) point out the presence of 75 RGB stars and 9 AGB stars, from which 4 are carbon rich stars, in a radius of 90″ from the centre of the cluster. Judging from the integrated SINFONI mosaic spectrum on Figure 4.9 we see the signature of a carbon star. It consists of many spikes, which are not due to noise or bad sky correction, but are real absorption features, which also lead to a flatter continuum shape (see Figure 3.1). Indeed, looking at the spectra of the resolved stars in our SINFONI mosaic data cube for this cluster, we identified one of the stars as C-type. The velocity distribution of the additional bright stars inside 100″ radius is shown on Figure 4.13, top panel. The three brightest stars are also C-type. Thus we decided to integrate all the stars within the 90″ radius used by Mucciarelli et al. (2006), with the exception of the seventh and eighth stars from the cluster's centre due to low S/N spectra.

NGC 2162: Inside the aperture photometry radius of 90″, that Mucciarelli et al. (2006) have used, there is a very bright carbon star with $K = 9.65^m$ and $(J - K) = 1.87$ (magnitude and colour taken from the 2MASS Point Source Catalogue). It is visible on Figure 4.4 at $\sim 50''$ away from the cluster's centre, above and to the right, as well as on the colour-magnitude diagram in Figure 4.2 as the brightest and the reddest object. If this star is a cluster member, it would be responsible for $\sim$ 60% of the total cluster light and will affect significantly the integrated spectral properties of the cluster, thus it is very important to carefully analyse its cluster membership. According to the velocity distribution of the bright stars around NGC 2162, shown on Figure 4.13, middle panel, this star has a velocity very similar to the velocity, which we measured from the central cluster mosaic. This, however, may still be due to projection effects, since the LMC field contains also carbon stars, which have similar properties as the ones belonging to clusters (Frogel et al. 1990). Looking at the surface distribution maps of C- and M-type giants across the LMC field in the study of Blanco & McCarthy (1983), we see that NGC 2162 is located in a region far away from the LMC bar, which has the highest frequency of field carbon stars. According to these maps, we can expect to have ~ 25 C-type stars in an area of 1 deg^{-2}. This density, scaled to the area, covered by a circle with a radius of 90″, gives 0.05 carbon stars for the 1.96×10^{-3} deg^2. Moreover, the control field, that Mucciarelli et al. (2006) used to estimate the LMC field contribution (shown on their Figure 4), does not contain any stars on the AGB redder than $(J - K) = 1.2$. Having bright carbon stars is not untypical for LMC globular clusters with the age and

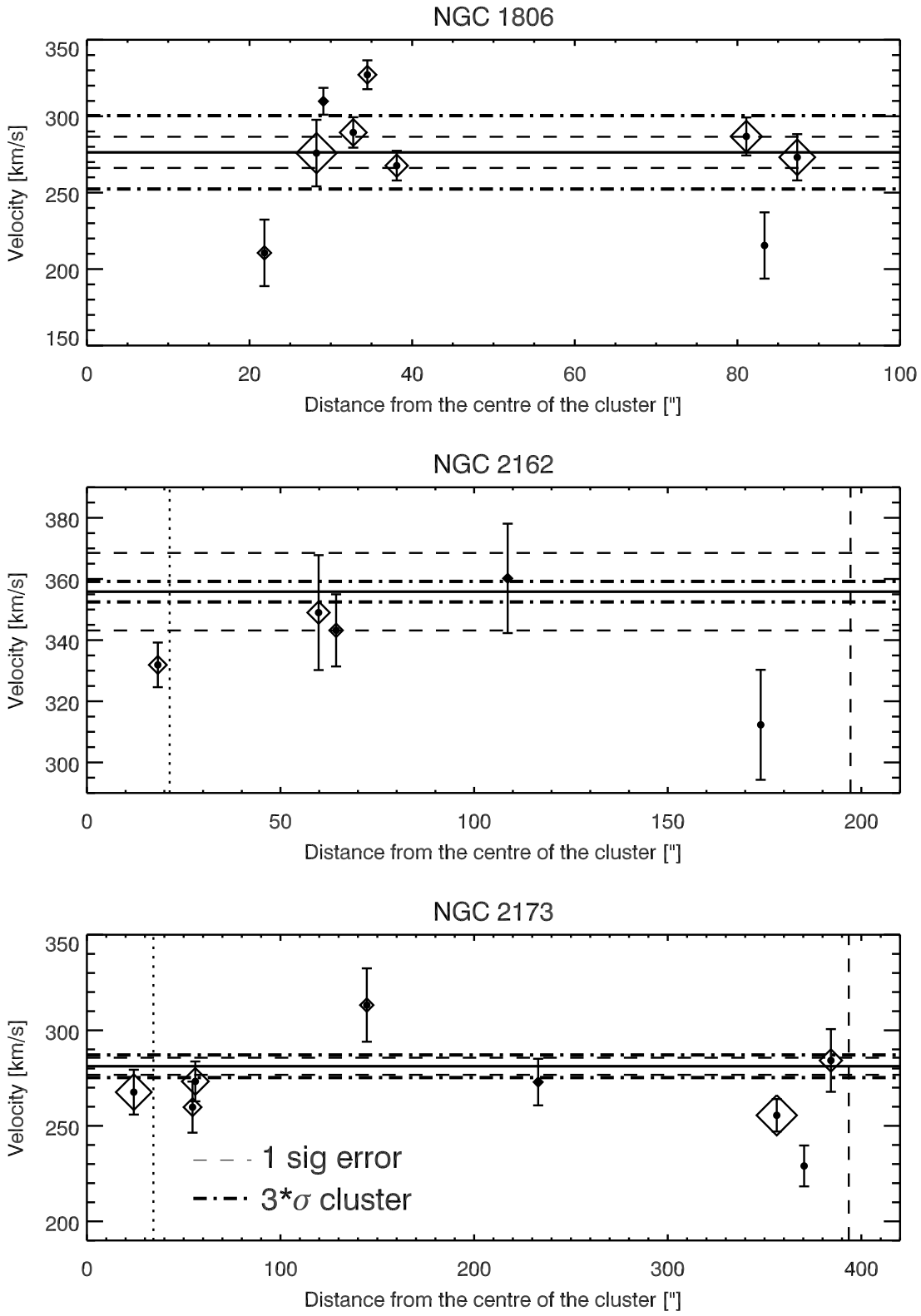

Figure 4.13: Radial velocities of the stars observed in the vicinity of the group of the intermediate age clusters, NGC 1806, NGC 2162, and NGC 2173, as a function of their distance from the clusters' centres. The used symbols are identical to the ones in Figure 4.11.

metallicity of NGC 2162, which SWB type is V, as shown by Frogel et al. (1990). With all these facts taken together, we can assume that this very bright and red star is a cluster member, although its definite membership will be confirmed or rejected only by high resolution spectroscopy. In order to obtain the final integrated spectrum of NGC 2162, we have also added the other two bright stars, located within 90″ radius. The remaining stars in our observational sample have too low S/N and would not increase the total S/N.

NGC 2173: The decisions about cluster memberships of the stars observed around this cluster are easier. This is due to the availability of high resolution spectroscopy of RGB stars in NGC 2173 from the study of Mucciarelli et al. (2008). As shown on Figure 4.14, we have three stars sitting outside of the central SINFONI mosaic and one within it in common with their study. Based on high resolution spectra Mucciarelli et al. (2008) find that these four stars have very similar radial velocities (rms = 1.2 km s^{-1}) and negligible star-to-star scatter in the [Z/H]. Thus we safely conclude that at least the first three stars outside of the SINFONI mosaic are cluster members and include them in the final integrated spectrum for the cluster.

4.3.7 Discussion on cluster light sampling

In the previous section we have shown that with a reasonable amount of offsets and within 1.5 hours observing time, we can sample a good fraction of the light from our sample of LMC GCs. We have seen that for well concentrated clusters there is no need for additional light sampling, than a central mosaic, covering at least the half-light radius. The strategy of observing a mosaic on the cluster's centre and then a sequence of the brightest and closest stars within a certain radius, works very well in the case of sparse and not luminous clusters, as well as for those, which are rich, but not well concentrated. However, there are still some doubts about the cluster membership of the brightest stars around the intermediate age clusters, especially in the case of carbon rich stars. For this reason we would need high resolution spectroscopy to measure their radial velocities and compare with other RGB stars.

Flux calibration of ground based spectroscopic data in the near-IR is particularly difficult, thus we cannot rely on direct luminosity estimates from our data. However, we can use the available photometry of Mucciarelli et al. (2006) to estimate the approximate amount of sampled light in the intermediate age clusters. In this study the authors provide not only integrated magnitudes and colours, but also estimates of the M- and C-type stars contributions to the total cluster light in the *K*-band. From there we know that the *K*-band light of NGC 2162 is dominated by only one carbon rich star, which is responsible for ∼ 60 % of the total cluster's luminosity. This C-type star contributes with about 70 % to our final integrated cluster spectrum. From this we conclude that for this cluster we are missing approximately 10 % of the luminosity, measured by Mucciarelli et al. (2006). But we have to note that their study goes as faint as $K = 18^m$, while the majority of our stars are not fainter than $K = 14^m$ (see Figure 4.2). The situation with the other two intermediate age clusters is similar. NGC 1806 is quite rich in stars in comparison with the other two clusters, as seen in the *K*-band images on Figure 4.4. According to Mucciarelli et al. (2006) 22 % of the total cluster light is

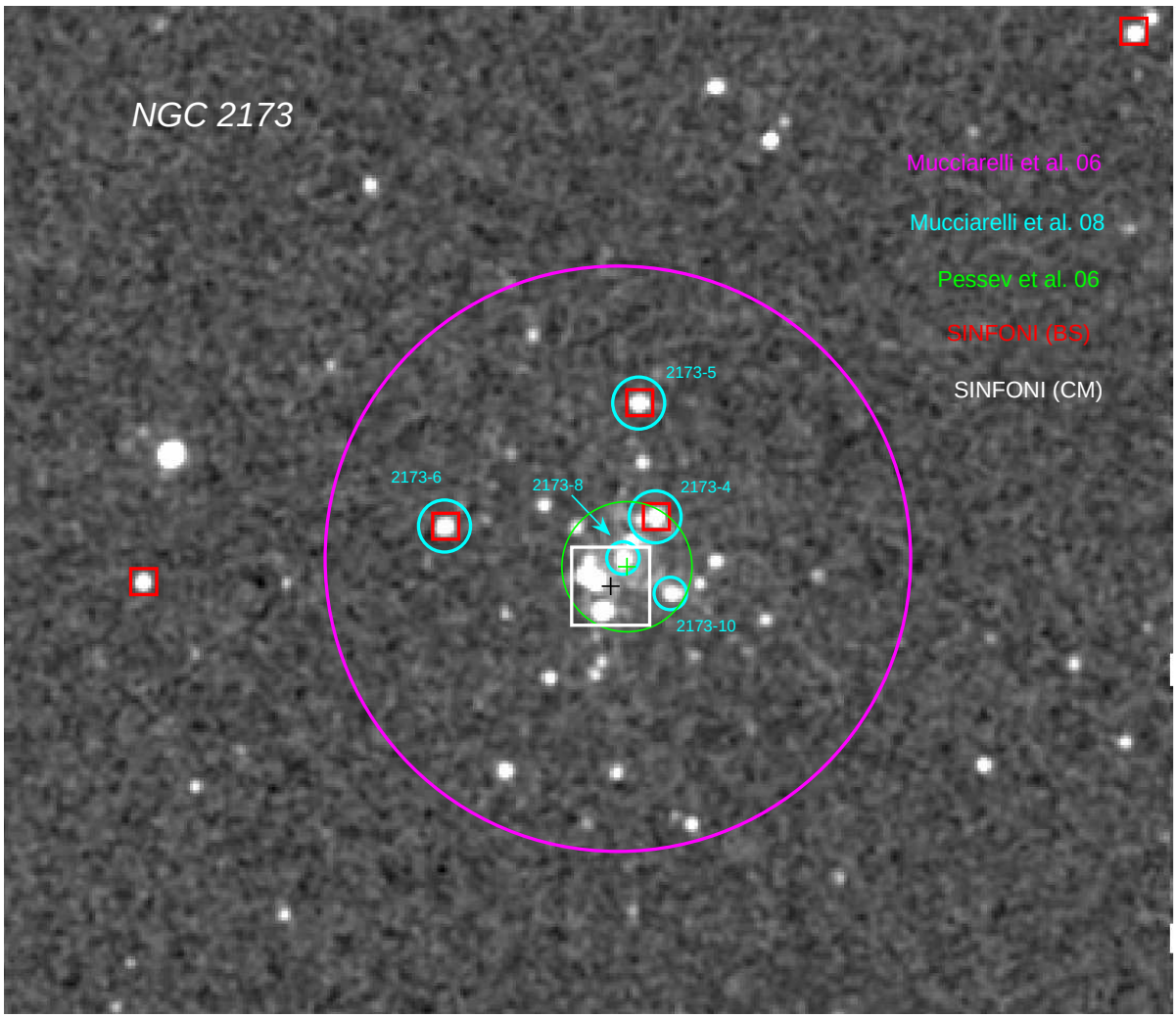

Figure 4.14: A summary of the available photometric and spectroscopic data about NGC 2173. The white square marks the extent of the SINFONI mosaic. The red squares show the additional bright stars we have observed with SINFONI. The cyan circles show the stars with high resolution spectroscopy data from Mucciarelli et al. (2008) (with numbers assigned as in this paper). The green circle shows the aperture with 20″ radius that Pessev et al. (2006) used for photometry. Finally, the magenta circle denotes the photometric aperture of Mucciarelli et al. (2006) with 90″ radius.

coming from stars with $K < 12.3^m$ (AGB stars). About 77 % of it is due to four carbon stars. In our NGC 1806 integrated spectrum these four C-type stars account for ∼ 60 %. Following Mucciarelli et al. (2006), 15 % of the light in NGC 2173 are due to a C-type star. In our spectra this star is responsible for ∼ 20 %.

According to these rough estimates it is evident that we have reached our goal, set up in Section 4.1, namely to obtain representative luminosity weighted, integrated spectra in the *K*-band for a group of clusters, having intermediate and old ages. The final spectra, used for the scientific analysis in the following sections, are shown on Figure 4.16.

4.4 Comparisons with stellar population models

One of the goals of the project, discussed in this chapter, is to provide spectra of globular clusters, which will be used to verify the predictions of current SSP models in the near-IR *K*-band and will serve as an empirical framework for the analysis of galaxy spectra. Our sample consists of six globular clusters in the LMC. Three of them, NGC 1754, NGC 2005 and NGC 2019, are members of the first generation of globulars being born in this galaxy. Their ages are above ∼ 10 Gyr and the metallicity is [Z/H] ∼ −1.4. The second group, consisting of NGC 1806, NGC 2162 and NGC 2173, is representative for the intermediate age population of GCs in the LMC. They have been formed during the secondary star formation event in the galaxy, which took place about 2 – 3 Gyr ago. Also their metallicity is higher, [Z/H] ∼ −0.4. These two groups will be used to explore two different regimes of stellar populations, old and metal poor, and intermediate age and more metal rich.

4.4.1 Old clusters

Literature data of the integrated near-IR colours of our sample of old and metal poor clusters are shown in Figure 4.17 with open circles. The large open symbols represent the colours, derived from 100″ radius aperture photometry, the small open symbols from 20″ radius aperture photometry from Pessev et al. (2006). With blue lines we have overplotted SSP model predictions from Maraston (2005) for Kroupa IMF and blue horizontal branch morphology. The metallicity which is closest to the one, derived for our GCs sample is denoted with a solid blue line, [Z/H] = -1.35. In the top panel the data agree reasonably well with the model $(J - K)$ colour. In the bottom panel the $(H - K)$ colours show a larger spread.

Besides comparing colours we can also compare our data with SSP model predictions of spectral indices. Maraston (2005) provides a full set of SEDs (spectral energy distributions) for different stellar populations with ages from 10^3 yr to 15 Gyr and covering a range of metallicities (1/20, 1/2, 1 and 2 times solar metallicity). These SEDs extend up to 2.5 μm, but their spectral resolution in the near-IR wavelengths is rather low, with one pixel covering 100 Å. Maraston (2005) shows the behaviour of a CO index, which measures the ratio of the flux densities at 2.37 and 2.22 μm, based on the HST/NICMOS filters F237M and F222M. The index is computed in units of magni-

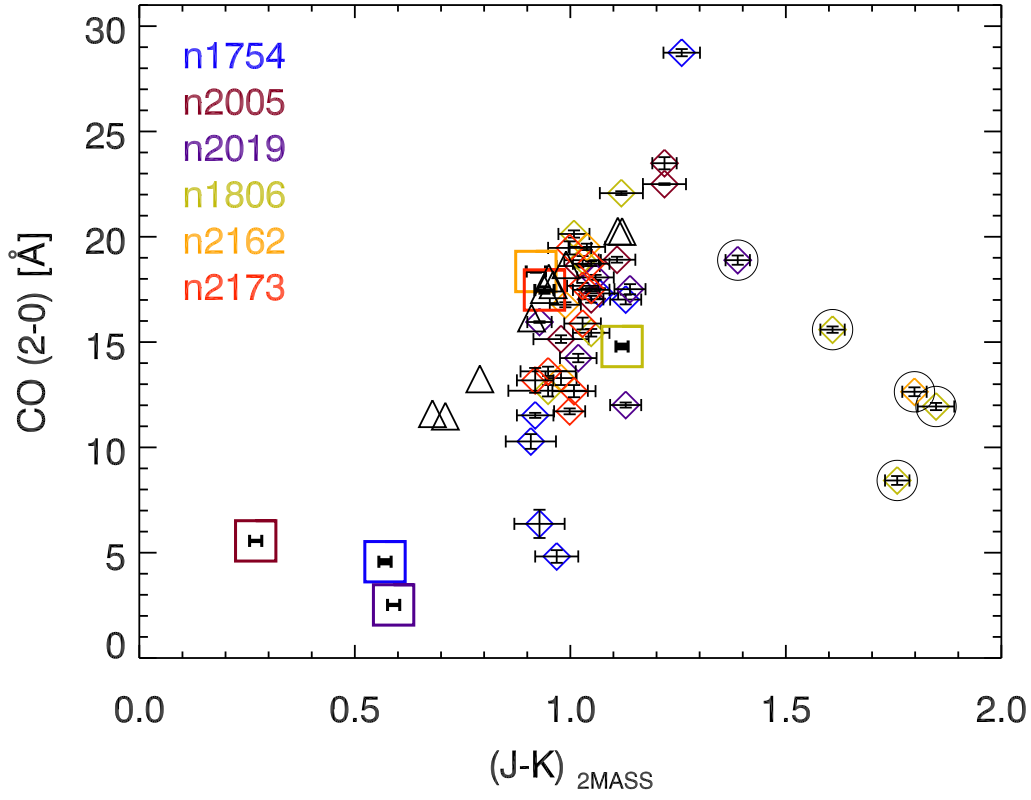

Figure 4.15: $(J - K_s)$ vs ^{12}CO (2–0) line strength in our sample. The squares mark our GCs, the diamonds show the additional bright stars in our sample. The ones, identified as carbon-rich, are surrounded by circles. The triangle symbols represent the galactic open clusters stars from Silva et al. (2008).

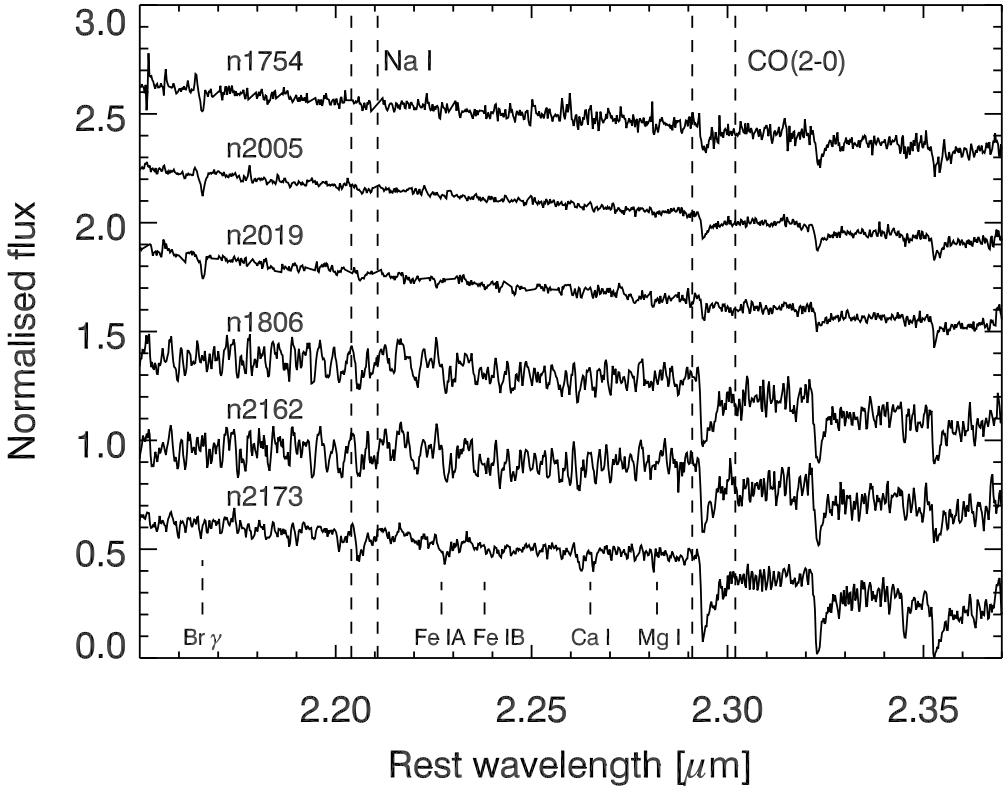

Figure 4.16: Final integrated spectra of the six LMC globular clusters, used for analysis. The spectra of NGC 1754, NGC 2005 and NGC 2019 contain light, integrated over the central SINFONI mosaics. The spectra of NGC 1806, NGC 2162, and NGC 2173 contain the light from the central mosaics plus additional bright stars.

tudes and is normalised to Vega. This index spans a much larger wavelength range and covers a number of the CO band-heads, as compared to the other two indices, introduced in Chapter 3, which measure the strength of ^{12}CO (2–0) only.

For the top panel of Figure 4.18 we used the CO index defined in Maraston (2005), while for the bottom panel we used the D_{CO} index defined in Mármol-Queraltó et al. (2008, see Chapter 3). We computed this index from the model SEDs, provided on C. Maraston's web page, for a Kroupa IMF. In order to measure the D_{CO} index we had to interpolate the theoretical SEDs linearly to a smaller wavelength step of 14 Å. We have chosen this value after a few tests to check the stability of the computation. Mármol-Queraltó et al. (2008) show that their D_{CO} index definition is very little dependant on the instrumental or internal velocity broadening of the spectrum. However, the most extreme resolution they have tested is $\sim$70 Å ($FWHM$), while the resolution of the model SEDs is more than 200 Å ($FWHM$). We have measured the D_{CO} index in 10 stars from our sample with their nominal resolution and when broadened to match the resolution of the models. The broadened spectra show offsets in D_{CO} index value of up to -0.03. An offset with this size is not going to influence our general conclusions about the integrated spectra of LMC GCs. This is further supported by the CO index values of the GCs, which exhibits the same relative values, as compared to the models. The CO index covers a very large wavelength range and is little dependant on the spectral resolution. Thus we decided to measure the D_{CO} index at the nominal resolution of the spectra and treat the models with caution. Once higher resolution models become available, this comparison should be repeated in a more quantitative way.

For stellar populations with an age of more than 3 Gyr the near-IR K-band light is dominated by RGB stars. The fuel spent in this evolutionary phase stays approximately constant (Maraston 1998, 2005). This is reflected in the stellar population models in Figure 4.18, where the CO index remains almost constant at a given metallicity for ages $\geq$ 3 Gyr. Our observational data fit reasonably well with the model predictions, despite the slightly lower index values in the LMC GCs, compared to the [Z/H] = −1.35 line.

4.4.2 The influence of carbon stars on intermediate age clusters

We can divide the intermediate age sample of our GCs into two sub-samples, according to the SWB type of the clusters. NGC 1806 and NGC 2162 have SWB type V and thus their age is estimated to be around 1.1 Gyr (Frogel et al. 1990). NGC 2173 has SWB V.V and an age of approximately 2 Gyr (Frogel et al. 1990). Based on colour-magnitude diagram methods different authors give slightly higher or lower ages for these clusters in comparison with the above values. In order to be consistent with the age calibration of the SSP models presented by Maraston (2005) we have decided to use the ages based on SWB types.

In Figure 4.17 literature data for the intermediate age GCs in our sample are also shown. According to their mean metallicity we should compare them with the dotted lines, which show the model predictions for [Z/H] = −0.33. The data are coming from two recent studies of the integrated photometric properties of GCs in the LMC. The first one is made by Mucciarelli et al. (2006) with the ESO 3.5 m NTT/SOFI. On the plots their results are shown with solid circles. They list the integrated near-IR magni-

tudes within an aperture with radius of 90″, after decontamination from the LMC field population, extinction and completeness corrections. In the second study Pessev et al. (2006) use near-IR images from the 2MASS Extended Source Catalogue and perform photometry with different aperture sizes (the open circles on the plots) after correcting for the extinction and LMC field population. Comparing the large filled and open symbols on Figure 4.17, we see some degree of disagreement between the two studies, despite that Mucciarelli et al. (2006) do not provide error bars. We also see that according to the different apertures of Pessev et al. (2006) our intermediate age clusters exhibit colour gradients of about 0.2^m in $(J-K)$ and $(H-K)$, however not always in the same direction. In $(J-K)$ the clusters become systematically bluer with increasing radius, while in $(H-K)$ NGC 2162 gets redder. In general colour gradients in globular clusters can be explained by mass segregation, which makes the most massive, and thus the most evolved, stars to fall towards the centre. However, this effect is not expected to be that large, in comparison with the values that Pessev et al. (2006) report. Also the majority of our intermediate age cluster sample are not very massive, thus we can expect that mass segregation has not been very effective in bringing the most massive stars in the centre of the cluster. We have already discussed in Section 4.3.6 that Pessev et al. (2006) seem to have overestimated the LMC field contribution, which gives a possible explanation for the observed colour gradients, being due to an inappropriate LMC field decontamination, during which the reddest stars have been removed.

Having made the comparison of the SSP model predictions with the observed colours of LMC globular cluster, we can continue to the spectral comparisons in Figure 4.18. For the intermediate age clusters on both panels the closest model metallicity to the data is denoted with the dotted line, [Z/H]= −0.33. NGC 2173, marked with a red filled circle and having an age of approximately 2.2 Gyr, agrees reasonably well with the model predictions. However, the other two intermediate age clusters, NGC 1806 (light green filled circle) and NGC 2162 (orange filled circle) have CO index values much lower than the model predictions, independent from the index definition. Our data show the same behaviour when using the ^{12}CO (2–0) index definition from Frogel et al. (2001). We do not show a similar comparative plot here, since this index definition is significantly sensitive to spectral resolution and proper resolutions corrections need to be applied to the model SEDs.

We have tested a few scenarios, which can provide possible explanations of the observed trends. The first scenario, which we have investigated is that we are not sampling well the total cluster light. This hypothesis can be ruled out following the estimations about the sampled cluster light during our observations, made in Section 4.3.7. There we have concluded that our observations sample up to 80 % of the total cluster light. Thus this is not a potential reason for the disagreements with the models.

By carefully investigating the integrated LMC intermediate age GCs spectra, we have seen that the presence of C-type stars does not only influence the overall colours of the clusters, as discussed above, but also the CO index. Looking at the individual stars in Figure 4.15, we see a general trend of increasing ^{12}CO (2–0) index with the colour becoming redder. This is typical for oxygen rich (or M-type) stars (e.g. Frogel et al. 1990). However, stars with $(J-K) > 1.3$ show a decreasing ^{12}CO (2–0)

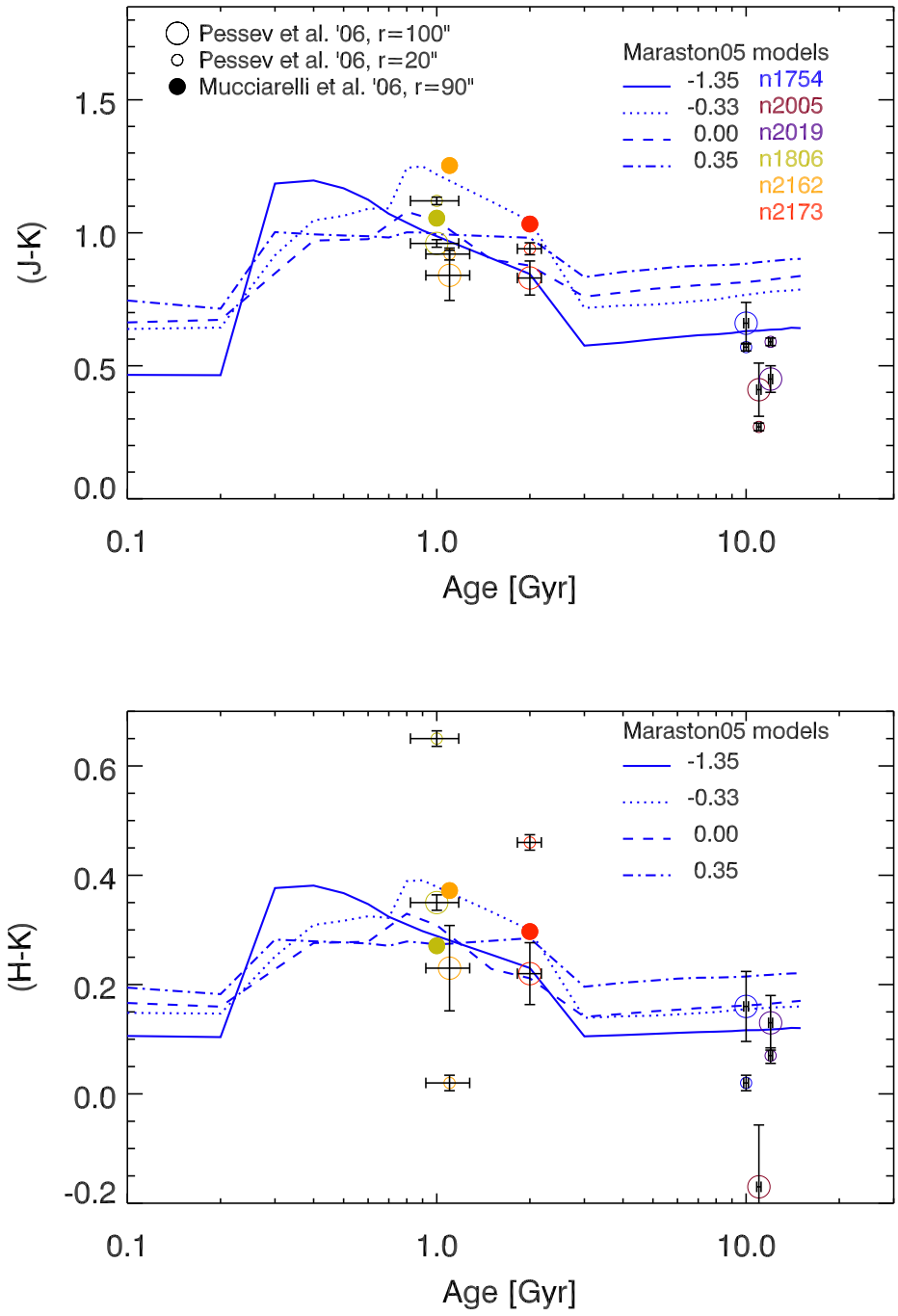

Figure 4.17: Comparison of clusters' integrated colours with SSP model predictions from Maraston (2005). The filled coloured circles (colour coding as listed in the upper right corner of the top plot) correspond to the $(J-K)$ and $(H-K)$ colours derived form the 90″ radius aperture photometry of Mucciarelli et al. (2006). The coloured open circles give the values, which Pessev et al. (2006) derived from two different size apertures: small circles for $r = 20''$, large circles for $r = 100''$. The blue thick lines with different styles give the model predictions as a function of the metallicity and the age.

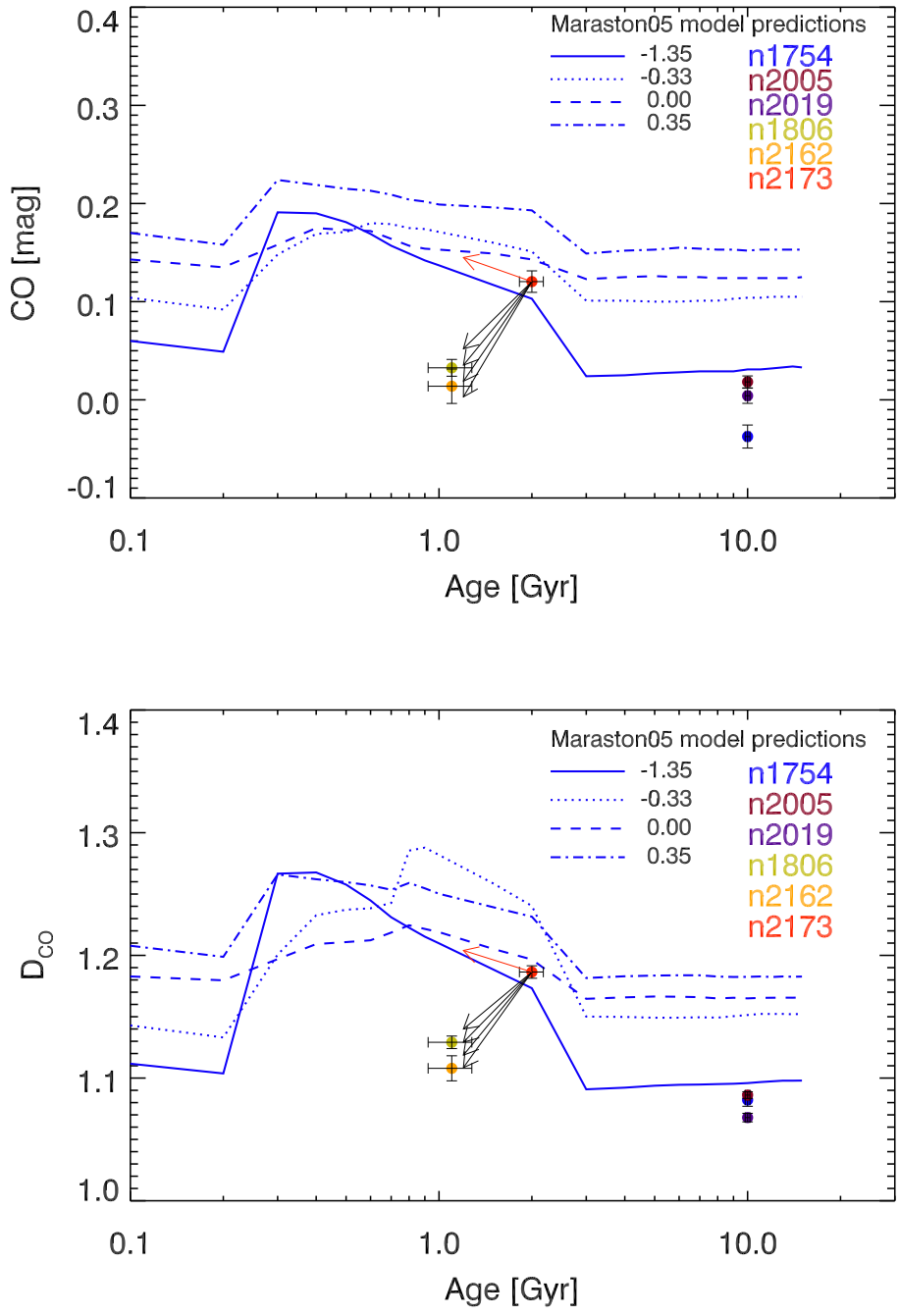

Figure 4.18: A comparison of model predictions of Maraston (2005) with our LMC GCs data (coloured filled circles). Model metallicities are given with different line styles *Top panel:* CO index, used by Maraston (2005) to compute CO line strength. *Bottom panel:* D_{CO}, defined by Mármol-Queraltó et al. (2008). On both plots the arrows show the changes in CO after adding a different amount of carbon star contribution to the NGC 2173 spectrum. From top to bottom the carbon star fraction is 40 %, 50 %, 60 % and 70 % respectively. The red arrow shows the CO index when the spectrum of NGC 2173 is composed of 60 % of the spectrum in the 3^{rd} bin of Lançon & Mouhcine (2002).

line strength. These are exactly the carbon rich stars, separated on Figure 4.5 with a slanted line, and denoted on Figure 4.15 with circles. Similar trends for LMC globular clusters' carbon stars have been observed by Frogel et al. (1990) as well.

According to Frogel et al. (1990) the clusters, which harbour the brightest carbon stars are of SWB type V – VI. For these clusters carbon stars contribute about 40 % of the total bolometric light. Exactly this observational fact is taken into count in the models of Maraston (2005) for the calibrations of the modelled SEDs. We have used the spectrum of NGC 2173 to check what is the effect of different ratios of M-type to C-type stars on the CO line strength. This spectrum is very convenient for this kind of tests, since it is the one with a minimal carbon star contribution, only 15 % according to Mucciarelli et al. (2006), in our sample. We have modelled different C:M ratios in the final spectrum by adding the corresponding amount of carbon star light. The results are shown in Figure 4.18 with arrows, starting from the initial position of NGC 2173 (red filled circle) on the age – index diagram and ending at the age of clusters with SWB type V, i.e. 1.1 Gyr. The reason for this age scaling is that a larger carbon star contribution would mimic the spectrum of a younger cluster. The arrows show, from top to bottom, an increasing fraction of carbon star contribution to the final cluster light – 40 %, 50 %, 60 % and 70 %, respectively originate from the C-type star. The same is valid for both, the CO index used by Maraston (2005) and the D_{CO} index defined by Mármol-Queraltó et al. (2008). The outcome of this simple stellar population modelling is that the observed values of different CO indices for LMC clusters with SWB type V can be reproduced with an increasing fraction of the carbon star contribution. It is interesting to note that the same kind of tests, but performed with integrated colours, do not give such large changes in the $(J - K)$ colour, as in the CO index values.

The big advantage of the models of Maraston (2005) is the inclusion of TP-AGB phase in the final SEDs, which is of paramount importance for stellar populations with ages between 0.3 and 2 Gyr, due to the very high luminosity of this stellar phase. The empirical photometric calibration has been done with the near-IR photometric data of LMC globular clusters and AGB stars of Persson et al. (1983) and Frogel et al. (1990). The spectral calibration of carbon stars, included in the models, has been performed using the averaged C-type star spectra, published by Lançon & Mouhcine (2002). These authors have obtained 21 spectra of carbon-rich LPVs in the Milky Way. However, due to the small temperature scales of the sample, they do not consider as justified to have more than a few averaged bins. The carbon stars have been grouped according to their temperature, defined by their $(H - K)$ colour. The first three bins contain averages of 6 C-type star spectra each. Bins 4 and 5 contain the spectra of a single very red star, R Lep, near maximum and minimum light. The temperature of the stars is decreasing with increasing bin number.

If carbon rich stars in the Galaxy and the LMC have different CO absorption strengths, then it would have a profound implication on the model predictions. Differences in the CO index are suggested by Frogel et al. (1990), where they compare the CO value of LMC clusters C-type stars and their counterparts in the Milky Way. The LMC stars have systematically weaker values at a given colour. In Figure 4.19 we show a comparison of the CO index values as a function of $(J - K)$ colour, measured in C-type stars belonging to our sample and the CO index, that we measured on the averaged spectra

of Lançon & Mouhcine (2002). LMC stars are marked with filled symbols. The least-squares linear fit to these data points is shown with a solid line. The fit coefficients for the D_{CO} index are:

$$D_{CO} = 1.668 \pm 0.103 - 0.321 \pm 0.058\,(J-K) \tag{4.2}$$

The Milky Way averaged spectra are marked with open symbols, with a bin number written next to each. The dashed line is showing the linear least-squares fit to the averaged spectra, for the D_{CO} index having fit coefficients:

$$D_{CO} = 1.268 \pm 0.007 - 0.042 \pm 0.003\,(J-K) \tag{4.3}$$

From this figure we see that the trends for C-type stars in these two galaxies generally disagree. Moreover, stars with $(J-K) > 1.6$ have increasingly different CO index values, which explains why our LMC GCs sample fits the model predictions for integrated colours, but not for the CO index.

We have made another test of including carbon star light to the spectrum of NGC 2173, but this time using the spectrum of bin 3 of Lançon & Mouhcine (2002). The result is shown in Figure 4.18 with red arrows. For this case specifically the ratio of carbon star to the original spectrum was 6:4. Different ratios, as in the previous test, give similar values. We see that the overall CO index value increases by adding Milky Way carbon stars, while the inclusion of LMC cluster carbon stars leads to a decrease in the index. This can be a potential explanation of the discrepancies between the models and the data, because the models have been calibrated with stars from the Milky Way.

At this point the question arises why C-type stars in the LMC and the Galaxy have different CO line strengths at a given near-IR colour? We have to treat this issue with care, since not all of the carbon stars in the Lançon & Mouhcine (2002) library disagree with the relation for the LMC C-stars. The averaged spectrum from bin 2 has CO indices very close to the LMC values. In Figure 4.19, bottom panel, we have added another C-type star from the Milky Way, marked with an asterisk. It is located in the Galactic open cluster NGC 2477, whose metallicity is [Z/H]= −0.02 (Houdashelt et al. 1992). A K-band spectrum of it has been published in Silva et al. (2008), however the authors did not discuss its properties. Its $(J-K)$ colour is 1.69 (Houdashelt et al. 1992) and the D_{CO} index value is consistent with the relation for LMC C-type stars, given in Equation 4.2.

The first suggestion for the reason for the different CO index values in LMC and Milky Way carbon stars is due to the metallicity of the two samples. As already discussed earlier, AGB stars with lower metallicity are more likely to become C-type. The star becomes C-type when C/O>1. This can happen only when all the O is locked up in CO, and there is still some extra C in the atmosphere. For the metal-poor stars there is less O in the atmosphere in the first place. Therefore the star needs to dredge up less C in order to overcome in relative amount the quantity of O and so become C-type. The remaining carbon is used to form other molecules, like C_2, CN and CH. In this way the CO index as we measure it decreases. Note that the overall line strength of the ^{12}CO (2–0) may not decrease significantly, for example see Figure 4.16, where the ^{12}CO (2–0) feature in NGC 1806 and NGC 2162 does not seem to be much weaker, as

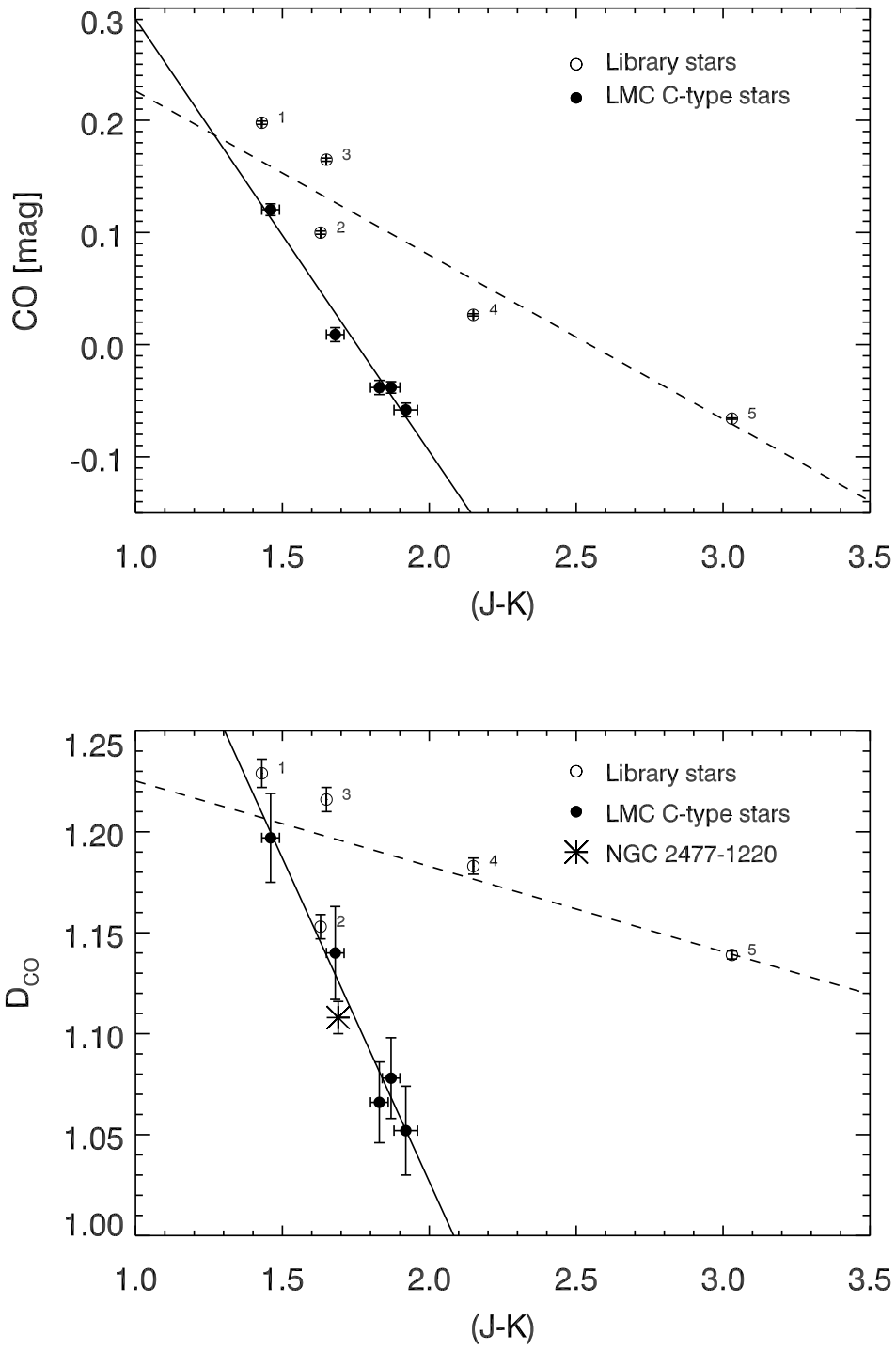

Figure 4.19: $(J - K)$ vs. CO index in LMC and Milky Way carbon-rich stars. LMC stars are marked with filled circles. The linear least-squares fit to the data is shown with a solid line. The values for the Milky Way averaged star spectra from Lançon & Mouhcine (2002) are shown with open circles. The number next to each data point corresponds to the bin number. Their linear least-squares fit is shown with a dashed line.

compared to NGC 2173. But the CO indices, which we use to describe the behaviour of this feature, take into account the continuum shape as well, which in the case of carbon stars is severely affected by the presence of features like C_2, CN or CH.

In more metal rich stars the amount of oxygen atoms is higher and all of the available carbon is used to form CO molecules, which makes stronger CO index. The stars from the Lançon & Mouhcine (2002) library are Milky Way stars and thus have solar metallicity, which is higher than the average metallicity of the LMC of $[Z/H] \sim -0.5$ (see e.g. Carrera et al. 2008). This could explain why CO indices are higher in Milky Way C-type stars. However, we have already shown that there are Milky Way C-type stars, which have lower CO indices. Another possible explanation of the differences in CO line strength is the age of the stars, but exploring this dependence is not trivial.

The observed difference between the carbon stars in the Milky Way and in the LMC has important implications on the stellar populations models. The photometric calibration of the intermediate age populations in the models of Maraston (2005) has been performed with globular clusters in the LMC. However, for model SED synthesis spectra of carbon stars from the Milky Way have been used. Here we show that the contribution of carbon stars with solar solar metallicity to sub-solar model tracks produces inconsistent results. Clearly, a better empirical calibration of the models is necessary, and a new library of carbon stars with sub-solar metallicities needs to be included in the models. However, this choice might give a good estimate for the spectral properties of populations with metallicities above solar, if Milky Way carbon stars really have higher CO indices. We are going to test the models in super-solar metallicity regime in Chapter 5, using long-slit spectra of early-type galaxies.

4.5 Near-IR index diagnostic diagrams

In Figure 4.20, top panel, we show a diagnostic diagram, based on two near-IR indices: Na I and D_{CO}. The positions of the data points resemble remarkably well the distribution in Figure 4.18. On both plots the *y*-axis gives the strength of CO, while the *x*-axis gives the ages of the clusters in the former graph, and the strength of Na I in the later case. The near-IR Na I index seems to be well correlated with the age of the clusters, however, metallicity may also play a role. This result was already suggested by Silva et al. (2008). They find that centres of early-type galaxies in the Fornax cluster with signatures of a younger population, i.e. stronger Hβ, have stronger Na I indices, than purely old galaxies. The bottom panel in Figure 4.20 shows that the Ca I line strength correlates with the D_{CO} index. However, this correlation has to be taken with caution since the clusters in the data sample have different metallicities.

In Figure 4.21 we show the Na I index (top panel) and Ca I index (bottom panel) as a function of the age of the clusters. For intermediate age clusters the Na I index increases with decreasing age. The Ca I index exhibits the same behaviour as the D_{CO} index.

The combination of near-IR spectral features with optical ones may lead to a better understanding of the current age-metallicity degeneracies. For this reason we searched in the literature for optical integrated light spectroscopic studies, which can help us to

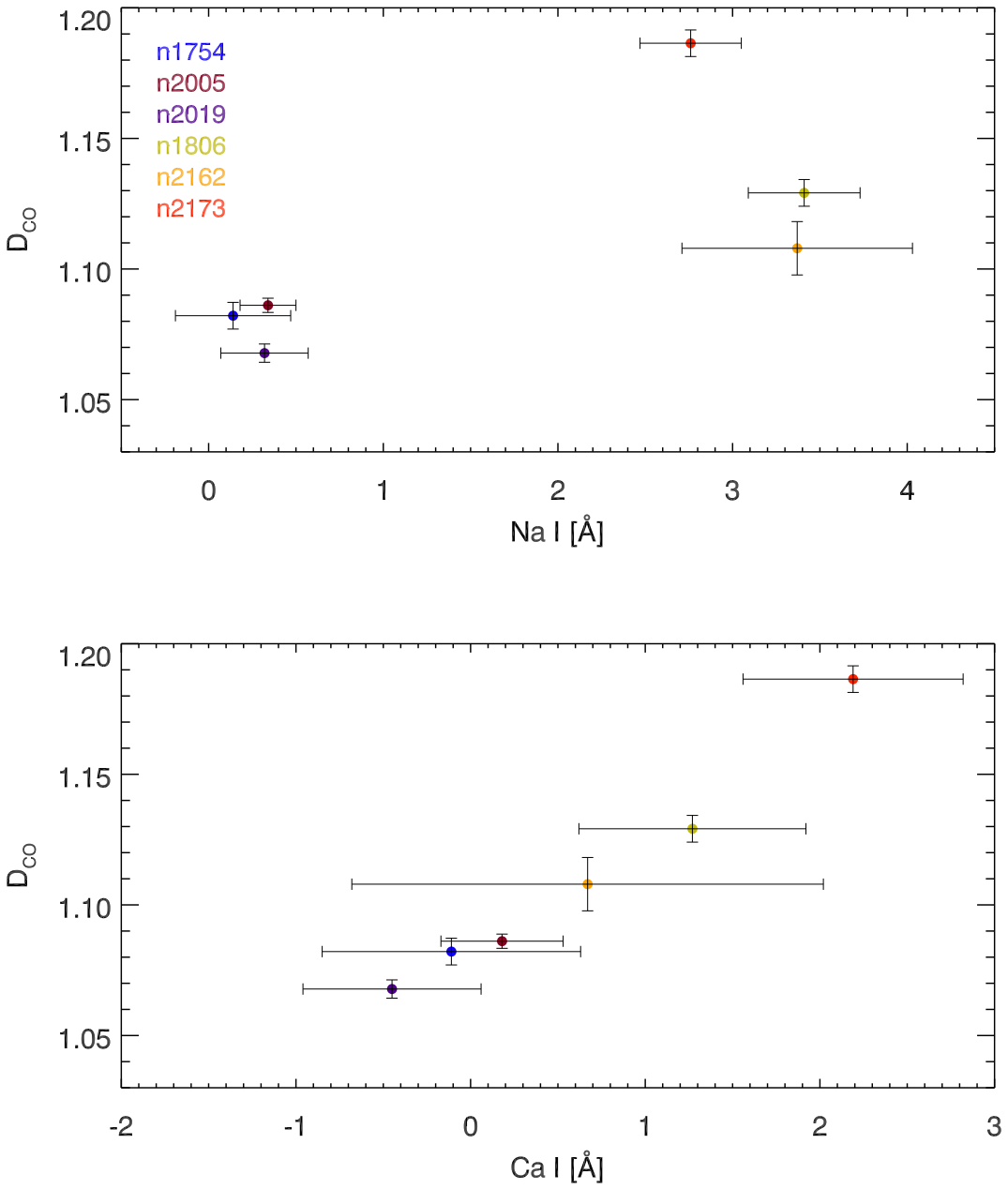

Figure 4.20: Near-IR diagnostic diagrams. *Top panel*: D_{CO} index vs. Na I, measured from the integrated luminosity weighted spectra of LMC GCs. *Bottom panel*: D_{CO} index vs. Ca I.

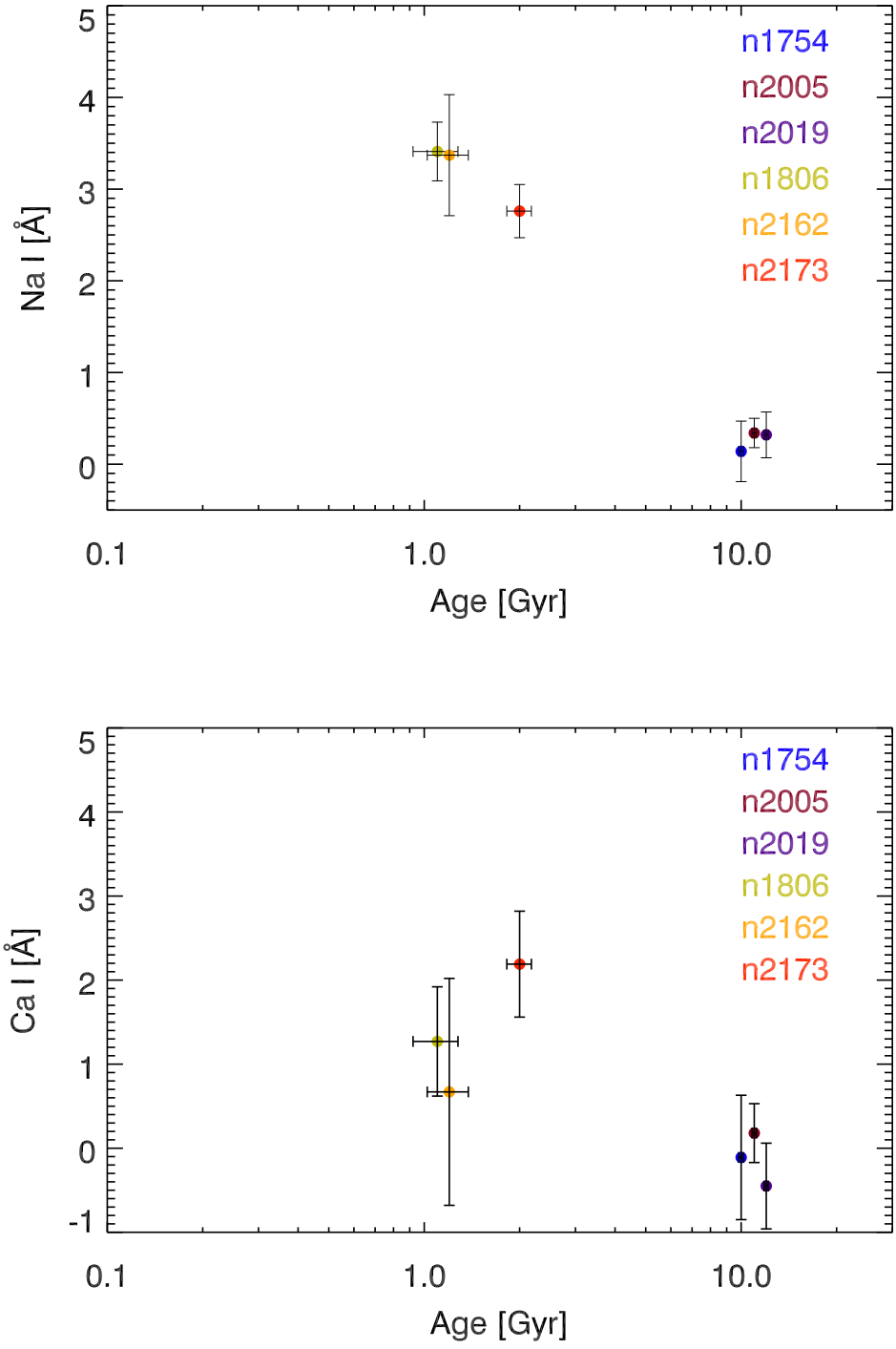

Figure 4.21: Near-IR indices plotted vs. the age of the clusters. *Top panel*: Na I, *Bottom panel*: Ca I index.

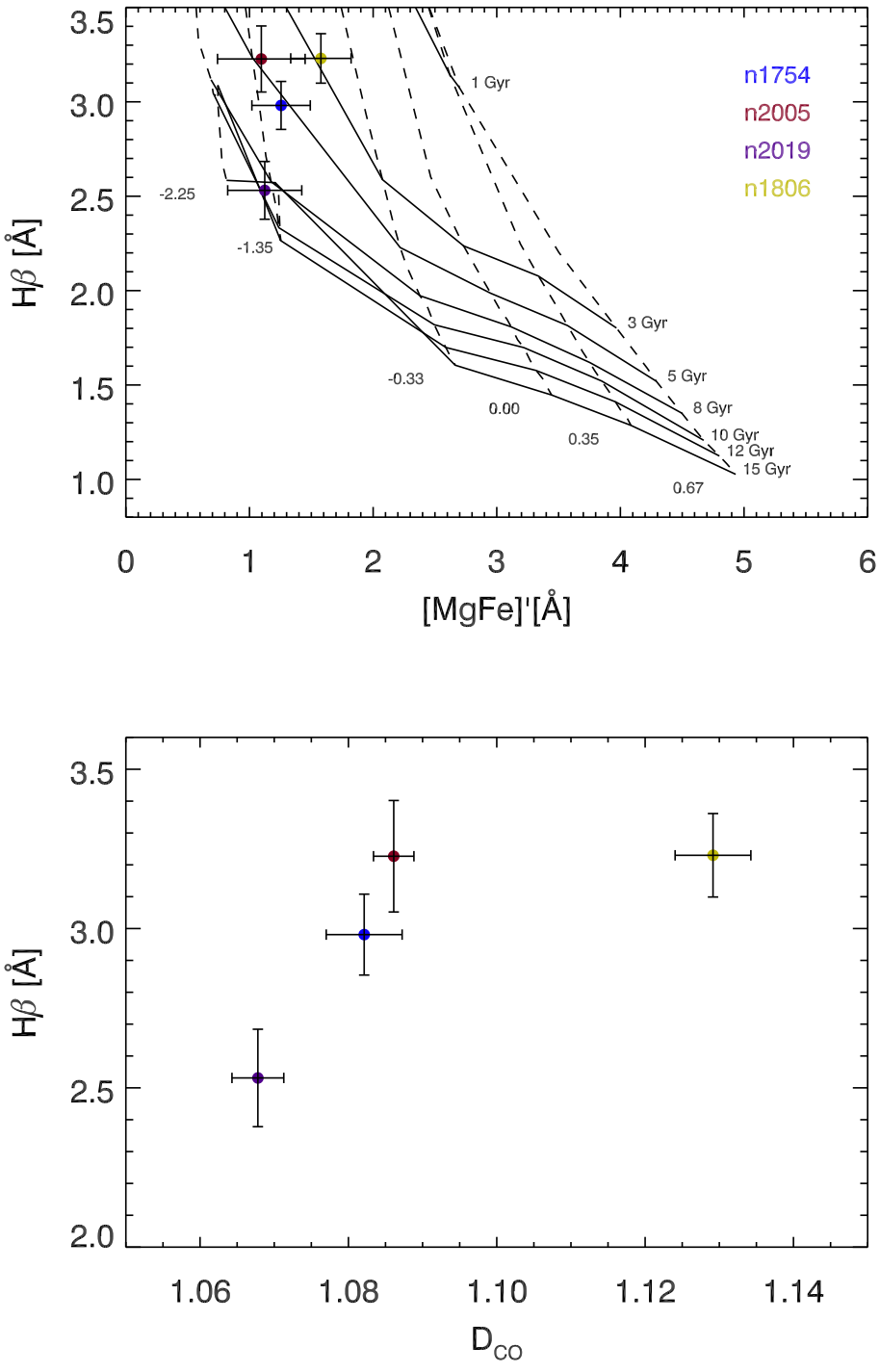

Figure 4.22: Comparison of optical with near-IR spectral properties. *Top panel*: Hβ vs. [MgFe]' age-metallicity diagnostic diagram. Filled coloured circles represent the LMC clusters NGC 1754 (blue), NGC 2005 (dark red), NGC 2019 (violet) and NGC 1806 (green) (data from Beasley et al. 2002). Overplotted are SSP models from Thomas et al. (2003). Solid and dashed lines show lines of constant age and metallicity, respectively. *Bottom panel*: The optical index Hβ vs. the near-IR index D_{CO}.

make comparisons. Beasley et al. (2002) present Lick index values for a number of GCs in the LMC. We have four clusters in common with their sample: the old and metal poor NGC 1754, NGC 2005 and NGC 2019, and the younger and more metal rich NGC 1806. The spatial coverage of the optical spectra is only 3″ in diameter, which is much less than our SINFONI coverage of 24″×24″. However, this may not be a major issue, since the group of old clusters are reported to have undergone a core collapse (Mackey & Gilmore 2003), which means that their light is well concentrated towards the centres.

There are several SSP models in the optical wavelength range. With their help we can estimate luminosity weighted ages and metallicities of unresolved stellar populations, however some degeneracies still persist. In Figure 4.22, top panel, we show the SSP models by Thomas et al. (2003) for solar abundance ratios. The solid and dashed lines represent lines with constant age or metallicity, respectively. On top we have overplotted the Lick indices, measured by Beasley et al. (2002) for the four clusters in common with our work. According to this plot NGC 2019 and NGC 1806 have consistent ages and metallicities with what was estimated using other methods, i.e. colour-magnitude diagram fitting. However, NGC 1754 and NGC 2005 seem to have much younger luminosity weighted ages, as compared with colour-magnitude fitting age estimates. Beasley et al. (2002) suggest that this is due to differences in the horizontal branch (HB) morphology. Indeed, Olsen et al. (1998) show that NGC 1754 and NGC 2005 have a blue horizontal branch morphology. Their $(B-R)/(B+V+R)$ parameters (see Lee et al. 1994, B denotes the number of blue HB stars, V – the number of RR Lirae variable stars, and R – the number of red HB stars), which ranges between -1 for clusters with only red HB and +1 for clusters with only blue HB, are 0.47 and 0.87, respectively. However, the third old cluster in our sample, NGC 2019, also has a very blue HB ($(B-R)/(B+V+R) = 0.56$), but its age, as derived from optical indices, is still more than 10 Gyr. The origin of these discrepancies is still unresolved. In Figure 4.22, bottom panel, we show the dependence of Hβ vs. D_{CO}. The two clusters with strongest Hβ absorption have also stronger D_{CO}. This observation is still difficult to interpret and needs the more detailed predictions of future stellar populations models in the near-IR.

4.6 Conclusions

In this chapter we have presented the first results from a pilot study of the near-IR spectroscopic properties of a sample of six globular clusters in the LMC. To validate the observational strategy, data reduction and analysis methods, we have selected from the catalogue of Bica et al. (1999) three out of 38 GCs with SWB type VII to represent the old (> 10 Gyr) and metal poor ([Z/H]~ -1.4) population of the LMC, and three out of 71 clusters with SWB types V and VI to explore the properties of the intermediate age (1 – 3 Gyr) and more metal rich ([Z/H]~ -0.4) component of the population. For each cluster we have observed the central 24″ × 24″ and in most of the cases we have sampled about half the light. However, in order to better sample the RGB and AGB stars, which are the most important contributors to the integrated cluster light in the near-IR, we have observed up to 8 of the brightest stars outside the central mosaics,

but still within the tidal radii of the clusters, that have near-IR colours and magnitudes consistent with bright red giants in the observed clusters. We have obtained integrated luminosity weighted spectra for the six clusters, measured the line strengths of several absorption features in the *K*-band and compared them with current stellar population models. Our main results are as follows:

A successful observing strategy. The idea to cover at least the central half-light radius with a number of SINFONI pointings seems to be an efficient way in sampling the near-IR light of old (> 10 Gyr) clusters. For the intermediate age clusters, which are more sparse and dominated by just a few very bright stars, observing a central mosaic plus a number of the brightest stars in the vicinity of the cluster is a better choice for optimal cluster light sampling. The availability of high spectral resolution spectroscopy greatly helps the differentiation of the cluster member stars from the LMC field contamination.

The influence of carbon-rich stars on the integrated spectra of intermediate age clusters. In intermediate age clusters the largest amount of light originates from oxygen (M-type) and carbon-rich (C-type) AGB stars. Different ratios of the contributions by these two types of stars can lead to significant changes in the near-IR ^{12}CO (2–0) line strength. According to our observations at the time, when the C-type contribution peaks (at ~1 Gyr) the observed CO line strength is weak and then increases fast to reach its maximum for clusters with age ~2 Gyr.

Comparison with stellar population models: Implications due to carbon stars. The comparison of our data with the stellar population models of Maraston (2005), in terms of CO line strength, shows a disagreement for the youngest clusters in our sample. For clusters with age ~1 Gyr the models predict maximal CO line strength, while we observe the opposite: the CO strength is significantly weaker (see Figure 4.18). At the same time, literature data of the integrated colours of the clusters are consistent with these models (see Figure 4.17). We explain these discrepancies as due to the different origin of the C-type stars used to calibrate the models and the ones in our data sample. The stars, used for model calibration, are Milky Way carbon stars, which have roughly solar metallicity, while our carbon stars are born in the LMC, where the metallicity is lower. We support this hypothesis with Figure 4.19, where we show that carbon rich stars in the Milky Way and LMC, having similar $(J-K)$ colour, have very different CO line strengths.

Future work. To explore fully the spectral properties of globular clusters in the LMC we plan to extend our K-band light study, and include also the J- and H-bands, where other interesting spectral features reside. For example the C_2 at 1.77 μm promise to even better constrain the luminosity weighted ages and metallicities of intermediate age clusters (Maraston 2005). The LMC, with its rich evolutionary history and proximity, represents a unique laboratory for testing and calibrating present and future stellar population models. For this purpose the current sample of globular cluster has to be extended towards younger ages, where the carbon star contribution, which, as we have already shown, is extremely important, is even higher. Also clusters with an age above ~3 Gyr can potentially shed some light onto the current age-metallicity degeneracies, when near-IR data are combined with optical.

Chapter 5

Index scaling relations in the near-IR

5.1 Introduction

The observation that almost 75 % of all field elliptical galaxies exhibit morphological fine structures like shells and boxy isophotes (Bender et al. 1989), and about 60 % to 80 % of all elliptical galaxies have kinematically unsettled dust (van Dokkum & Franx 1995) suggests that a big fraction of the early-type galaxies in the field have undergone a star formation episode in the last 5 Gyr. These features can survive only for up to 3 Gyr before becoming mixed with the rest of the galaxy, which implies relatively recent mergers (e.g. Barnes 1992). Optical spectroscopy is currently our major tool of probing the stellar content of early-type galaxies. Using the Lick indices, in combination with stellar population models, significant progress has been made in unravelling the luminosity weighted properties of stellar systems, which remain unresolvable into single stars from the ground (e.g. Worthey et al. 1994; Kuntschner & Davies 1998; Trager et al. 2000; Sánchez-Blázquez et al. 2007). To derive ages the most often used feature has been the optical Hβ line. As metallicity indicators different combinations of lines of Mg and Fe are in use. However, still some degeneracies persist. Light from several important stellar evolutionary phases contributes almost equally to the spectral features in the optical wavelength range. For populations with ages between 1 and 3 Gyr this problem is less expressed, when observing in the near-IR. At that stage the near-IR light is dominated by TP-AGB stars. For populations with age of more than 3 Gyr, the main contributors are cool giant stars on the RGB (Maraston 2005). The relatively young age of the mergers implies that the new born stellar populations will be dominated by TP-AGB stars and their properties will be best observed in the near-IR wavelength range. Thus by carefully examining the near-IR spectral properties of early-type galaxies we can hope to gain a better understanding of the complex galaxy evolution processes.

We have undertaken a project aiming at constraining the central near-IR spectral properties of a sample of early-type galaxies in low density environments and compare them with literature data of galaxies in the Fornax cluster. We will also compare the galaxy data with present day stellar populations models and test the models in the super-solar metallicity regime, in contrast with our work, presented in Chapter 4, where we have tested the sub-solar metallicity range with the help of globular clusters

in the LMC.

The data sample consists of 26 elliptical and S0 galaxies in low density environments, also referred to as field galaxies. Some of them are members of local groups of galaxies and thus cannot be called real field galaxies. However, for the purpose of our study, they are still located in relatively less dense regions, as compared to the Fornax cluster of galaxies. For this reason we will refer to the galaxies in our sample as field early-type galaxies. Their global near-IR photometric properties have been presented in Silva & Bothun (1998a) and the central photometric properties in Silva & Bothun (1998b). In this chapter we present a follow up study using near-IR long-slit spectroscopy.

5.2 Instrument description and observations

As part of the project "A Near-IR Spectroscopic Survey of the Central Regions of Field Ellipticals", (PI D. R. Silva), a sample of 26 early-type galaxies has been observed on February 2^{nd}, 3^{rd} and 4^{th} 2000 with the 2.1 m telescope at Kitt Peak National Observatory (KPNO). The observational set-up used ONIS (Ohio State/NOAO Imaging Spectrograph) – a general-purpose imager and moderate-resolution spectrometer. This instrument is sensitive to the wavelength range between 1 and 2.4 μm and has an 512×1024 InSb infrared detector. Our spectra cover the K-band, between 2 and 2.4 μm, with the sampling of 8.36 Å per pixel. The slit width was $0\farcs68$, one pixel covered $0\farcs34$ on the sky. The spectral resolution was R~1300 measured from a HeNeAr lamp, used for the wavelength calibration. To observe each galaxy a standard near-IR observational technique has been used (see Section 2.4). Due to the long-slit mode, used in this study, there was no need for separate sky frames. Instead, during the exposure sequence for each galaxy, first the galaxy was centred on the slit near one end and an individual integration was executed. Then the galaxy was moved ~70'' towards the other end of the slit where another integration was executed. The galaxy was then returned to the original slit position where the next integration was obtained. This ABA pattern was repeated a number of times, resulting in multiple individual two-dimensional spectroscopic images. Each individual galaxy exposure lasted 240 s and series of 10 have been taken. After taking the galaxy spectra, an appropriate telluric star at similar airmass has been observed, following the same pattern as for the galaxy. Exposure time for the stars has been 20 s. After each galaxy + telluric star sequence a spectrum of the HeNeAr lamp has been taken. At the beginning of the observing night several dome flat exposures have been acquired. During day time series of dark exposures with the length of the science and calibration frames were made.

Due to problems with the detector, described bellow, we succeeded to extract spectra with sufficient signal-to-noise ratio only for 10 galaxies in our sample. Their basic properties are given in Table 5.1, together with the achieved signal-to-noise ratios of the final spectra. The list of the relevant telluric stars is given in Table 5.2.

Table 5.1: Galaxy sample and observing log.

Galaxy	Type	B	RA	Dec	σ	R_{eff}	S/N	Age
		(mag)	(hh:mm:ss)	(° : ′ : ″)	(km s^{-1})	(″)		
(1)	(2)	(3)	(4)	(5)	(6)	(7)	(8)	(9)
Maffei I	S0(pec)	-	02:36:35.4	+59:39:18	187	57	39	–
NGC 0821	E6	11.76	02:08:21.1	+10:59:42	212	49	15	O
NGC 2549	SA(r)	12.11	08:18:58.3	+57:48:11	143	20	19	Y
NGC 3377	E5-6	11.13	10:47:42.4	+13:59:08	132	38	13	I
NGC 3489	SAB	11.06	11:00:18.6	+13:54:04	108	19	23	Y
NGC 3607	SA(s)	10.93	11:16:54.6	+18:03:07	221	43	16	O
NGC 3608	E2	11.57	11:16:58.9	+18:08:55	182	41	13	O
NGC 3610	E5	11.62	11:18:25.3	+58:47:10	174	15	26	I
NGC 4570	S0(7)/E7	11.74	12:36:53.4	+07:14:48	180	14	16	O
NGC 5322	E3-4	11.05	13:49:15.3	+60:11:26	217	33	13	I

Notes: (1) Galaxy name, (2) galaxy type, (3) total B-band magnitude. For Maffei I this value is unknown, due to its location behind the Milky Way disk, (4) and (5) galaxy coordinates (column 3, 4 and 5 taken from NED), (6) central velocity dispersion (data from Fingerhut et al. 2003; Smith et al. 2000; Bernardi et al. 2002; Simien & Prugniel 1997; Denicoló et al. 2005), (7) effective radius (data from Kuntschner et al. 2006; Buta & McCall 1999, and derived from RC3), (8) signal-to-noise ratio of the resultant spectra close to the ^{12}CO (2–0) band-head, (9) Age group to which the galaxy belongs, as estimated from Figure 5.2. Y stands for galaxies with age < 3 Gyr, I for 3 < age < 7 Gyr, O for the galaxies with age > 8 Gyr.

Table 5.2: Telluric stars.

Star	Galaxy	RA	Dec	SpT
		(hh:mm:ss)	(° : ′ : ″)	
(1)	(2)	(3)	(4)	(5)
HR 0839	Maffei I	02:51:37	+58:19:12	A6V
HR 4227	NGC 3377	10:49:12	+10:32:57	A2V
HR 4227	NGC 3489	10:49:13	+10:32:56	A2V
HR 4366	NGC 3608	11:15:55	+12:50:57	A2V
HR 4865	NGC 4570	12:48:51	+14:07:42	A1V
HR 0578	NGC 0821	01:59:23	+12:17:46	A6V
HR 3235	NGC 2549	08:17:47	+59:34:40	A7IV
HR 4378	NGC 3607	11:18:20	+11:58:55	A2V
HR 4344	NGC 3610	11:12:44	+54:53:53	A4V
HR 5216	NGC 5322	13:50:27	+58:32:11	A3V

Notes: (1) Telluric star name, (2) galaxy, for which this star was used, (3) and (4) star coordinates, (5) spectral type.

5.3 Basic data reduction

The basic data reduction has been carried out with the help of various IRAF tasks within the package `ccdred`, following a standard long-slit data reduction technique.

5.3.1 Trim

The use of a filter to limit the spectrum to the *K*-band only causes a partial illumination of the detector. For this reason, prior to any data reduction, we have trimmed all of the raw frames and from here on we used only the useful 512×541 out of 512×1024 pixels.

5.3.2 Dark current

Early infrared detectors typically suffered from substantial dark current, caused by problems in the detector and the high thermal background of the instrument. In the case of ONIS the dark current is $\sim 1.2\, e^-/\mathrm{s}$, which is as high as the signal coming from the brightest galaxies in our sample. To correct for this we have obtained "master dark" frames for each night and exposure time setting after combining several dark frames taken during day time using a pixel reject algorithm. With these in hand, we have subtracted the relevant master dark frame from each individual galaxy or star exposure.

5.3.3 Flat field correction

The next step in removing the instrument signature is to flat-field the data. There are pixel-to-pixel gain variations caused by the detector itself or dust on the camera window. Flat field frames have been taken with the help of the illuminated dome. Then we combined the frames of each night using a median rejection algorithm, resulting in a "master flat". Then the master flats were normalised by fitting a cubic spline of high order (35 – 50) to the average continuum in wavelength direction and dividing each column by this fit. The resulting frames are referred to as "response" frames. Then the final step in flat-fielding was to divide each science frame by the response flat field.

5.3.4 Wavelength calibration and distortion correction

In order to wavelength calibrate our spectra, we used the NeHeAr lamp spectra, taken after each galaxy + telluric star sequence. In this way we ensure that the wavelength calibration and distortion correction will be optimal. We created a distortion map in wavelength direction of the detector using these lamp spectra by fitting a two dimensional polynomial to the wavelength as a function of a row and column to the position of ~ 15 spectral lines. The accuracy of the wavelength calibration was ~ 1.5 Å (1/5 pixel).

5.3.5 Background subtraction

Following the original design of the observations, in order to remove the sky contribution we have to simply subtract two consecutive science frames from each other. Since we have positioned the galaxy for the first frame at one end of the slit, and for the second frame to the other, the subtraction of the two frames would result in two background corrected images, with the only difference that the second one is negative. However, this approach turned out to be impossible, due to the presence of interference patterns, visible on the majority of the raw frames like waves, propagating in the spectral direction. These waves had different amplitudes and wavelengths for different frames, so their removal was practically impossible. For this reason we chose to determine the sky background contamination from areas located very close to the galaxy spectrum on the detector, but still far enough in order to avoid galaxy light over-subtraction. For this purpose we have estimated the regions where the galaxy spectrum is located and selected bands of width $\sim 5''$, where the contribution comes only from the sky (usually $\sim 10''$ outside of the galaxy). Then we interpolated the sky contribution to be subtracted from the galaxy spectrum. The same treatment was applied to the telluric stars.

5.3.6 1D spectrum extraction

After executing the above data reduction steps we obtained dark current subtracted, flat field corrected, wavelength calibrated and sky background corrected two dimensional images of the spectra for each galaxy and telluric star. After their careful examination we concluded that we cannot use the spectra, which are recorded on the right hand side of the detector due to a large amount of hot and dead pixels. This substantially reduced the number of our frames and thus for each galaxy we had only 5 out of 10 exposures to combine, and for the telluric stars 3 out of 6.

We extracted 1D spectra with the IRAF task `apall`. The extraction aperture was set to be 1/8 of the effective radius of the galaxies. Thus we have obtained five 1D spectra for each galaxy and three spectra for each telluric star. To obtain the final combined spectra we used a median rejection algorithm. The total exposure time for each galaxy was 1200 s and 60 s per telluric star.

5.3.7 Telluric correction

The last step of the data reduction is to remove the deep absorption lines originating in the Earth's atmosphere. We achieved this using the method described in Section 2.4. To correct the galaxy spectrum, first we have taken its associated telluric star and divided its spectrum by scaled black body spectrum with the same temperature as the star. In this way we obtained a telluric correction spectrum. Then the galaxy spectrum was divided by the telluric correction spectrum to yield a fully reduced spectrum, ready for scientific analysis. The final spectra are shown on Figure 5.1. The spectra were corrected for radial velocity shifts (see next paragraph). The solid vertical lines show the limits of the D_{CO} index passband, and the dashed lines – the extent of the continuum

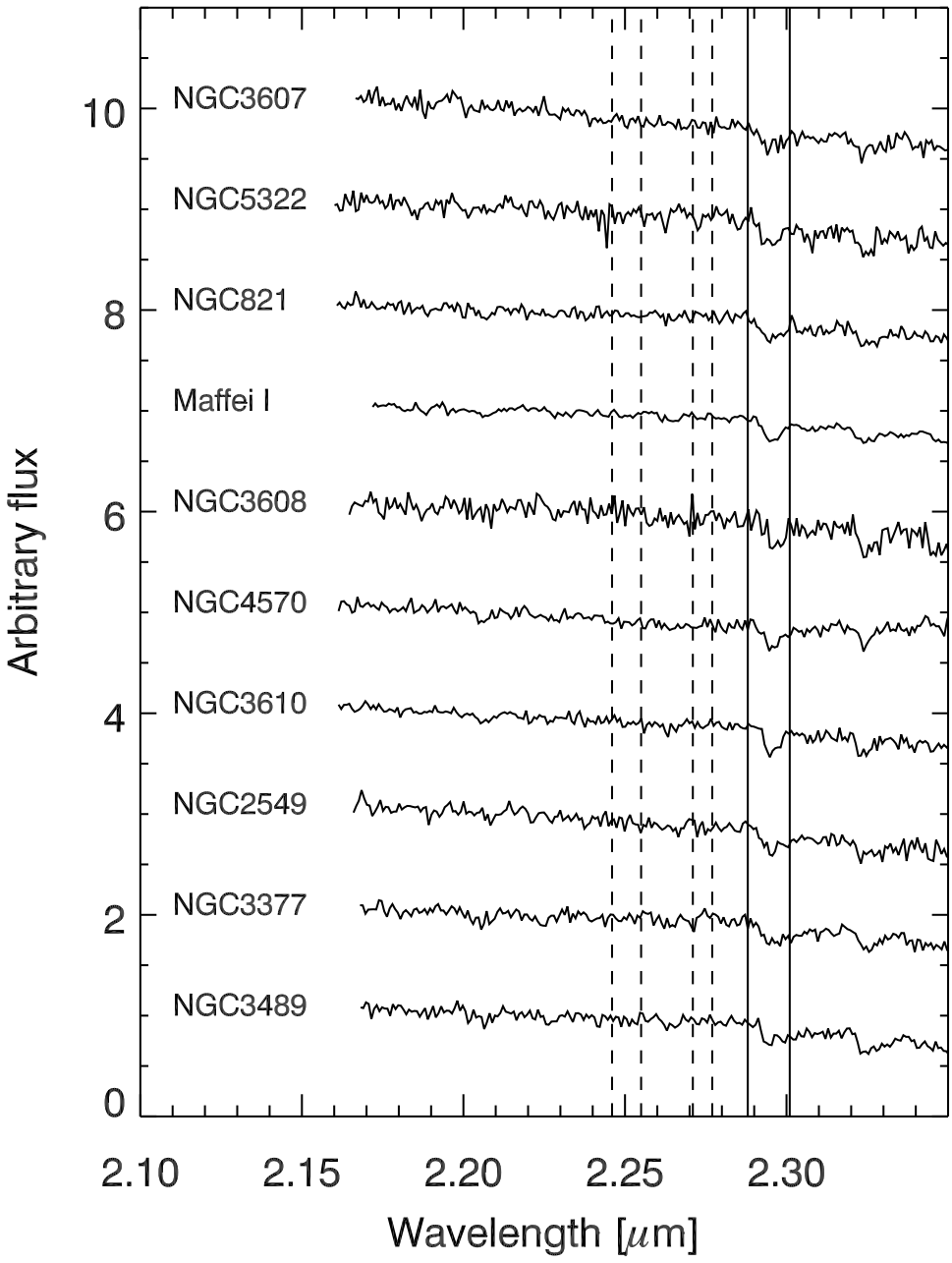

Figure 5.1: Fully reduced spectra of the sample of field early-type galaxies, ordered from top to bottom in decreasing velocity dispersion and corrected for radial velocity shifts. The solid vertical lines show the extent of the on feature passband, used to measure the D_{CO} index. The dashed lines mark the limits of the continuum passbands.

bands (for definition of the D_{CO} index see Chapter 3). We have estimated the achieved S/N ratio close to the ^{12}CO (2–0) band-head in the final spectra, with the help of the empirical method described by Stoehr et al. (2007), and listed the values in Table 5.1.

5.3.8 Measurements of near-IR line strengths

Before measuring the near-IR line strengths, we determined the recession velocities of the galaxies in our sample using a Fourier cross correlation technique (see Section 3.4.2) and de-redshifted the spectra accordingly. The combination of few absorption lines and low S/N did not allow us to determine reliably the central velocity dispersions, thus we used literature data (see Table 5.1 and references there). We note that these values have been inferred from optical spectra, however we do not consider that this is a source of significant error, when comparing with near-IR data, since Silva et al. (2008) show that central velocity dispersions, derived from optical and near-IR spectroscopy, are very similar for elliptical and S0 galaxies.

We have measured only the strength of Na I and the ^{12}CO (2–0) band head using the D_{CO} index, again due to the low quality of the spectra. The D_{CO} index definition is less sensitive to velocity dispersion and/or spectral resolution broadening and differences in the continuum shape (Mármol-Queraltó et al. 2008), as compared to the other ^{12}CO (2–0) index definitions, given in Chapter 3. In order to compare our sample of field early-type galaxies with galaxies in clusters, we have measured the D_{CO} index in the spectra, presented in Silva et al. (2008).

The Na I index is sensitive to changes in the velocity dispersion and the spectral resolution. We have corrected the index values for the internal velocity broadening in the galaxies, following the method, described in Section 3.4.3. In Section 3.4.1 we chose the standard spectral resolution to be 6.9 Å ($FWHM$) and we have broadened our spectra to match this value, where needed (e.g. the LMC globular cluster spectra, presented in Chapter 4). The spectra of the field early-type galaxies, discussed in this chapter, have a lower spectral resolution of 17.3 Å ($FWHM$). In order to be able to compare correctly the data with results from the previous chapter, we have to measure the indices on spectra, having the same spectral resolution. A natural choice is to smooth the LMC GCs spectra, obtained with VLT/SINFONI and Fornax galaxies, obtained with VLT/ISAAC to the lowest spectral resolution of the field galaxies. However, the spectroscopy of the field galaxies sample has been performed with an already decommissioned instrument. If we broad all spectra to its resolution, we will decrease the quality of the other data sets, obtained with contemporary instruments, and we will have to do the same in the future, thus loosing the advantage of the better data quality that current near-IR spectrographs offer. The lower spectral resolution broadens the spectral features in a similar way as the velocity dispersion. We have estimated the effect of the reduced spectral resolution, as compared to the resolution of the Fornax cluster galaxies spectra using Figure 3.4. The Na I index in field early-type galaxies, that we measure at a resolution of 17.3 Å ($FWHM$), is lower with ~ 3 % of the index value (~ 0.15 Å), as compared when measured at the resolution of 6.9 Å ($FWHM$), which is much less than the estimated errors (see Table 5.3). We decided to correct the Na I index in field early-type galaxies to correspond to the higher resolution data of

Fornax cluster galaxies and LMC globular clusters. We list the final values of the Na I and D_{CO} index in Table 5.3, together with their $1\,\sigma$ errors for both field and Fornax cluster samples.

Table 5.3: Near-IR indices, ages and metallicities of the early-type galaxies.

Galaxy (1)	Na I (2)	D_{CO} (3)	[Z/H] (4)	Age (Gyr) (5)
		Field galaxies		
Maffei I	4.03 ± 0.17	1.180 ± 0.003	–	–
NGC 0821	4.78 ± 0.60	1.211 ± 0.009	0.21 ± 0.06	11.52 ± 1.10
NGC 2549	4.39 ± 0.61	1.235 ± 0.011	0.49 ± 0.08	2.70 ± 0.36
NGC 3377	6.33 ± 0.41	1.208 ± 0.007	0.12 ± 0.03	6.37 ± 1.09
NGC 3489	4.78 ± 0.42	1.174 ± 0.007	0.15 ± 0.02	1.70 ± 0.05
NGC 3607	2.16 ± 0.62	1.260 ± 0.011	0.27 ± 0.06	15.00 ± 0.48
NGC 3608	3.84 ± 1.00	1.224 ± 0.017	0.09 ± 0.08	14.04 ± 1.35
NGC 3610	5.35 ± 0.50	1.198 ± 0.008	0.21 ± 0.09	4.89 ± 1.64
NGC 4570	5.22 ± 0.52	1.158 ± 0.007	0.36 ± 0.06	11.52 ± 1.52
NGC 5322	4.56 ± 0.80	1.216 ± 0.012	0.52 ± 0.14	3.76 ± 2.28
		Fornax cluster galaxies		
NGC 1316	4.70 ± 0.14	1.225 ± 0.001	0.64 ± 0.08	1.82 ± 0.06
NGC 1344	4.33 ± 0.09	1.203 ± 0.002	0.55 ± 0.09	2.37 ± 0.41
NGC 1374	4.12 ± 0.09	1.206 ± 0.001	0.36 ± 0.12	10.79 ± 3.84
NGC 1375	3.50 ± 0.20	1.188 ± 0.004	0.15 ± 0.09	1.59 ± 0.18
NGC 1379	2.87 ± 0.13	1.189 ± 0.002	0.08 ± 0.09	10.79 ± 2.69
NGC 1380	4.49 ± 0.07	1.198 ± 0.002	0.52 ± 0.12	4.89 ± 2.78
NGC 1381	3.32 ± 0.09	1.200 ± 0.002	0.18 ± 0.06	10.10 ± 2.01
NGC 1399	5.35 ± 0.22	1.203 ± 0.002	0.49 ± 0.09	14.04 ± 2.77
NGC 1404	4.79 ± 0.06	1.206 ± 0.002	0.40 ± 0.08	10.79 ± 2.59
NGC 1419	2.86 ± 0.08	1.190 ± 0.001	-0.07 ± 0.11	13.15 ± 3.07
NGC 1427	3.43 ± 0.11	1.194 ± 0.002	0.12 ± 0.05	11.52 ± 1.63

Notes: (1) Galaxy name, (2) Na I index, expressed in Å (the index for Fornax cluster galaxies is taken from Silva et al. (2008), (3) D_{CO} index, (4) [Z/H] and (5) age, as derived from the optical age-metallicity indicators from Figure 5.2.

5.4 Near-IR indices in early-type galaxies

In this section we are going to explore the near-IR spectral properties of our sample of field early-type galaxies and compare them with literature studies of the population of early-type galaxies in the Fornax cluster. We will also compare the near-IR properties

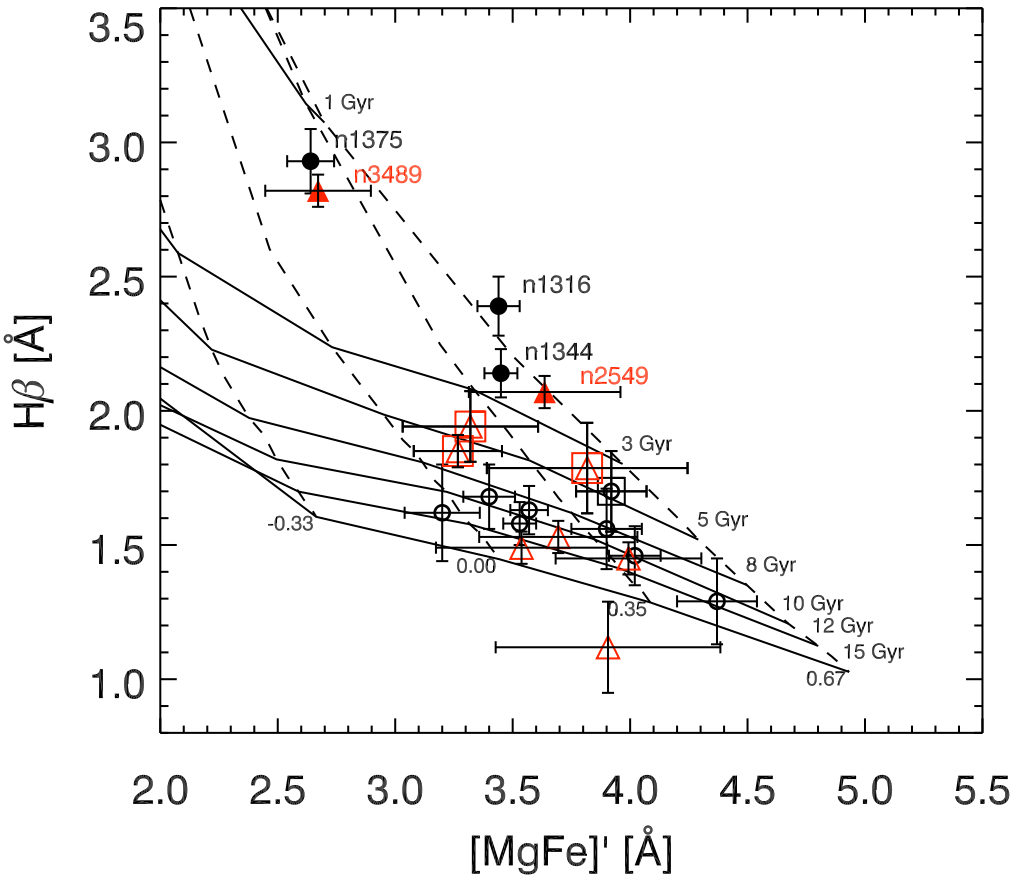

Figure 5.2: Hβ vs. [MgFe]' diagram, with overplotted stellar populations models from Thomas et al. (2003) for solar abundance ratios, used to derive ages and metallicities of early-type galaxies. Dashed lines show constant metallicity, solid lines constant age. Circles represent early-type galaxies in the Fornax cluster from the study of Silva et al. (2008), red triangles represent the values for the field galaxies sample (data from Trager et al. 1998; Kuntschner et al. 2006). Galaxies from the two samples, which have clear signatures of younger populations ($\leq$ 3 Gyr), are marked with filled symbols. The galaxies with ages between 3 and 7 Gyr are marked additionally with squares.

with the much better explored optical ones and try to understand which are the main drivers of near-IR indices. In Figure 5.2 we show the classical optical diagram, used to derive ages and metallicities of early-type galaxies. It includes Hβ and the combined [MgFe]' index [1]. We have overplotted stellar populations models from Thomas et al. (2003) for solar abundance ratios. Red triangles represent the field early-type galaxies, black circles – Fornax cluster members. Lick indices for Fornax galaxies are taken from Silva et al. (2008). Mg b and Hβ index values for the field galaxies are coming from Kuntschner et al. (2006), except of NGC 3607, NGC 3610 and NGC 5322, for which data are taken from Trager et al. (1998). Fe5270 and Fe5335 values are taken also from the same study for the whole field galaxies sample. Lick indices, given in Kuntschner et al. (2006) and Silva et al. (2008), are measured from spectra covering 1/8 of the effective radius of the galaxies and thus are identical to our extraction radii. Trager et al. (1998) used a fixed slit width and length ($1\farcs4 \times 4\farcs0$) for their spectra extraction, however we do not consider these differences to be a potential source of significant errors.

Using Figure 5.2 we have estimated the ages and the metallicities of the galaxies in both samples and listed them in Table 5.3. According to this plot we have five galaxies with a population with luminosity weighted age of less than 3 Gyr. These are particularly important for our case study, because at that evolutionary stage we expect to see the largest contribution from TP-AGB stars. In our sample of field galaxies these are NGC 3489 and NGC 2549. They are shown with filled red triangles. NGC 3489 exhibits dust and irregular elliptical isophotes (Kuntschner et al. 2006). The Fornax galaxies, which have significant contribution from younger stars, are NGC 1375, NGC 1316, and NGC 1344. They are marked with filled black circles. The next age group of galaxies in Figure 5.2 has ages between 3 and 7 Gyr. In our sample of field galaxies these are NGC 3610, NGC 3377 and NGC 5322. We have indicated them with open red squares on top of the triangles. From the Fornax cluster sample NGC 1380 falls into this group. We have indicated it with a square on top of the black circle. Central gas has been traced in both NGC 3610 and NGC 5322 (Goudfrooij et al. 1994), NGC 5322 reveals a prominent dust lane (van Dokkum & Franx 1995), the presence of dust in NGC 3610 is not so obvious, but cannot be ruled out (Silva & Bothun 1998b). The central near-IR colours of these two galaxies are consistent with the presence of intermediate age AGB stars (Silva & Bothun 1998b). NGC 1380 contains an optically thick central dust lane, which is easily visible on HST images (Silva et al. 2008). The third group of galaxies in Figure 5.2 are the quiescent galaxies with ages between 8 and 15 Gyr. Fornax cluster galaxies are indicated with open circles, field galaxies with red open triangles.

In the following when discussing these three groups we will refer to them as galaxies with young population, for objects that have SSP luminosity weighted ages ≤ 3 Gyr, intermediate age galaxies, for the ones with ages between 3 and 7 Gyr and old population for the galaxies with age > 8 Gyr.

For one galaxy in our sample we were unable to find Lick indices in the literature. This is Maffei I, which is situated at very low Galactic latitude behind the Milky Way disk and is very difficult to observe in optical light, due to the heavy galactic extinction in this direction. However it is much easier to observe it in near-IR light and here we

[1] [MgFe]'= $\sqrt{Mg\,b * (0.72Fe5270 + 0.28Fe5335)}$, (Thomas et al. 2003)

will include only its near-IR indices.

5.4.1 Scaling relations in field and cluster early-type galaxies

In Figure 5.3 we show several index-σ scaling relations in the optical and the near-IR. In all panels Fornax cluster galaxies are denoted with black circles and the galaxies from our sample with red triangles. The filled symbols mark the galaxies, which have clear signatures of a younger population, i.e. strong Hβ and weak [MgFe]' index values, the square symbols mark the galaxies with age between 3 and 7 Gyr (see Figure 5.2). In all panels we have shown the least-squares linear fit to the old galaxies in the Fornax cluster with dashed lines. The first panel in Figure 5.3 shows the dependence of Hβ on the central velocity dispersion of the galaxies. Old Fornax galaxies show a nice anti-correlation with the central velocity dispersion. Old field early-type galaxies follow the same correlation. Both field and Fornax galaxies with younger populations are located above the main relation, which is valid for the intermediate age field galaxies as well.

The next panel shows the well known Mg - σ relation (e.g. Burstein et al. 1988; Bender et al. 1993; Colless et al. 1999). This relation demonstrates that the most massive galaxies (those with higher σ) have also higher metallicity. Both Fornax and field old galaxies follow it. The younger objects in the two samples tend to have lower Mg b index strength as compared to old galaxies with the same velocity dispersion.

The following panel shows the correlation of the near-IR Na I index with σ. Old Fornax galaxies show a very narrow correlation, while the field sample exhibits a larger spread. Both field and Fornax galaxies with a contribution from a younger population show a higher Na I index than old galaxies. This result was already pointed out in Silva et al. (2008). Here we confirm it with an extended sample, including field early-type galaxies. The sub-sample of intermediate age field galaxies also shows higher Na I index values. This, taken together with our LMC globular clusters data, discussed in Section 4.5, suggests that the near-IR Na I index is sensitive to young stars. At old ages this index correlates well with the metallicity.

The last panel in Figure 5.3 shows the correlation of the D_{CO} index with the central velocity dispersion. In this plot the D_{CO} index in old Fornax galaxies increases steadily with σ, the younger galaxies again have slightly higher index values. However, the field galaxies sample shows a complex behaviour with a significant scatter in the old galaxies. Field galaxies with traces of younger populations also have different D_{CO}. For one of them, NGC 3489, which has the strongest Hβ absorption in our sample, the index is bellow the main relation, while for the next youngest galaxy, NGC 2549, the D_{CO} index is above the relation.

In Figure 5.2 and 5.3 there is one galaxy, NGC 3607, which has an unusually weak Hβ and Na I index, with very strong D_{CO} index. This galaxy is substantially deviating from the stellar population models and scaling relations. The reason for this is not clear, so we have chosen to exclude it from our analysis and it is not plotted from here on.

In Figure 5.4 we show the correlations between different index-σ fit residuals. To obtain them we have subtracted from each observed data point for a given index the weighted linear fit of index to velocity dispersion for old Fornax early-type galaxies,

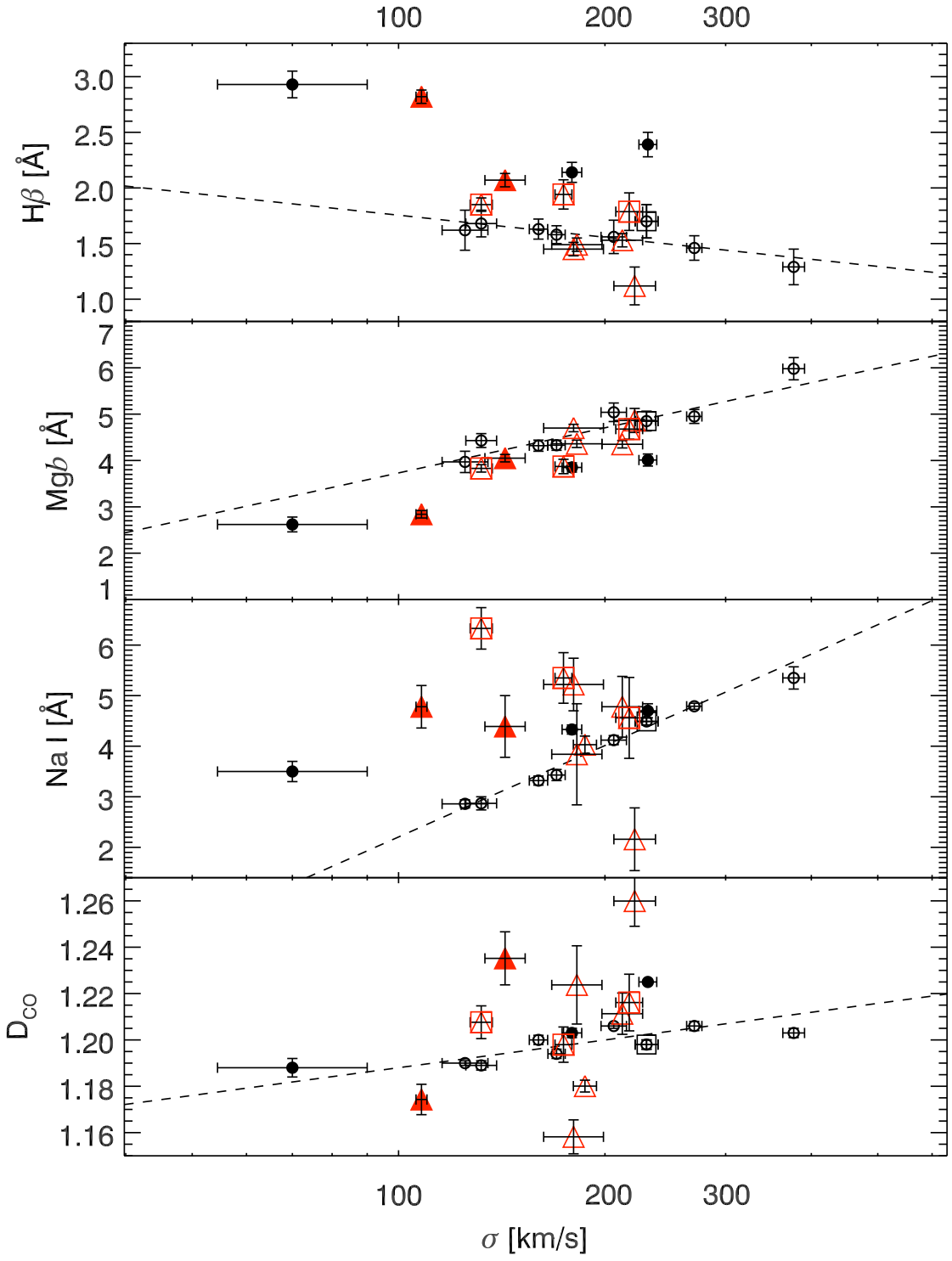

Figure 5.3: Optical and near-IR scaling relations. From top to bottom: the optical Hβ, Mgb, the near-IR Na I and D_{CO} index vs. central velocity dispersion σ. Colour and symbol coding for the galaxies is the same as on Figure 5.2. The dashed lines on every plot show the least-squares linear fit to the old Fornax galaxies (open circles).

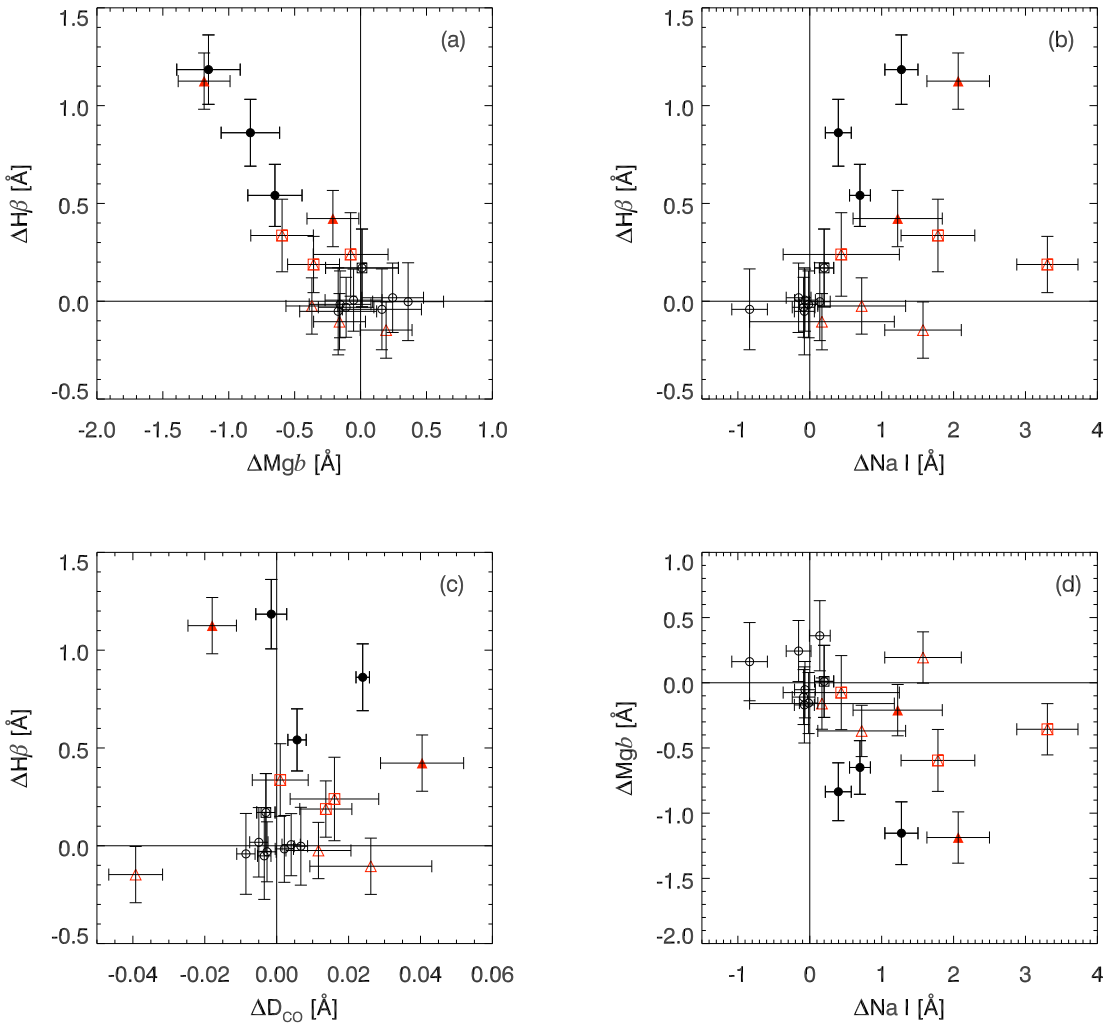

Figure 5.4: Index–σ fit residuals. Colour coding and symbols are the same as on previous plot. ΔIndex gives the residual of the weighted linear fit of this index to the velocity dispersion of old Fornax cluster galaxies, shown in Figure 5.3.

showed on Figure 5.3 with dashed lines. Colour coding and symbols are the same as on previous plots. Panel (a) shows a very nice anti-correlation between the Hβ and Mg b fit residuals for young and intermediate age galaxies. Panel (b) shows that the fit residuals of Hβ and the near-IR Na I index correlate well for young and intermediate age galaxies. Yet another confirmation of the conclusion we made in the previous paragraph that Na I index reacts to the presence of young stars. Panel (c) once more illustrates the complex behaviour of the near-IR D_{CO} index. Fit residuals for younger and intermediate age galaxies in general correlate with Hβ residuals, however there are exceptions. The last panel, (d), shows general anti-correlation between Na I and Mg b fit residuals.

In summary, near-IR Na I and D_{CO} index correlate with the central velocity dispersion of early-type galaxies, similar to the optical ones. This correlations are very well expressed in the case of old Fornax cluster galaxies. We have shown that the metallicity scaling of the central velocity dispersion of early-type galaxies, known from the optical metallicity indicator Mg b, is seen with the near-IR Na I index as well. Old field early-type galaxies exhibit a larger spread, however we consider this is due to the lower quality of the data, as compared to the Fornax cluster data. Galaxies with young and intermediate ages stand out of the main correlations.

5.4.2 Index-index diagnostic diagrams

In Figure 5.5 we show various diagnostic diagrams, using optical and near-IR indices. On panel (a) we repeat Figure 5.2 for guidance. We have omitted NGC 3607 as discussed in the previous section. The colour and symbol coding in this figure is the same as in the previous plots, i.e. red triangles represent the field early-type galaxies, black circles Fornax cluster members. The dashed lines in panels (c), (d) and (f) show the least-squares linear fits to the old Fornax galaxies only.

Some of these diagrams can be used to separate quiescent (old) galaxies from those with signatures of recent star formation (filled symbols). In panels (c) and (d) we plot the dependence of the near-IR indices D_{CO} and Na I on the optical metallicity indicator [MgFe]'. In the D_{CO} vs. [MgFe]' diagram the old Fornax galaxies follow a clear correlation, the younger galaxies have generally higher D_{CO} values as compared with their older counterparts with similar [MgFe]'. The field galaxies show a larger spread and follow to some extent the relation for the old Fornax galaxies. The Na I vs. [MgFe]' diagram is a better tool to distinguish young from old galaxies. Silva et al. (2008) have shown this plot for the Fornax galaxies only, here we add our field sample. Young and intermediate age field early-type galaxies are well separated from the relation valid for the old galaxies.

In the next two panels we show the dependence of the optical age indicator Hβ from near-IR indices (panels (e) and (f)). Both of them show the separation between young and old galaxies clearly. Old field galaxies follow the relation for the Fornax old galaxies. However, the behaviour of the D_{CO} index is more complicated at younger ages. Field galaxies with strong Hβ have both weak and strong D_{CO}. This may be due to the fact that D_{CO} index depends strongly on the metallicity when the age is around 1 Gyr (what actually is the derived age of the young field galaxies, according to the Hβ

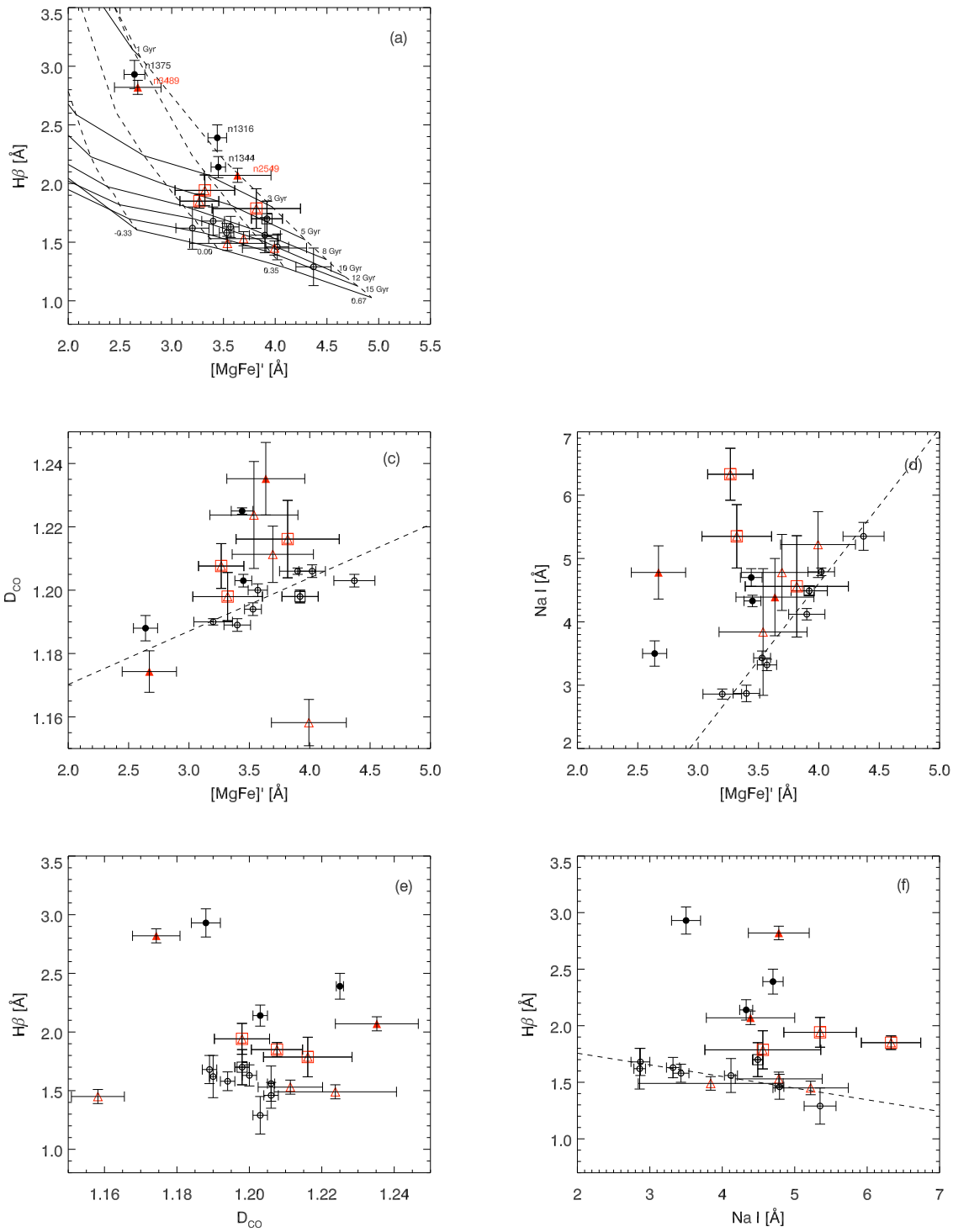

Figure 5.5: Various index-index diagnostic diagrams. Panel (a) is repeating Figure 5.2 for guidance. Colour and symbol coding for the galaxies is the same as in previous figures. The dashed lines in panels (c), (d) and (f) show the linear least-squares fits to the old Fornax galaxies.

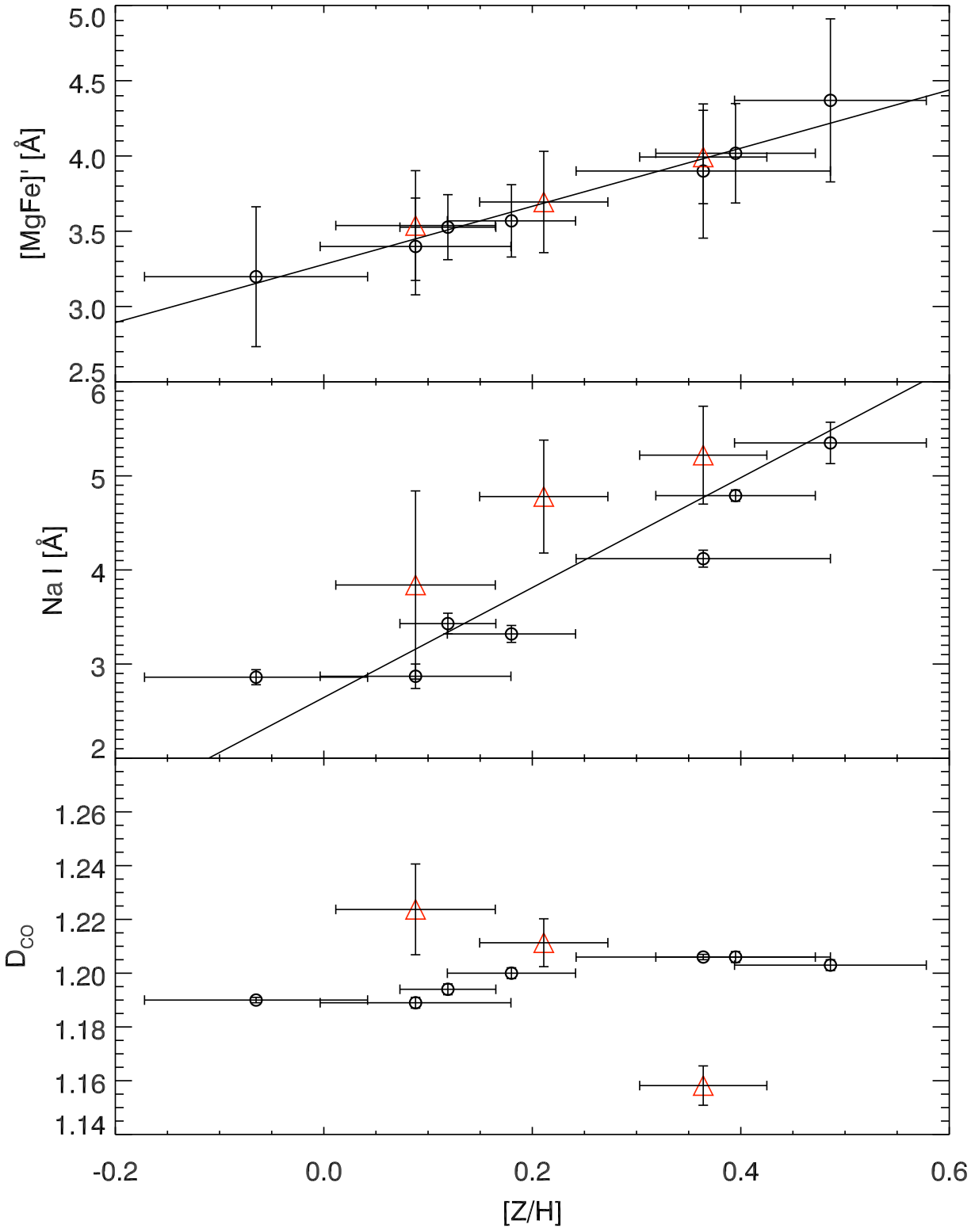

Figure 5.6: Optical and near-IR indices for old Fornax (open circles) and field (red triangles) early-type galaxies vs. their metallicity, derived from Figure 5.2. The solid lines in the top plots represent the weighted linear fit to all data points.

vs. [MgFe]' diagram).

The resemblance of panel (f) with panel (a) is remarkable. The Na I index tracks the metallicity of the old Fornax galaxies, as suggested earlier, while the Hβ strength decreases mildly. Field galaxies follow this relation as well. The four intermediate age galaxies are clearly separated from the other two age groups. Young Fornax and field galaxies are also well distinct from the older ones. Therefor similar plots, based on these two indices, promise to be good age-metallicity diagnostic diagrams, when better stellar population models in the near-IR become available. The differentiation in age and metallicity looks not as complex as it is, when using Hβ vs. [MgFe]'.

This argument is further supported in Figure 5.6, where we show the dependence of optical and near-IR line strengths from the metallicity of the galaxies, which we have derived from Figure 5.2 (see Table 5.3). The top panel shows the optical metallicity indicator [MgFe]' for old Fornax (open circles) and field (red triangles) early-type galaxies. The solid line represents the weighted linear fit to the data and has an equation:

$$[MgFe]' = 3.279 \pm 0.218 + 1.931 \pm 0.853\,[Z/H] \tag{5.1}$$

For the middle panel we have used the near-IR Na I index. The correlation between this index and the metallicity is very good. The weighted linear fit has an equation:

$$NaI = 2.644 \pm 0.315 + 5.841 \pm 1.260\,[Z/H] \tag{5.2}$$

The bottom panel shows that the D_{CO} index tends to saturate for [Z/H] > 0.2.

5.5 Comparisons with stellar population models

In Figure 5.7 we show a comparison of our sample of field early-type galaxies, together with Fornax cluster members, with the current SSP models of Maraston (2005) for the D_{CO} index. As discussed in Section 4.4, these models do not give a good description of the D_{CO} index at sub-solar metallicities and intermediate age, but for older ages, solar and higher metallicities they may be describing the data well. The D_{CO} index values, measured from the theoretical models, also have to be interpreted with caution (see the discussion in Section 4.4.2). This index definition is not suitable to measure the D_{CO} index on that low spectral resolution SEDs ($\sim$ 200 Å in $FWHM$). However, the expected error is of the order of $\sim$ 3 % of the index value and is not going to influence our findings. We will use the D_{CO} index values of the theoretical SEDs as an estimate of the general trends of dependence from age and metallicity. When higher spectral resolutions models become available the following comparisons should be re-maid to obtain more quantitative estimates.

In the top panel we have marked with a black rectangle the locus of the D_{CO} index values for old Fornax early-type galaxies. The age range has been chosen according to the optical age-metallicity diagram, presented in Figure 5.2 and extends between 8 and 14 Gyr. The data agree reasonably well with the models for super-solar metallicity. With an open circle and a square we have indicated NGC 1380, the only Fornax galaxy in the intermediate age range. With solid black circles we have indicated the three

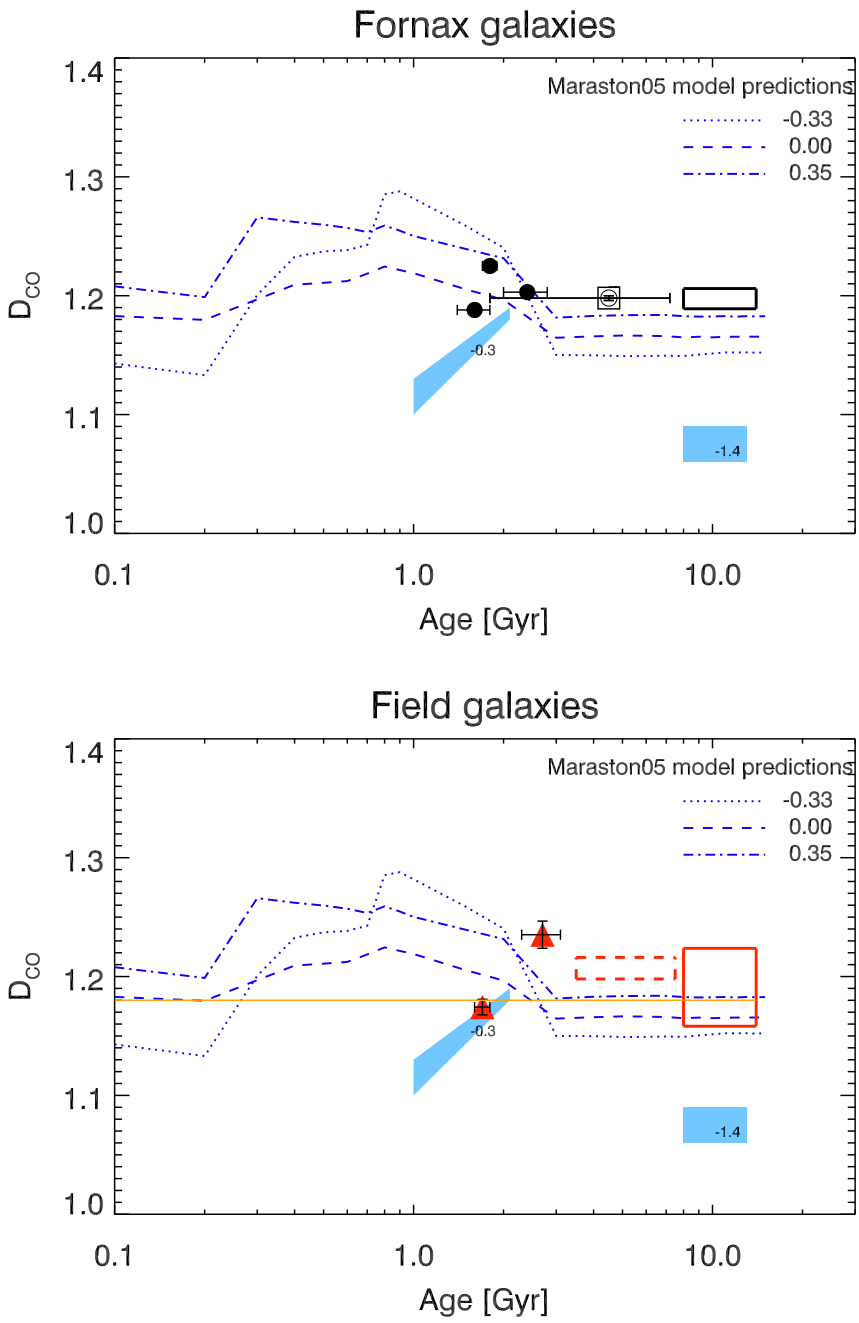

Figure 5.7: Comparison of the predictions of the stellar populations models of Maraston (2005) with Fornax cluster (top panel) and field galaxies (bottom panel). Dark blue lines indicate different metallicities. The region, surrounded by a black rectangle is the locus of D_{CO} index values for old Fornax cluster galaxies. The region, surrounded by red rectangle (bottom panel) shows the extent of the D_{CO} index in old field galaxies (8 – 14 Gyr). The dashed red rectangle shows the D_{CO} index in intermediate age (3 – 7 Gyr) galaxies. Filled symbols indicate the two young galaxies. The light blue shaded regions show our own calibration of the D_{CO} index from Chapter 4 for metallicities indicated in the boxes. The horizontal orange line indicates the D_{CO} index value for Maffei I.

galaxies in the Fornax cluster, which have signatures of a younger population according to Figure 5.2. For the two galaxies at ~2 Gyr, NGC 1316 and NGC 1344, the D_{CO} index agrees with the models for metallicity of [Z/H] ~ 0.35 (the derived metallicities for these galaxies from Figure 5.2 is about 0.6). However, the youngest Fornax cluster galaxy in the sample, NGC 1375, has a lower D_{CO} index as compared to the model predictions for the optical indices expected metallicity of solar or twice solar.

In the bottom panel we show the same models, this time together with data of our field early-type galaxies sample. The red rectangle shows the location of the old field galaxies and extends between 8 and 14 Gyr. The red dashed rectangle indicated the location of the D_{CO} index values in the intermediate age galaxies, with ages between 3 and 7 Gyr. The red filled triangles mark the two galaxies with a contribution from a young population, visible in Figure 5.2. Our sample of old field galaxies shows a similar behaviour as the Fornax cluster galaxies with a larger spread in the D_{CO} index. The galaxy at ~2 Gyr, NGC 2549, exhibits an increase in D_{CO}, consistent with the models, while the same index, measured in the youngest galaxy, NGC 3489, has a lower value.

In Figure 5.7 we have also included our observations of globular clusters (GCs) in the LMC, presented in Section 4.4, and indicated their D_{CO} index values with blue shaded regions. The metallicities are noted inside these regions. There we have seen the same trends as with the early-type galaxies in this chapter: the youngest objects in our samples with ages ~1 Gyr have a too low D_{CO} index value, compared to the models. In Section 4.4 we have discussed, as a possible reason for this disagreement, the carbon stars, which are the major contributor to the *K*-band light in intermediate age clusters. Their D_{CO} index is very much dependant on the metallicity (see Figure 4.19 and discussion in Section 4.4.2). In that section we reached the conclusion that models, calibrated with carbon stars with improper metallicity may be the reason for the disagreement with the data, however other factors, than metallicity, may also play a role. With the GCs we tested the case of half-solar metallicity. Here we see a similar behaviour in early-type galaxies which presumably have higher metallicities. There are two possible explanations. First, the most important contributors to the luminosity weighted D_{CO} index in these very young galaxies (~1 Gyr, according to SSP models) are stars, which have formed from metal poor gas. Second, the current carbon star sample from the Milky Way (Lançon & Mouhcine 2002) may be not enough to establish the spectral properties of carbon stars with different metallicities, using assumptions about the stellar evolution. The LMC clusters with age ~1 Gyr have $D_{CO} \sim 1.12 \pm 0.01$, while in NGC 1375 it is 1.19 ± 0.004. This difference may be explained with the higher metallicity of the young stars, which favours less carbon star production and brings the D_{CO} index up. In order to confirm this speculation there is a need for a larger sample of near-IR spectra of AGB stars (carbon and oxygen rich) to be able to derive a more consistent picture of this very important stellar evolutionary phase and its contribution to the integrated properties of globular clusters and galaxies.

In Figure 5.8 we show another near-IR index as a function of the age of the galaxies: the Na I index. Like in Figure 5.7, we indicated our calibration of this index regarding age and metallicity, derived from our own work on LMC GCs, presented in Chapter 4 with blue shaded regions (metallicity values are given in the regions). From Figures 5.3 and 5.5 and their discussion in the text we know that in old Fornax cluster galaxies

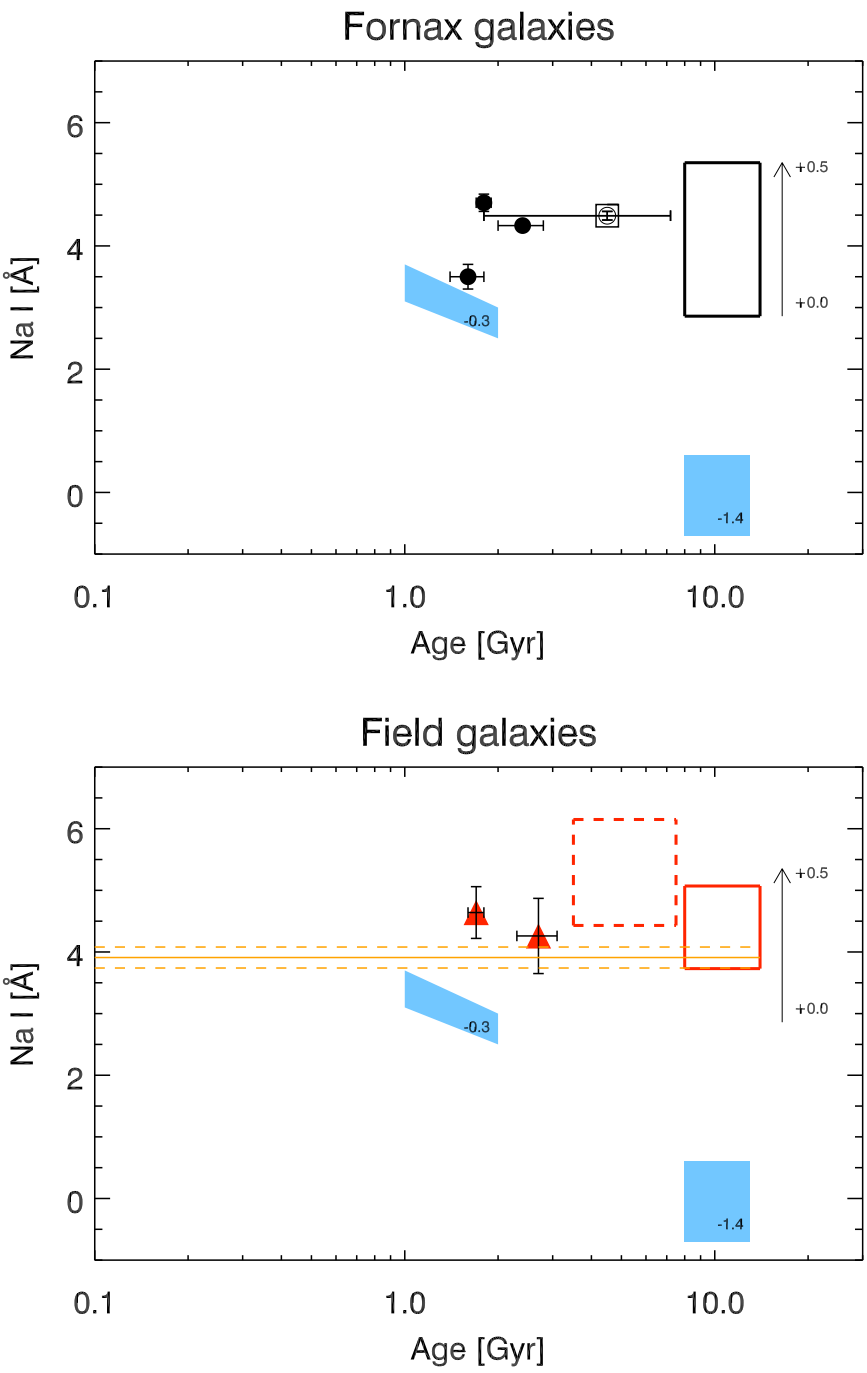

Figure 5.8: Na I index in Fornax and field early-type galaxies, plotted vs. their age. Colours, symbols and ages as in Figure 5.7. With blue shaded regions we have shown the values of Na I index for different metallicities (as noted in each region), derived from our own work on LMC globular clusters (Chapter 4) for sub-solar metallicity. The Na I index as a function of the metallicity of old Fornax early-type galaxies is shown with an arrow, extending between [Z/H]=+0.0 and +0.5. The horizontal orange solid and dashed lines indicate the Na I index and its error for Maffei I.

the Na I index is proportional to the metallicity. This we have indicated with an arrow, showing the metallicity range between [Z/H]=+0.0 and +0.5.

Na I in Fornax cluster galaxies (top panel) is consistent with the LMC calibration for the galaxies at ~ 2 Gyr, after we take into account their higher metallicity, as compared to the LMC. However, our sample of globular clusters and galaxies is limited to distinct groups of sub-solar and above solar metallicities and we do not have a clear picture of the development of the near-IR indices at metallicities in between. In field galaxies (bottom panel) we have used the same symbols to indicate the young, intermediate age and old galaxies, like in Figure 5.7 Na I tends to increase with decreasing age, which is consistent with our observations of LMC globular clusters, discussed in Section 4.5, but scaled to the higher metallicity of the galaxies.

In the Figures 5.7 and 5.8 we have indicated the D_{CO} and Na I index value of Maffei I with orange solid lines. The 1σ error bar is indicated only for the Na I index (dashed orange line), because for the D_{CO} index it is rather small (0.003) and overlaps with the index value. Given that there are no literature measurements of the optical indices we cannot infer an estimate of the age and the metallicity of this galaxy only from our near-IR spectra and will have to wait until more detailed near-IR stellar population models become available.

In Figure 5.9 we show a diagnostic diagram based on a combination between optical and near-IR indices. SSP models for the optical Hβ index are taken from Thomas et al. (2003). The D_{CO} index values have been computed from the model SEDs of Maraston (2005) for Kroupa IMF. Clearly a better choice for this diagram would be the near-IR Na I index vs. Hβ, as already discussed in Section 5.4. However, the measurement of the Na I index from the current near-IR theoretical SEDs is practically impossible, due to their very low spectral resolution. As in previous figures we overplotted the index values for the field and Fornax cluster early-type galaxies. Old galaxies follow the trends of decreasing Hβ and increasing D_{CO}, expressed by the solid lines of constant age and increasing metallicity. The four intermediate age galaxies follow a similar trend, shifted towards younger age. The interpretation of the indices for the galaxies with optical signatures of a younger population is more difficult, due to the complex behaviour of the near-IR D_{CO} index. In this figure the data points describing the old and intermediate age galaxies are located outside of the model predictions. However, this might be due to the expected weakness of the D_{CO} model index values, as discussed at the beginning of the section, due to the very low spectral resolution of the theoretical SEDs. The arrow at the bottom left corner of the plot gives an estimate of the correction factor, that has to be added to the models to simulate the D_{CO} index at the spectral resolution of the data. When this correction factor is taken into account, the agreement between the data and the models is very good.

5.6 Conclusions

In this chapter we have discussed the near-IR central index properties of a sample of early-type galaxies in low density environments, throughout the text referred as to field galaxies. We compared them with literature studies of Fornax cluster galaxies and we

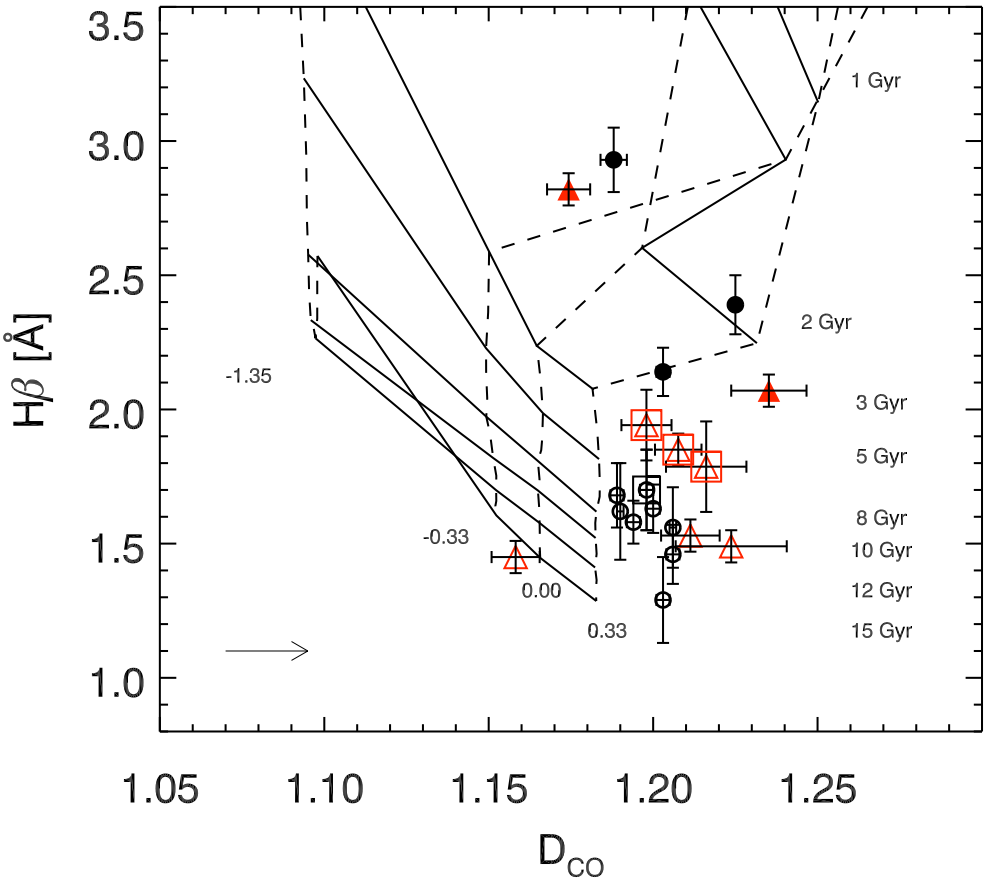

Figure 5.9: Combination of optical and near-IR SSP models. Hβ index predictions are from Thomas et al. (2003). The D_{CO} index predictions are computed from the SEDs of Maraston (2005). Solid lines represent constant age, dashed lines constant metallicity. Field and Fornax cluster galaxies are overplotted as on previous plots. The arrow at the bottom left corner indicates the correction factor to be added to the models to simulate the D_{CO} index at the spectral resolution of the data.

explored the similarities and the differences with a variety of methods. We divided the two galaxy samples into three sub-groups, based on their luminosity weighted, SSP-equivalent age, as derived from optical spectral indices. The group of young galaxies consists of five objects with ages ≤ 3 Gyr. We have four intermediate age galaxies with ages between 3 and 7 Gyr. The rest of the samples (eleven galaxies in total) we call old galaxies.

Index-σ scaling relations in the optical and the near-IR. Near-IR index-σ relations correlate with the optical ones. Both, the Na I and D_{CO} index, correlate with the central velocity dispersion for old field and Fornax cluster galaxies, although field galaxies exhibit a larger scatter. We consider this scatter is due to the lower quality of the field galaxies data. Here we compare spectra obtained with a 2 m class telescope and an early near-IR detector (the field sample is observed with the 2.1 m KPNO telescope) with an 8 m class telescope and more advanced instrument (the Fornax sample has been acquired with VLT/ISAAC). Silva et al. (2008) pointed out that the Na I index is strongly correlated with the σ in old Fornax cluster galaxies. Here we confirm this result by adding data for old field early type galaxies. Galaxies with clear signatures of recent star formation do not follow the main D_{CO} and Na I index-σ relations for old galaxies.

Na I and D_{CO} indices and the metallicity. The near-IR Na I index shows a good correlation with the optical metallicity indicator [MgFe]' for old Fornax galaxies. Thus it shows that it is significantly influenced by the metallicity of the population at old ages. We derive an empirical calibration for the Na I index as function of metallicity. The D_{CO} index also increases with increasing metallicity, although with a shallower slope, and agrees roughly with the SSP models of Maraston (2005).

Na I and D_{CO} indices and the age. Field and Fornax cluster galaxies with optical signatures of a recent star formation are clearly distinguished in several diagnostic diagrams. Na I tends to increase with decreasing age in early-type galaxies, as well as in LMC globular clusters. The D_{CO} index exhibits a more complex behaviour. It increases with decreasing age in galaxies with age up to ~ 2 Gyr and then weakens for galaxies at ~ 1 Gyr luminosity weighted and SSP equivalent age. Such trends are consistent with the presence of TP-AGB stars in the galaxies. We have seen the same in Chapter 4 for globular clusters in the LMC, which have sub-solar metallicity.

Comparisons with stellar population models. In this chapter we have tested the above solar metallicity regime of stellar populations. Current near-IR SSP models agree with the D_{CO} index for old early-type galaxies, but a correction factor to account for the poor spectral resolution of the models have to be considered. There are signatures that the models overestimate this index at very young ages, however there are also other possible explanations. This observation implies the need for a better understanding of the most important contributors to the near-IR light in young and intermediate age globular clusters and galaxies, i.e. AGB stars. This understanding is of paramount importance to the study of high redshift galaxies, close to the time of their formation. The near-IR Na I index reacts stronger to the presence of AGB stars at that stage, as compared to D_{CO}. For older ages it tracks the metallicity of the population. Thus we consider the combination between the optical Hβ index and the near-IR Na I index as a potentially good age-metallicity indicator once more sophisticated stellar population

models become available.

Chapter 6

Central K-band kinematics and line strength maps of NGC 1399

based on M. Lyubenova, H. Kuntschner, and D. R. Silva
Astronomy & Astrophysics, 2008, 485, 425

6.1 Introduction

The centres of giant early-type galaxies are interesting laboratories for exploring important questions about the physics of early-type galaxy assembly and star formation history. In particular, the ultimate goal is to tie the formation of global properties to such central properties as nuclear stellar populations, super-massive black holes, and active galactic nuclei.

The recently developed technique of near-infrared integral field spectroscopy in conjunction with adaptive optics offers a new window into these astrophysical questions by probing spatial scales (~0.″1 or better) heretofore only accessible to the instruments on the Hubble Space Telescope (HST). At the distance of the Fornax cluster (~ 20 Mpc) this corresponds to a spatial resolution of about 10 pc, which can be achieved over a 3″ × 3″ field-of-view with e.g., VLT/SINFONI. Although with limited field of view, this setup can be used to scrutinise compact stellar subsystems such as globular clusters or the nuclear regions of galaxies.

Today it is widely accepted that many massive and bright early-type galaxies contain super-massive central black holes (SMBH) with masses reaching up to $10^9\,M_\odot$, which tightly correlate with the physical properties of the host galaxies (Kormendy & Richstone 1995; Gebhardt et al. 2000; Ferrarese & Merritt 2000). Recently, it was shown that the nuclei of low- and intermediate luminosity early-type galaxies in the Fornax and Virgo clusters exhibit a (often blue) central (<0.02 effective radii) light excess in contrast with high-luminosity galaxies ($M_B \lesssim -20$), which usually show a flat luminosity profile (core) at the same spatial scales (Côté et al. 2006, 2007). The mass fraction contributed by the central light excess is similar to the relative contribution of SMBH in giant galaxies, which could suggest a common formation path (Wehner & Harris 2006; Côté et al. 2006). The nature of these central light anomalies is

still uncertain since until recently their spatial scales were typically reachable only by HST imaging and in a few cases HST/STIS spectroscopy.

In this chapter we will present high spatial resolution two-dimensional maps of the velocity profile and the distribution of two near-IR spectral features in NGC 1399 – the central giant elliptical galaxy in the Fornax cluster ($M_B \lesssim -21.08$). This galaxy is known to harbour a SMBH (Saglia et al. 2000; Houghton et al. 2006; Gebhardt et al. 2007), weak nuclear activity (O'Connell et al. 2005) and shows a classical core in the luminosity profile (Lauer et al. 1995, 2005; Côté et al. 2007).

6.2 Observations and basic data reduction

6.2.1 Observations

NGC 1399 was observed on 5 October, 25 and 26 November 2004 as part of the SINFONI Science Verification program. Observing conditions were generally good with free-air optical seeing measurements ranging from 0.″4 to 0.″7, except in the night of October 5^{th}, where they reached 1″. The observations log is listed in Table 6.1.

To remove the night sky signature we used the standard near-IR technique, described in Section 2.4. We have consecutively taken object (O) and sky (S) frames. Our target was observed in five observing blocks (OBs) each containing a OSSOOSSO sequence (see Table 6.1). Each individual object pointing had two 300 s integrations, the sky pointings only one. The various on source pointings were dithered by 0.″05 to reject bad pixels and assure better spatial sampling. In the course of the data reduction we decided to exclude OB A, because of highly variable sky conditions resulting in a poor sky subtraction.

In order to improve upon natural seeing the observations were carried out using adaptive optics (AO) in natural guide star assisted mode. We used the same guide star (2MASS J03382914-3526442) as in the study of Houghton et al. (2006) which is located 17.″6 to the North of the galaxy centre. According to the SINFONI user manual, for best results the AO guide star should be sitting closer than 10″ from the object. In our case this was not possible, due to the lack of bright star in vicinity of the galaxy centre. Moreover the galaxy itself is not a good reference source, because of its flat central surface brightness profile. But even using this relatively distant star, we achieved reasonable AO correction, which is proved by the comparison of our SINFONI reconstructed luminosity profile with the one obtained with HST/NICMOS (see Figure 6.1)

Together with the science observations telluric standard stars were observed, as well as four velocity template stars covering the spectral range K4III to K7III (see Table 6.2).

Table 6.1: NGC 1399 observing log.

UT date (1)	t (s) (2)	O+S Frames (3)	Total t (s) (4)	OB ID (5)
2004 Oct 05	2x300	4+4	2400	A
2004 Nov 25	2x300	4+4	2400	B
2004 Nov 26	2x300	4+4	2400	C
2004 Nov 26	2x300	4+4	2400	D
2004 Nov 26	2x300	4+4	2400	E

Notes: (1) Date of observation, (2) exposure time per object pointing, (3) number of Object + Sky frames, (4) total on source exposure time per observing block, (5) observing block ID.

Table 6.2: List of velocity template stars.

Name (1)	spectral type (2)	Source (3)
HD 0005425	K4III	this work
HD 0025211	K4/5III	this work
BD -15 1319	K5III	this work
BD -16 1418	K7III	this work
2MASS J20411845+0016280	M0III	075.B-0495(A)
HD 0141665	M5III	075.B-0490(A)
2MASS J17093801-2718559	M5II-III	075.B-0490(A)

Notes: (1) star name, (2) spectral type, (3) origin of data.

6.2.2 Data reduction

To reduce this set of data we used the SINFONI Pipeline v. 1.6. The outline of the pipeline recipes and their output products we have discussed in Section 2.5. In summary, using the relevant pipeline recipes we obtained the necessary master flat fields, distortion, bad pixel and wavelength maps. Finally, for each data set contained in one galactic or calibration star OB the **sinfo_rec_jitter** recipe extracts the raw data, applies distortion, bad pixels and flat-field corrections, wavelength calibration and stores the combined sky-subtracted spectra in a 3-dimensional data cube. The **sinfo_rec_jitter** recipe also provides a one-dimensional spectrum extracted from an optimal aperture, which worked well for our star observations.

The accuracy of the wavelength calibration was checked by comparing the position of known sky OH emission lines, taken from the atlas of Rousselot et al. (2000), to the wavelength calibrated sky spectra. Where needed small shifts of up to one pixel (= 2.45 Å) were applied to our galaxy observations.

An important step towards improving our spatial resolution is the super sampling of the spaxels. This is possible since each resolution element is imaged over two pixels on the Hawaii2RG array and has a rectangular shape with dimensions of $0\farcs05 \times 0\farcs1$ on the sky. This means that if we dither the observations by half of a resolution element ($0\farcs05$) we will have final resolution elements with sizes $0\farcs05 \times 0\farcs05$. This means that the final amount of spectra is $64 \times 64 = 4096$ and the output FoV is slightly larger than $3'' \times 3''$. In fact, the outer regions of the FoV are not usable due to different defects on the Hawaii2RG array and worse sky correction. For this reason we have cut them and have a final useful FoV of $3'' \times 3''$. This approach has shown to work well, especially in the cases when resolving small scale structures is essential.

6.2.3 Telluric correction

Together with NGC 1399 we observed stars from solar spectral type, which exhibit a number of absorption features in the *K*-band. In order to remove the continuum shape and the spectral lines, typical for solar type stars, we divided the telluric star spectrum by a scaled and gaussian broadened, to match the resolution of our observations, solar spectrum. After that each telluric correction spectrum was shifted and scaled with respect to the science spectrum, for whose correction it will be used to minimise the residuals. To correct all the spectra in a given data cube we used one single telluric correction spectrum. We consider this is not a source of significant error, because the FoV of each data cube is rather small ($3'' \times 3''$) and we do not expect significant variations of the night sky. The last step was to divide each spectrum in the science data cubes by the so prepared telluric spectrum.

6.2.4 Data cubes combination and spatial binning

In order to achieve the best signal-to-noise ratio we combined four of the individual observing blocks (OB ID: B, C, D, E). We excluded OB A because of its poorer quality, resulting in additional noise. Before combining the OBs we identified the centre of the

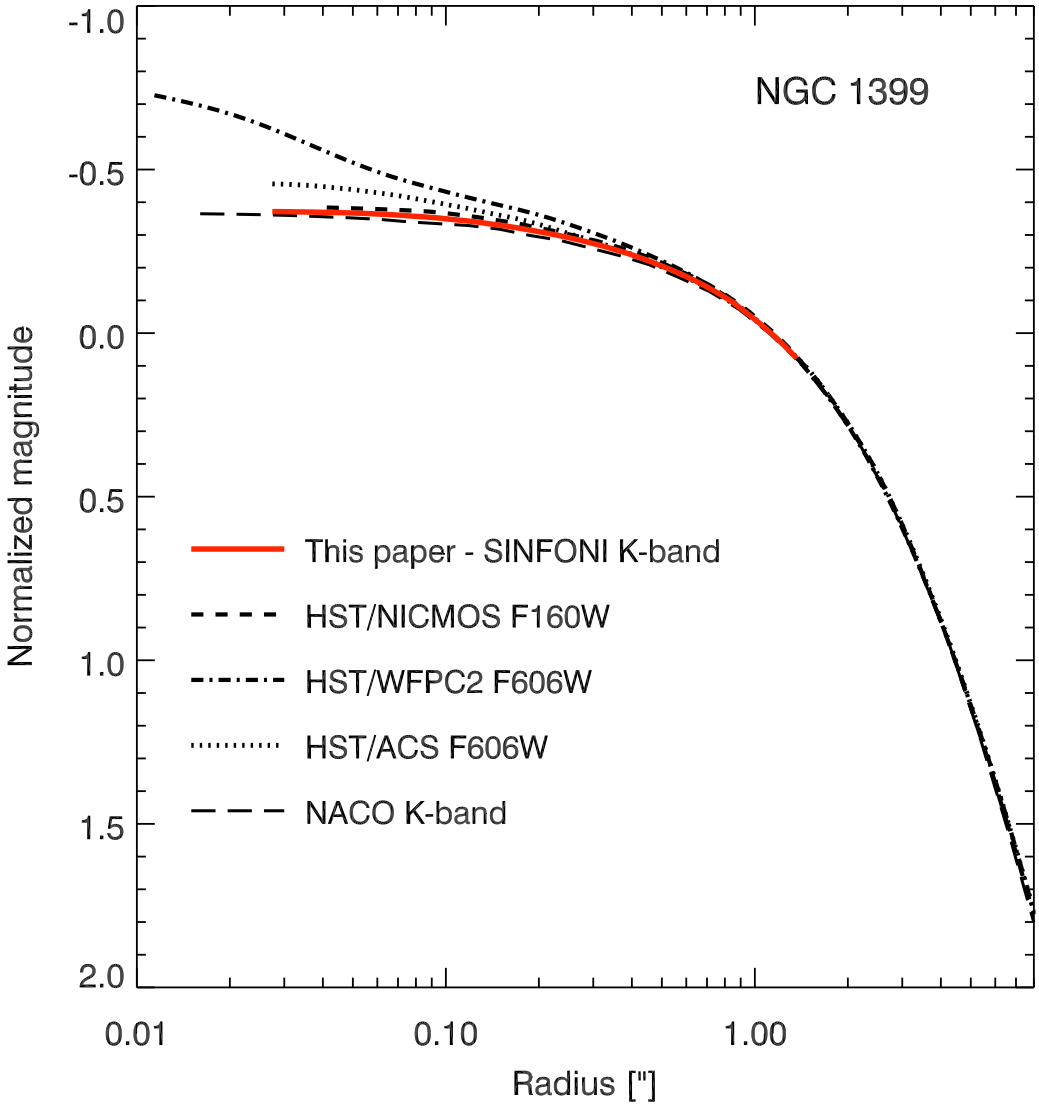

Figure 6.1: Normalised luminosity profile of NGC 1399 as reconstructed from our data cube (solid red line). As a comparison we show HST/NICMOS F160W (short dashed line) and HST/ACS F606W (dotted line) observations (retrieved from the HST Archive) as well as HST/WFPC2 F606W (dash-dot line) profile from Gebhardt et al. (2007) and a VLT/NACO *K*-band profile from Houghton (private communication, program 078.B-0806, PI Houghton) – long dashed line. Profiles are normalised in the region $1'' \leq r \leq 1\farcs4$. The WFPC2 light profile is super-sampled and deconvolved for the instrumental PSF which at least partly explains the differences between the WFPC2 and ACS data, obtained in the same filter (F606W).

galaxy in each data cube with an accuracy of one pixel (= 0.05″) and re-centred them. The final combination was performed using a sigma-clipping pixel reject algorithm.

The next step was to spatially bin the final data cube to a roughly constant signal-to-noise ratio which will allows us to measure reliable kinematics and line strengths. This was done using the adaptive binning method of Cappellari & Copin (2003). Using our velocity template stars we first performed Monte Carlo simulations to determine the minimum S/N needed to recover the higher order moments h_3 and h_4 of the line-of-sight velocity distribution (LOSVD) to a precision of about ± 0.04. This also means that the recession velocity and velocity dispersion can be recovered with an error of about ± 17 km s^{-1}. This accuracy is comparable with or better than what was achieved in previous studies, while we also preserve a good spatial resolution. For our data set and the spectral region 2.2 - 2.3 μm we found that a S/N of about 100 is needed. The resulting bins have a typical size of ∼ 0.″15 (5-6 spaxels combined) in the central regions, and approximately 0.″2 (>10 spaxels combined) for radii >1″. Bins which contain more than 30 spaxels (a few bins at the edges of the field of view) are excluded from the analysis, because of higher systematic effects, and are marked with black colour on the kinematical and line strength maps.

During the binning procedure we derive pseudo error spectra by determining the standard deviation at each wavelength. While this procedure is not fully correct since not all spaxels in a given bin are independent (e.g., seeing effects) it takes into account other error sources such as sky-subtraction and telluric correction residuals.

6.2.5 Effective spatial resolution

A key parameter to characterise our data is the effective spatial resolution, which was achieved in the combined data cubes before binning. Direct measurements of the effective point spread functions were not obtained during the nights of our observations, due to the tight constraints of the science verification run. Therefore, we estimate the effective seeing in two other ways.

We first compared the reconstructed and radially averaged luminosity profile of NGC 1399 from our data cube with the results from a HST/NICMOS image (GO 7453, PI Tonry; camera NIC2, sampled at 0.″0755 per pixel). We found that the two luminosity profiles agree very well even without any further broadening of the NICMOS data suggesting roughly similar PSF sizes with a FWHM ≃ 0.″17 (see Figure 6.1).

Secondly, we independently confirmed the above estimate from our own data cube by measuring the FWHM of a point source like object (presumably a globular cluster) located at about 1.″45 south-east from the NGC 1399 nucleus. Globular clusters at the distance of the Fornax cluster might be extended. However, here we assume it to be a point source and thus obtain a conservative estimate for the seeing. A simple Gaussian fit yields a FWHM = 0.″11, very much in agreement with the results from the comparison of the luminosity profiles.

We conclude that the effective spatial resolution of our NGC 1399 data can be described with having a FWHM of about 0.″15.

6.3 Kinematics

In this section we present our kinematical analysis of the central region of NGC 1399. Our *K*-band IFU spectroscopy is used to probe the velocity profile of the galaxy's centre to HST like spatial resolution.

6.3.1 Extraction of the kinematics and comparison with earlier studies

The extraction of the kinematical information from the final galaxy data cube was performed with the help of the Penalised Pixel-Fitting method (pPXF) developed by Cappellari & Emsellem (2004). The success of this method relies on the provision of a good set of template spectra, which match the galaxy spectra as well as possible. We found that the template stars observed in conjunction with the NGC 1399 observations (covering K4III to K7III) did not yield fully satisfactory fits and thus we searched the VLT/SINFONI archive for further template stars particularly covering later spectral types. We found three suitable stars with spectral type M0III, M5III and M5II-III. Fully reduced spectra were kindly provided by M. Cappellari (private communication). In our final analysis seven velocity template stars (see Table 6.2) were used in the fitting procedure to determine the recession velocity, velocity dispersion and the h_3 and h_4 Gauss-Hermit coefficients for each bin in the data cube.

The fitting was performed in the spectral range between 2.18 μm and 2.35 μm where several prominent absorption features allow fitting (see Figure 6.2). However, we excluded the region 2.20 μm– 2.22 μm (around the Na I feature), because none of the template stars was able to match the strength of the Na I absorption in NGC1399. This is not surprising, since Silva et al. (2008) showed that the Na I absorption strength is typically stronger in early-type galaxies compared with Galactic open cluster stars. In the fitting procedure typically only 3-4 stars were used to achieve a good fit over the full wavelength extent. The stars which received the highest weighting were of spectral type M0III and M5III.

We derive one-sigma error estimates from the pPXF code, based on our error spectra (see Section 6.2.4). The validity of our error spectra is confirmed since the reduced χ^2 values derived by the code were typically close to unity. Furthermore, we performed an empirical error estimation by assuming spherical symmetry in the galaxy and deriving the standard deviation for v, σ, h_3 and h_4 measurements in a ring of radius 0.″8 to 1″. The errors derived with this procedure agree well with the pPXF internal error estimates and are 17.2 km s^{-1}, 19.4 km s^{-1}, 0.03 and 0.05 for v, σ, h_3 and h_4, respectively.

The kinematics of NGC 1399 have been studied several times in the past using long-slit spectroscopy, mainly for the purpose of determining the mass of the super-massive black hole in its centre. Velocity dispersions as high as ~ 450 km s^{-1} make this galaxy an extreme and very interesting case in the σ-black hole mass relation (Ferrarese & Merritt 2000; Gebhardt et al. 2000).

Saglia et al. (2000) used ground based optical observations and reported little rotation (≤ 30 km s^{-1}) and compatibility with the presence of a central black hole of $M \approx 5 \times 10^8\,M_\odot$. Houghton et al. (2006) studied NGC 1399 with ground based adaptive

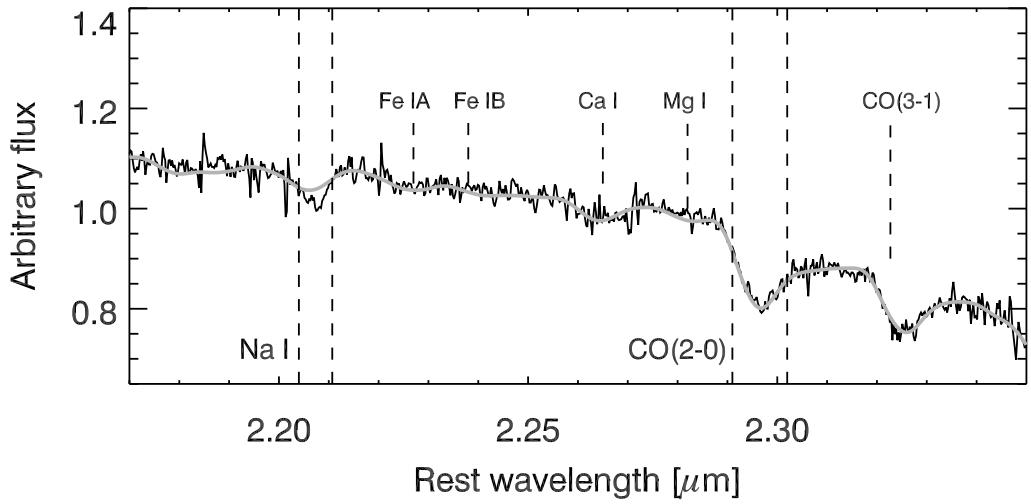

Figure 6.2: Normalised spectrum of NGC 1399 taken from the central bin of our data. The grey line shows the best fitting composite template as derived in our kinematics measurements. The vertical dashed lines show the extent of the central bandpass of the Na I and ^{12}CO (2–0) indices. The positions of several other absorption features are indicated.

optics assisted observations in the near-IR using the ESO VLT instrument NACO. Their analysis reveals a kinematically decoupled core and double-peaked velocity dispersion across the centre. The modelling requires a central black hole with $M \approx 1.2 \times 10^9\,M_\odot$ and a strongly tangentially biased orbit distribution. The most recent study is the one by Gebhardt et al. (2007). They analysed HST/WFPC2 optical imaging and HST/STIS spectroscopy in combination with the Saglia et al. (2000) data. They see a dramatic increase in the velocity dispersion at about 0.″5 on both sides of the galaxy and a central drop, which they interpret as tangentially biased orbital distribution. Their best fit model requires a black hole with mass $(5.1 \pm 0.7) \times 10^8\,M_\odot$.

In Figure 6.3 we show our kinematical measurements together with data from previous studies. We use radial plots for this first-order comparison, since the observations in the earlier studies were obtained with long-slits at different position angles (110° in Saglia et al. (2000), 117° in Gebhardt et al. (2007) and 5.06° in Houghton et al. (2006)). We plot data from the full two-dimensional region covered by our observations.

For radii $> 0.''3$ we find in general good agreement between our measurements and previously published results. However, we cannot confirm the large negative h_4 values seen by Houghton et al. (2006) although we also measure negative h_4 values at these radii. We also cannot confirm the velocity dispersion measurements of Gebhardt et al. (2007) for their two outermost data points.

For radii $< 0.''2$ our measurements appear to be between the measurements of Houghton et al. (2006) and Gebhardt et al. (2007). Although the studies do not agree

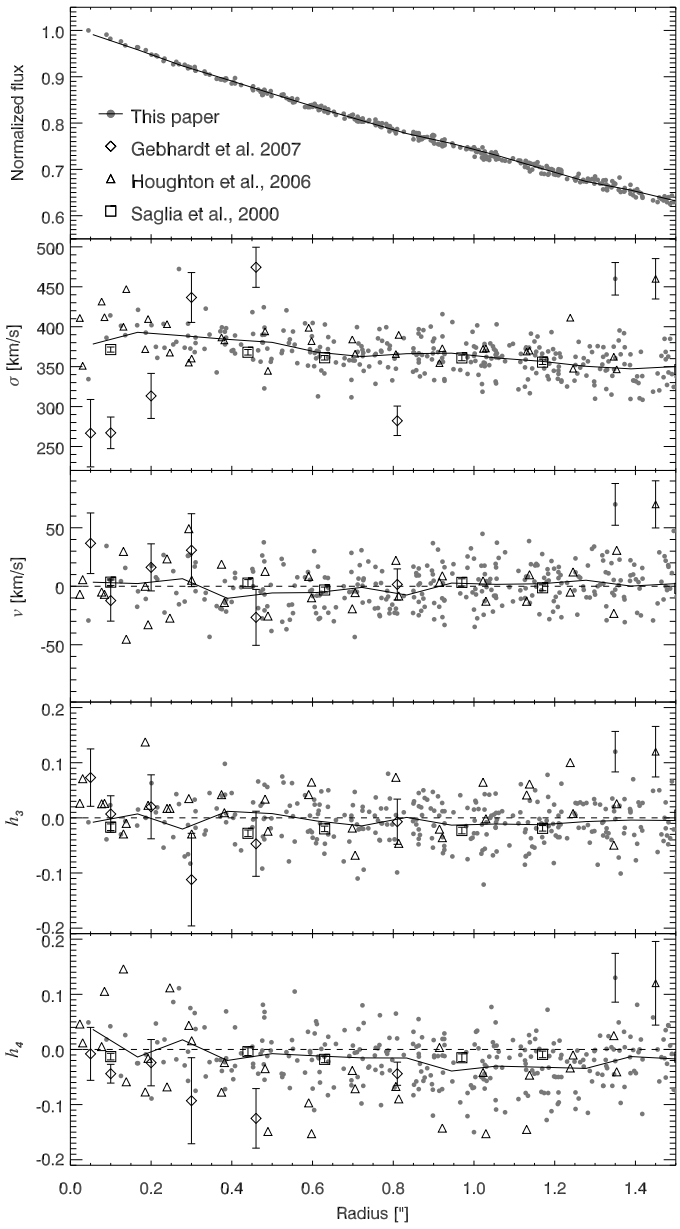

Figure 6.3: Light distribution and the first four moments of the velocity profile for NGC 1399. *Top panel*: Luminosity profile, as inferred from our SINFONI data. The solid line represents the mean luminosity in 0.″1 bins. *Bottom panels*: radial profile of the kinematics. SINFONI observations are marked with solid grey circles. Empirical error estimates (for details see Section 6.3.1) are shown with an error-bar and a solid symbol in the top-right corner of each plot. The solid line represents the mean value of each moment in 0.″1 bins. Results from earlier studies are shown with different symbols as explained on the top plot. Representative errors from Houghton et al. (2006) are shown with an error bar in the top-right corner of each panel with the triangle symbol. Errors from Saglia et al. (2000) and Gebhardt et al. (2007) are plotted with the data points.

well for the inner velocity dispersion gradient, all three of them show a pronounced drop in the very centre. In this comparison the HST/STIS data probably have the best spatial resolution ($\simeq 0\farcs05$; Gebhardt et al. (2007)), however, even accounting for seeing differences it is difficult to reconcile the data sets. Similarly, we cannot find any evidence in our data for the extreme, positive h_4 values seen in the Houghton et al. (2006) study.

6.3.2 Kinematical maps

Given that we have full two-dimensional kinematic maps, we can explore if there is a more complex kinematical structure in the centre of NGC 1399, which might explain the measurement differences reported above. In Figure 6.4 we present our maps of σ, v, h_3 and h_4. We also overplot the slit orientations and widths of Houghton et al. (2006) and Gebhardt et al. (2007) studies for better illustration. The Saglia et al. (2000) slit covers almost our full field of view, thus it is not shown in Figure 6.4

The velocity dispersion map shows rising values towards the centre with a distinct drop in the middle. However, the inner $\sim 0\farcs5$ appear to be asymmetric, and show three peaks to the north-east, south-east and west of the centre. Figure 6.4 shows that the Gebhardt et al. (2007) slit intersects two of the high-σ features, which can potentially explain the disagreement with Houghton et al. (2006), whose slit does not cover any of them. If confirmed, the velocity dispersion structures presented in this work may imply the need for more detailed dynamical modelling for the nuclear parts of the galaxy.

Our velocity map does not show any significant ordered motion within our errors ($\simeq$17 km s^{-1}). The h_3 map is consistent with a value of zero and thus no structure, while the h_4 map is mildly positive in the very centre and mostly negative for radii $> 0\farcs4$.

6.4 Near-IR line strength maps

In this section we discuss the two-dimensional distribution of two near-IR absorption features – Na I close to 2.2 μm and ^{12}CO (2–0) at 2.3 μm (see Figure 6.2), at a spatial resolution and scale only accessible by HST observations in the past. We used Frogel et al. (1990) index definitions, measured and calibrated the index values following the procedures, described in Sections 3.3 and 3.4. Using our error spectra we computed index errors via Monte Carlo simulations, where we took into account photon noise, recession velocity errors, and LOSVD correction errors. Following the procedure applied for the kinematics (see Section 6.3.1) we also derived empirical error estimates by computing the standard deviation of index values in a region with radius between $0\farcs8$ and $1''$. For the Na I index, the empirical estimate is 0.5 Å, and thus slightly higher than our internal estimate of 0.38 Å. For the ^{12}CO (2–0) index we find a much larger difference with an empirical error of 0.6 Å as compared to 0.17 Å for the internal value. Line strength indices can be very sensitive to continuum shape effects, especially if they cover large wavelength ranges as is the case for the ^{12}CO (2–0) index. We consider this

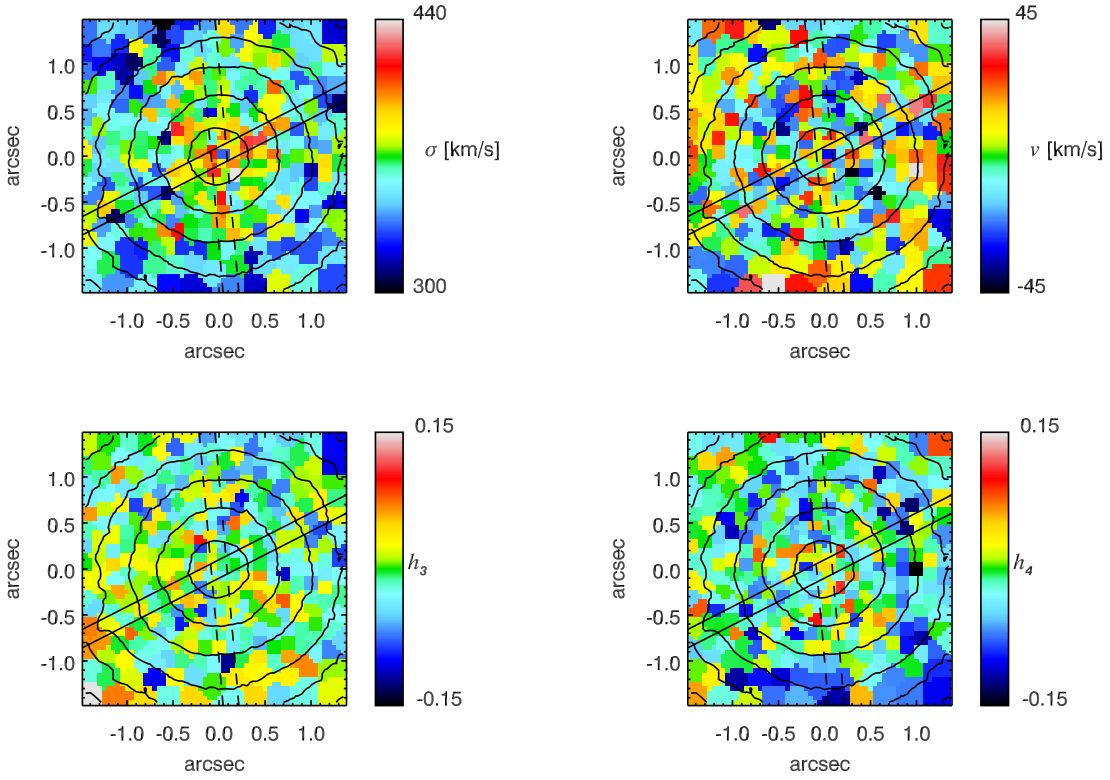

Figure 6.4: Maps of the first four moments of the velocity profile in the central 3″ of NGC 1399. *Top left* - velocity dispersion, *top right* - velocity. *Bottom left* - h_3 and *bottom right* - h_4. North is up, east - to the left. Slit orientation and width of the Gebhardt et al. (2007) study are shown with solid lines (PA = 117°, width = 0.″2), the slit of Houghton et al. (2006) is shown with dashed lines (PA = 5.06°, width = 0.″172). Overplotted are levels with constant surface brightness, as derived from our data.

is the main reason for increased errors (see also Silva et al. 2008). In the following we adopt the empirical error estimates in our analysis.

Silva et al. (2008) present a more complete set of spectral features in the *K*-band, including the Ca I and two Fe indices (see Figure 6.2). Here we will not discuss these additional, weak features, because our chosen S/N ratio per bin in combination with the very high velocity broadening of NGC 1399 makes them very difficult to measure.

In Figure 6.5 we show the distribution of Na I and ^{12}CO (2–0) over the central 3″×3″ of NGC 1399. In the central 0.″2 we see a well pronounced drop of about 1 Å and 1.5 Å in Na I and ^{12}CO (2–0), respectively. Below the maps we show the radial distribution of both indices for better illustration. The red line shows the median value of each index in 0.″1 wide bins. We note, that Houghton et al. (2006) also found some evidence for a central CO drop in their data, although their measurements were not conclusive. Outside the nuclear region we find evidence for line strength gradient in Na I. The index decreases with radius with a slope of -0.498 ± 0.087 within 0.″4 and 1.″4 (the Spearman correlation coefficient is -0.21 with a probability of 0.09% that there is no correlation). The linear fit to the data is overplotted in Figure 6.5. Using our calibration of the Na I index vs. metallicity from Chapter 5, equation 5.2, we measure a metallicity gradient $\Delta[Z/H]/log(r/r_e) = -0.19 \pm 0.06$. This gradient is shallower than the gradients measured at larger radii in other Fornax cluster early-type galaxies. For example Kuntschner (1998) measure an average metallicity gradient of -0.48 ± 0.19, based on the [Mg/Fe]′ index, for the elliptical galaxies in their sample.

We do not find a significant line strength gradient of the ^{12}CO (2–0) index over the observed radial range. We also measured the strength of ^{12}CO (2–0) using the D_{CO} index definition of Mármol-Queraltó et al. (2008) to check weather the ^{12}CO (2–0) line strength drop still persists. Our D_{CO} index map is shown in Figure 6.6, together with the radial profile for this index. Our internal error estimate of 0.003 is roughly consistent with the empirical error estimate of 0.005. In Figure 6.6 we give the empirical error. The drop in ^{12}CO (2–0) line strength is evident also when using a different index definition, which is less sensitive to the continuum shape. Thus our conclusions about its existence are stronger.

6.5 Discussion on the central velocity dispersion and line strength drops

In this section we will discuss the significance of the central σ and line strength drops we described in Sections 6.3.2 and 6.4 and explore a few possible scenarios that could explain their origin.

6.5.1 Technical aspects

Firstly, we investigate the statistical significance of the central drops in absorption strength of the Na I and ^{12}CO (2–0) indices. Using a two-dimensional Kolmogorov-Smirnov test we can reject the null-hypothesis that the innermost five data points ($r < 0.''15$) are drawn from the same distribution as the data points between 0.″3 and

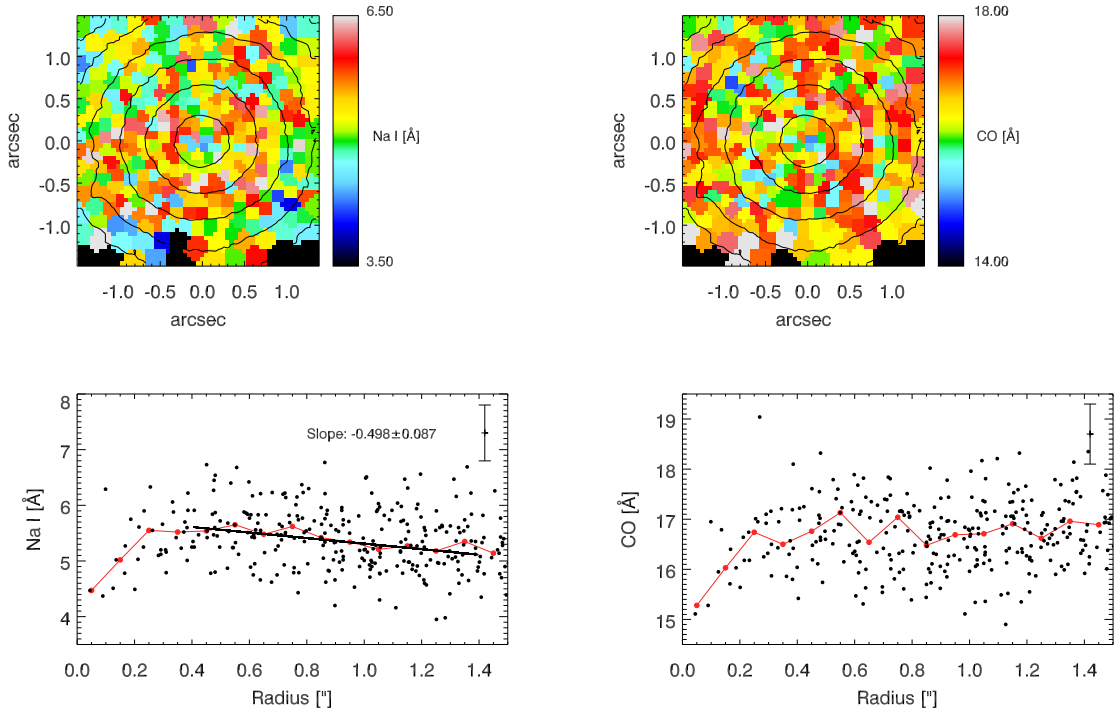

Figure 6.5: *Top panels*: Maps of Na I and ^{12}CO (2–0) in the central 3″of NGC 1399. Overplotted are levels with constant surface brightness, as derived from our data. *Bottom panels*: Radial distribution of the same indices. The red lines represent the median index values in 0.″1 bins. The black line shows a linear fit to the index values of Na I in the region $0.''4 < r < 1.''4$. The slope value is given in the plot. Typical index errors (see Section 6.4) are shown with error bars in the upper right corner of the plots.

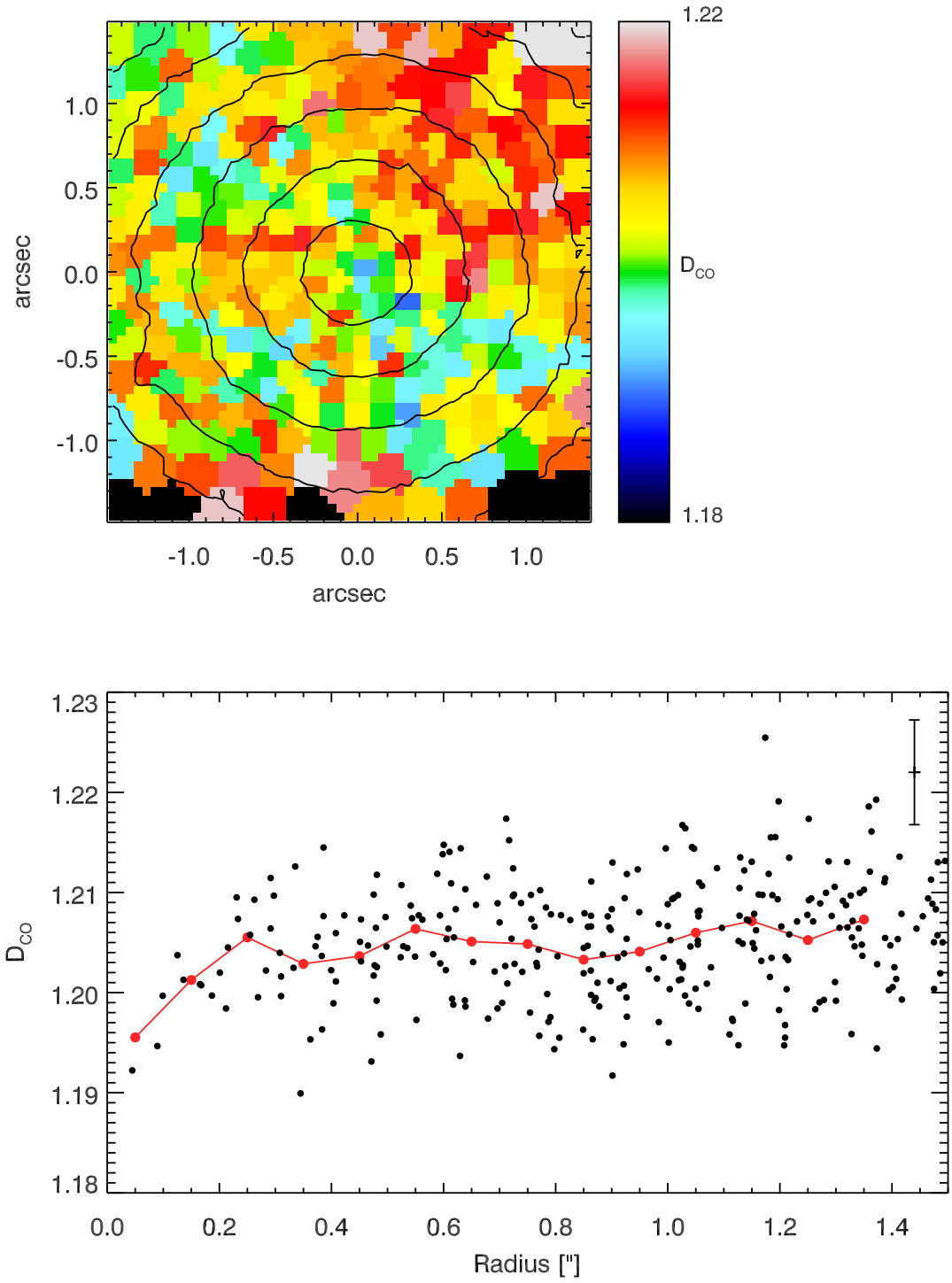

Figure 6.6: *Top panel*: Map of the D_{CO} index in the central 3″of NGC 1399. Overplotted are levels with constant surface brightness, as derived from our data. *Bottom panel*: Radial distribution of the same index. The red line represents the median index values in 0.″1 bins. Typical index error (see Section 6.4) is shown with error bar in the upper right corner of the plot.

1″ with a significance level of 3.4% and 0.4% for the Na I and ^{12}CO (2–0) indices, respectively. While for the Na I index the significance is only marginal, both index drops taken together are believable. Another test we performed is to fit a simple two component model, where we fit the data with two linear functions with a break radius at $r = 0\farcs25$. The steep slopes measured for the central component are different from zero at four and nine sigma level for the Na I and ^{12}CO (2–0) indices, respectively.

Secondly, we explore the possibility that the line strength drops could be caused by wrong kinematics (e.g., too low velocity dispersion) which would lead to wrong (e.g., too low) LOSVD corrections. Due to the large velocity broadening seen in the centre of NGC 1399 we have to apply significant LOSVD corrections (see Section 3.4). However, even if we assume the extreme case of a LOSVD ($\sigma = 370\,\mathrm{km\,s^{-1}}$, $h_3 = 0.0$ and $h_4 = 0.0$) constant with radius we still find highly significant drops for both indices.

In summary we find that the line strength drops are significant at least at the 3-σ level and are unlikely to be produced by technical/calibration problems or by a chance statistical effect. Furthermore the observed features in the velocity dispersion and line strengths are present also when one performs the same analysis with the individual data cubes before combination, although the noise level raises.

6.5.2 Astrophysical explanations

Central velocity dispersion drops have so far been observed mainly in spiral galaxies (e.g. Bottema & Gerritsen 1997; Emsellem et al. 2001; Márquez et al. 2003; Falcón-Barroso et al. 2006). σ-drops have also been found in a few early type galaxies (e.g. Graham et al. 1998; Simien & Prugniel 2002; Pinkney et al. 2003; Emsellem et al. 2004). For spiral galaxies Wozniak et al. (2003) suggested that these σ-drops are the result of gas accretion followed by star formation and are therefore indicative of a recent in-fall of dissipative material. In a follow up study Wozniak & Champavert (2006) showed that the life time of such σ-drops can be long (≥ 1 Gyr), however this requires continuous star formation in the nuclear region at least on a level of $1\,M_{\odot}\,yr^{-1}$. Without continued star-formation, the amplitude of the σ-drops decreases rapidly.

Velocity dispersion drops were found in about half of the sample of spiral galaxies, studied by Peletier et al. (2007). Their stellar populations analysis, however, shows that the ages of these inner components are not significantly younger than the centres of spiral galaxies without σ-drops as would be expected from the above scenario. This may indicate that the central, dynamically cold components can be more long lived.

Typically the observed σ-drops in spiral galaxies have spatial scales of a few hundreds parsecs. For NGC 1399 such a large scale σ-drop is not observed (Graham et al. 1998). The σ-drop we observe in NGC 1399 has a diameter of only ~30 pc (corresponding to $0\farcs3$). Similar size σ-drops have been seen with HST/STIS spectroscopy in the elliptical galaxies NGC 4649 and NGC 4697 by Pinkney et al. (2003) and in the post-merger NGC 1316 (Fornax A) with VLT/SINFONI by Nowak et al. (2008), indicating that these small scale drops may be a more wide spread phenomenon in early-type galaxies.

On the basis of their dynamical modelling Gebhardt et al. (2007) state that NGC 1399 possesses extremely tangentially biased orbital distribution for radii between $0\farcs1$ and

0.″5 which is responsible for the σ-drop, consistent with the findings of Houghton et al. (2006). Both studies explore various possibilities for the progenitor of these extreme orbits, ranging from nuclear activity, an eccentric disc, a torus to a stellar cluster having fallen in on a purely radial orbit.

We can empirically test the hypothesis for the presence of a low velocity dispersion subsystem in the nucleus of NGC 1399 causing the σ-drop. We performed simple simulations by combining an averaged galaxy spectrum taken at radii between 0.″2 and 0.″3 ($\sigma \sim 400\,\mathrm{km\,s^{-1}}$) with a velocity template star, broadened to velocity dispersions from 15 to 150 km s^{-1} and a range of luminosity weightings. We can reproduce our measurements for the inner 0.″15 of NGC 1399 ($\sigma < 360\,\mathrm{km\,s^{-1}}$ and positive h_4) with ~15% of the light originating from a central stellar subsystem with σ up to 100 km s^{-1}. Using the surface brightness profile of NGC 1399 (e.g. from Gebhardt et al. 2007) we can estimate the surface brightness of such a subsystem. We find that a central, low velocity dispersion ($\sigma \leq 100\,\mathrm{km\,s^{-1}}$) stellar subsystem with $V \simeq 20.3^m$ is able to explain the central drop in velocity dispersion for NGC 1399. Such a *V*-band luminosity is comparable to the brightest globular clusters in NGC 1399 or bright nuclei of dwarf galaxies in the Fornax cluster (e.g. Dirsch et al. 2003; Mieske et al. 2006).

If such a subsystem is present in the nucleus, we can expect that it will not have the same stellar population properties as the underlying galaxy since it might have been formed on different time scales, under different physical conditions or in a different environment. Thus we can expect that it will have some influence on the line strengths in the same region. Indeed, as shown in Section 6.4, we find line strength changes with the same extent as the σ-drop. Nevertheless, index changes might be due to different reasons than stellar population effects. A plausible explanation for the reduced line strengths of Na I and ^{12}CO (2–0) in the central regions could be the presence of nuclear activity causing the continuum level to be raised. Oliva et al. (1999) show that the nuclear continuum in the near-IR spectral domain in galaxies with active galactic nuclei (AGN) is mainly due to reprocessed radiation, coming from the AGN UV-continuum heated dust. This radiation has a black body spectrum with temperatures typically between 100 and 1000 K. O'Connell et al. (2005) report an ultraviolet light outburst in the nucleus of NGC 1399 with a maximal far-UV luminosity of 1.2×10^{39} erg s^{-1} reached in January 1999. Thus they claim NGC 1399 to harbour a low-luminosity active galactic nucleus (LLAGN). We tested this hypothesis by subtracting black body spectra with different temperatures in the above mentioned range from our innermost spectra with the goal to match the line strengths seen at radii > 0.″2. The results from this test were unfavourable for a scenario in which the LLAGN induced non-stellar continuum causes the observed line strength changes, since we were unable to model the index changes for both Na I and ^{12}CO (2–0) simultaneously with one single black body spectrum of a given temperature. We can go even further and force the indices to drop by the right amount by subtracting a continuum with a very steep slope (in comparison with the already mentioned black body spectra). However, when we use this steeper slope to match the index drops, the effective velocity dispersion measured from such a spectrum ($\sigma = 384\,\mathrm{km\,s^{-1}}$) does not agree well with our results from Section 6.3.1. Moreover, the resulting spectrum does not resemble the observed central galaxy spectrum (i.e. different continuum shape and slope), which it is sup-

posed to model. Therefore, we conclude that the presence of an AGN-like continuum is not very likely to be the reason for the central line strength and velocity dispersion changes observed in NGC 1399.

Coming back to the stellar population issue it is very interesting to note that the Gebhardt et al. (2007) imaging data of NGC 1399 (HST/WFPC2 PC chip) show a blue nucleus ($r \leq 0\farcs1$) with weak evidence for a central light excess at the same radii (see Figure 6.1). Their $(B - V)$ colour drops by about 0.1 mag in comparison with the surrounding region, which appears to be constant in colour (their Figure 1, bottom panel). Recent HST/ACS observations of NGC 1399 in g and z bands (Jordán et al. 2007; Côté et al. 2007, ACS Fornax Cluster Survey, also Andrés Jordán, private communication) show very weak evidence for a central light excess and also very mild evidence for a bluer colour, but exhibit prominent PA and ellipticity changes within $r \leq 0\farcs2$ consistent with the HST/WFPC2 data. We note, that the core region of NGC 1399 with a break radius of about 2″ (see Figure 6.1) is much larger than the scales discussed here.

The information from the imaging, combined with the observed σ and line strength drops at similar radii provide good evidence for the scenario of a central dynamically cold stellar subsystem with different stellar populations as compared to the surrounding galaxy.

6.6 Comparison with stellar population models

Until more detailed stellar population models in the near-IR become available we can only perform a limited stellar population analysis by using the empirical relations found in the Silva et al. (2008) study, our own work on globular clusters (GCs) in the LMC (Chapter 4), and early-type galaxies in the Fornax cluster and low density environments (Chapter 5). In Figure 6.7 we show the value of the Na I and D_{CO} index (top and bottom panel, respectively) in the outer regions ($r > 0.2''$) of NGC 1399 with a filled square symbol. The age was derived from an optical age-metallicity diagnostic diagram (see Figure 5.2). With a straight horizontal line we show the values of these two indices in the centre of NGC 1399 ($r < 0\farcs15$) and with the horizontal dashed lines we show their 1σ error. The choice of showing the central values with straight lines, spanning the full age range is due to our inability to estimate the age of the central subsystem. Our calibration of the Na I index in terms of metallicity from old Fornax galaxies is indicated with and arrow. The grey shaded regions indicate the loci of Na I and D_{CO} index values in these galaxies. The filled circles denote the three Fornax galaxies with signatures of recent star formation. The blue shaded regions show the loci of Na I and D_{CO} index values in LMC GCs (the metallicities are indicated inside the regions). For Fornax cluster early-type galaxies with old stellar populations Silva et al. (2008) found a good linear correlation between the Na I index and the optical metallicity indicator [MgFe]′ as well as ^{12}CO (2–0) and [MgFe]′. We have supported this finding in Chapter 5 with additional data and also argued that the Na I index correlates well with the metallicity at old ages. However, it also reacts to the presence of young stars and in a more linear way, than the D_{CO} index.

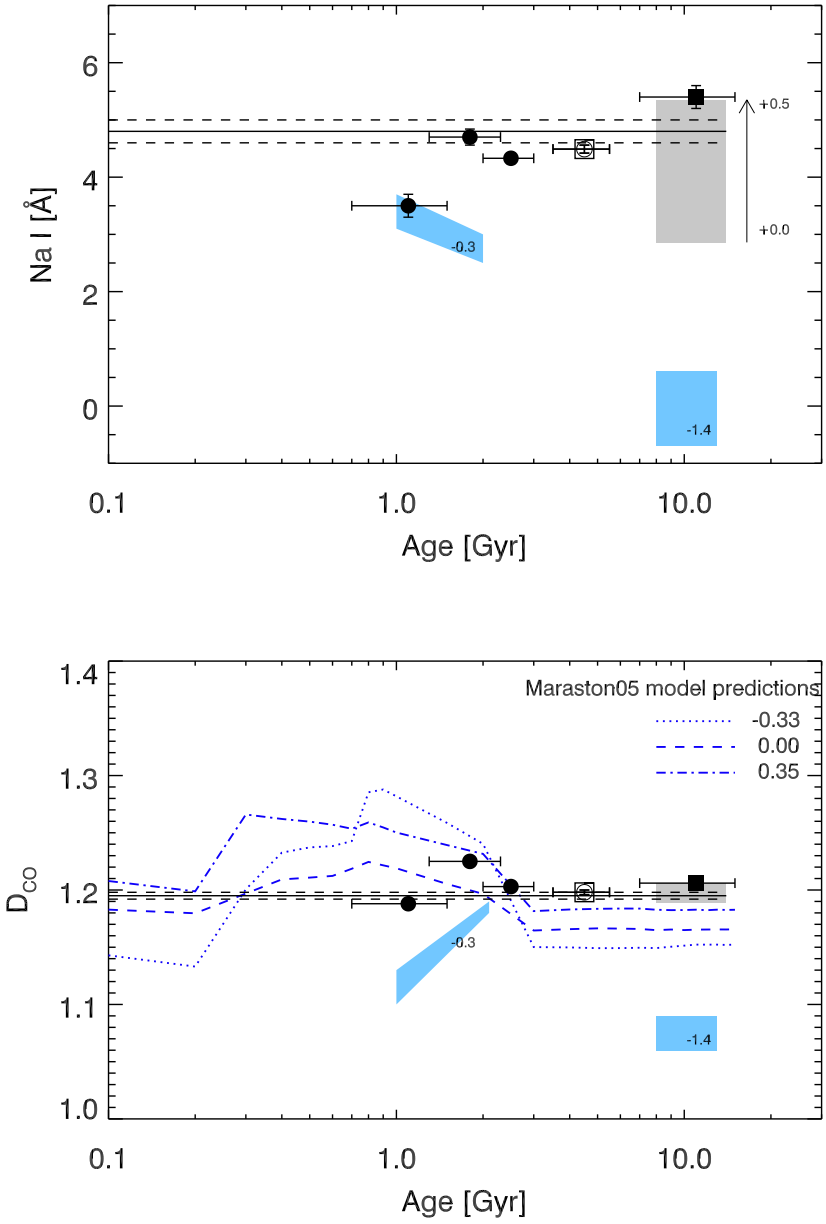

Figure 6.7: *Top panel*: Na I index as a function of age and metallicity. The filled symbols represent the three galaxies in the Fornax cluster with luminosity weighted ages of <3 Gyr from Chapter 5. The open square symbol denotes the intermediate age galaxy (NGC 1380). The grey shaded region indicates the locus of the old Fornax cluster galaxies. Our metallicity calibration of this index is shown with and arrow. With blue shaded regions are indicated the loci of LMC globular clusters from Chapter 4 (metallicity is indicated in the regions). The filled square denotes the outer regions of NGC 1399, the horizontal line stands for the central region of NGC 1399. *Bottom panel*: The same as above, but for the D_{CO} index. The blue lines give the SSP model predictions of Maraston (2005) for metallicities given in the panel.

The first possible explanation for the decrease of Na I and D_{CO} index in the centre of NGC 1399 is a drop in metallicity only. The hypothesis of a younger age only can be ruled out, because the Na I index then is expected to increase and not decrease. However, a combination of the two scenarios is also possible. Younger and more metal poor subsystem will have a lower Na I and D_{CO} index. The final index values will strongly depend on the relative contributions from the old and metal rich body of the galaxy and the younger and metal poor subsystem.

Alternatively, one can consider – in addition to a drop in metallicity, abundance ratio differences between the main body of NGC 1399 and the proposed central stellar subsystem, which would explain the relative changes of D_{CO} and Na I. While a combination of metallicity, age and abundance ratio changes are an attractive explanation for the observed line strength maps, a confirmation of the above scenarios clearly awaits the more detailed predictions of stellar population models.

6.7 Conclusions

In this chapter we presented for the first time high spatial resolution *K*-band maps for the kinematical and near-IR spectral properties of the centre of the giant cD galaxy in the Fornax cluster, NGC 1399. We confirm the presence of a central velocity dispersion dip within $r \leq 0\farcs2$ previously seen in the long-slit studies of Houghton et al. (2006) and Gebhardt et al. (2007). Our velocity dispersion map gives evidence for a non-symmetric structure towards the centre by showing three σ peaks to the north-east, south-east and west of the galaxy centre. Such a complex structure in the velocity dispersion has not been seen earlier in other early-type galaxies. The west – south-east peaks seem to be symmetric about the galaxy centre, while the north-east peak is essentially off-centred, nevertheless within our error analysis we consider it to be real. We note that the nuclear region of NGC 1399 does not seem to be obscured by dust (A. Jordán, private communication).

Additionally we measure two near-IR line strength indices at unprecedented spatial resolution. The most important features we observe in our 2-dimensional line strength maps are drops in Na I and D_{CO} line strength in the nuclear region of the galaxy, coinciding spatially with the drop in σ.

As an explanation for the line strength and velocity dispersion drops observed in the central region we discuss a scenario where NGC 1399 harbours a dynamically cold subsystem with a distinct stellar population. Dynamically this can be realised by a central stellar disc or a globular cluster (even a dwarf galaxy) having fallen into the centre of NGC 1399 on a purely radial orbit (Gebhardt et al. 2007). The near-IR index changes observed in our data suggest that the spectral properties of this subsystem are directed by some mixture of metallicity and age (and possibly abundance ratios) effects. Based on our results from Chapters 4 and 5 and the observed drop in Na I strength we can exclude a scenario of young age and constant metallicity. More precise constraints on the nature of the stellar population within this cold component awaits more detailed stellar population models. Similar line strength drops are observed also by Davidge et al. (2008) in a sample of nearby compact elliptical galaxies, suggesting

that they may be a more common phenomenon. We also observe a negative metallicity gradient for radii between 0.″4 and 1.″4, which is shallower than the averaged gradients at larger radii, measured in other early-type galaxies in the Fornax cluster.

Chapter 7

Summary

In this thesis we have studied the near-IR spectral properties of six globular clusters (GCs) in the Large Magellanic Cloud (LMC) and 21 early-type galaxies in the local Universe – 10 in low density environments and 11 in the Fornax cluster of galaxies. Our observations were acquired using integral field unit (IFU) and long-slit spectrographs. The common goal of the various projects was to provide the first spectral library of the integrated near-IR light of globular clusters with ages ≥ 1 Gyr and to verify the predictions of current stellar population models in the near-IR using GCs and early-type galaxies data.

7.1 Towards calibrating stellar population models in the near-IR

In Chapter 4 we have presented a pilot study of the GC population of the LMC, which provides us with a unique laboratory for the calibration and testing of SSP models at sub-solar metallicity. The relative remoteness of our targets, as compared to Milky Way globular clusters, offers a good balance between the availability of detailed information on the chemical composition and age via resolved stars studies, and the possibility to obtain integrated spectra with current instrumentation.

Using VLT/SINFONI we have obtained integrated, luminosity weighted spectra of six GCs in the LMC. Half of them represent the old (≥ 10 Gyr) and metal poor ([Z/H] $\sim$ –1.4) population in this galaxy, the other half represent the intermediate age ($1 <$ age < 3 Gyr) and more metal rich ([Z/H] $\sim$ –0.4) GC population. We have measured a number of spectral indices in the near-IR K-band – Na I, Ca I and D_{CO}, and compared the predictions of the stellar population models of Maraston (2005) with our observed D_{CO} line strength. Our conclusions are as follow:

- Literature photometric data of the integrated colours of the GCs in our sample agree very well with the model predictions for $(J - K)$ and $(H - K)$ colours.
- For old and metal poor GCs, model predictions for the D_{CO} index roughly agree with the observed values.

- For the intermediate age and half solar metallicity population the models predict an increase of the value of the D_{CO} index, which is consistent with the increased contribution by AGB stars at these ages. The D_{CO} index in our GC with an age of $\sim$2 Gyr agrees qualitatively with the model predictions for this index.

- Continuing to younger ages the models predict a maximum of the D_{CO} index at $\sim$1 Gyr. The two clusters in our sample, that have this age, show a reversed trend, i.e. instead of increasing, the D_{CO} index decreases. We find that this is due to the presence of carbon-rich AGB stars, which can contribute up to 60 % to the total K-band cluster light. The C-type stars have a weaker D_{CO} index, as compared to oxygen-rich (M-type) AGB stars. This difference is not due to a significant change of the strength of the ^{12}CO (2–0) feature, but to the appearance of many other absorption features, like C_2, CN and CH, in the spectral regions of C-type stars, where we estimate the continuum level needed to measure the D_{CO} index. This makes the index, as we measure it, weaker.

- We find differences in the D_{CO} index between the values, measured from the C-type stars in our LMC sample, and the Milky Way C-type stars from the library of Lançon & Mouhcine (2002), used to empirically include carbon star spectra in the models of Maraston (2005). For a given $(J-K)$ colour Milky Way carbon stars have a higher D_{CO} index, as compared to the LMC carbon stars. We consider this is due to the different metallicities of the two samples, however other reasons might also exist. A larger, more complete near-IR library of carbon stars covering a range of metallicities and colours is urgently needed to improve the model predictions.

- The near-IR Na I index appears to increase monotonically with increasing metallicity and decreasing age of the globular clusters. The Ca I index is very weak, however we find evidence that it correlates with the D_{CO} index and shows a similar dependence on the age at a given metallicity.

In Chapter 5 we have studied the central near-IR spectral properties of a sample of early-type galaxies in low density environments and compared them with early-type galaxies in the Fornax cluster, using long-slit spectroscopy. Within this project we have used our calibration of the near-IR Na I and D_{CO} indices from Chapter 4 and investigated their behaviour in the super-solar metallicity regime. Our main results are:

- For old galaxies we find that the Na I and D_{CO} indices correlate well with the central velocity dispersion, similar to the well known index–σ relations in the optical. Galaxies with optical signatures of a younger population (i.e. strong Hβ) clearly deviate from the main near-IR index-σ relations for old galaxies.

- For old galaxies the near-IR Na I index shows a very good correlation with metallicity as inferred from optical indices. The D_{CO} index follows the same trend, however with a shallower slope.

- The Na I and D_{CO} index react to the presence of young stars. However, the D_{CO} index has a more complex behaviour: it first increases with increasing age for a given metallicity, but then for the youngest galaxies in our sample it decreases, which is consistent with our observations of LMC GCs. The Na I index steadily increases with the age at a given metallicity, which is the opposite of what is observed in optical metallicity indicators.
- The near-IR spectral indices are mainly influenced by one single component of the stellar populations – cool giant stars, which means that they can be as good as the optical indices, if not even better, in resolving some of the current age-metallicity degeneracies. We suggest that a diagnostic diagram, based on the optical Hβ index, which is considered to be a good age indicator, and the near-IR Na I index, which we showed here to correlate well with the metallicity, is going to provide good estimates of the luminosity weighted age and metallicity of the unresolved stellar populations in early-type galaxies, once more detailed stellar population models in the near-IR become available.

7.2 The centre of NGC 1399: kinematically and chemically distinct

The IFU spectroscopy technique allows us to simultaneously obtain information of the full 2-dimensional kinematics and stellar population properties in nearby early-type galaxies. When coupled with adaptive optics, this method can lead to a spatial resolution only accessible to the *HST* in the past. In Chapter 6 we present our observations of the giant cD galaxy in the Fornax cluster, NGC 1399, with VLT/SINFONI in adaptive optics assisted mode. We used our *K*-band spectroscopy to probe the kinematics and the stellar populations within the sphere of influence of the super massive black hole, found in its nucleus. The effective spatial resolution of our data is $\sim 0\farcs15$ ($FWHM$). Our results are as follows:

- We confirm the presence of a central velocity dispersion drop within $r \leq 0\farcs2$ seen in previous long-slit studies by Houghton et al. (2006) and Gebhardt et al. (2007).
- Our velocity dispersion map gives evidence for a non-symmetric structure in this central area by showing three σ peaks to the north-east, south-east and west of the galaxy centre.
- We observe drops in the strength of two near-IR features – Na I and ^{12}CO (2–0), which have the same location and extent as the σ drop.
- The observed line strengths and velocity dispersion changes suggest a scenario where the centre of NGC 1399 harbours a dynamically cold subsystem with a distinct stellar population. The subsystem's properties are directed by either a combination of a younger age and lower metallicity, as compared to the main body of the galaxy, or lower metallicity only. We note that our data are not consistent with an AGN induced change in the spectra.

- We also observe a negative gradient of the Na I index over the central $3'' \times 3''$ of NGC 1399. Following our calibration of the metallicity as a function of the Na I index in Chapter 5 we measure a metallicity gradient, which is smaller than the averaged metallicity gradients observed at larger radii in other early-type galaxies in the Fornax cluster.

7.3 Future work

The accessibility to the near-IR spectral properties of early-type galaxies has opened up a new window to the exploration of their formation and evolutionary history. The use of near-IR spectral indices gives promising first results in solving the age-metallicity degeneracies, through the identification of the Na I index to be mainly metallicity driven.

In order to explore fully the near-IR spectral properties of the globular clusters in the LMC we plan to extend our *K*-band light study to the *J* and *H*-bands, where other interesting spectral features reside. The data have been already acquired and data reduction and analysis will start soon.

Furthermore, we plan to extend our spectral library of integrated, luminosity weighted spectra of LMC globular clusters by including spectra of objects with younger ages, where the contribution from AGB stars is even higher than in the clusters, studied in this thesis. The inclusion of spectra of GCs with different metallicities and ages will greatly improve the calibration of stellar population models. A potential source of such GCs are nearby galaxy merger remnants, where a significant secondary star formation has occurred (e.g. NGC 7252 or NGC 5128). A proposal has been submitted, waiting for evaluation.

The ultimate spatial resolution one may achieve when using adaptive optics in the near-IR is offering new insights into the dichotomy between early-type galaxies with flat luminosity profiles and those with central light excess. Recently it has been proposed that the light excess is due to nuclear star clusters (e.g. Côté et al. 2006), which mass scales with the central velocity dispersion of the host galaxy in a similar way as the M_{BH}-σ relation, suggesting a similar formation path (e.g. Ferrarese et al. 2006; Wehner & Harris 2006). Currently we are exploring the central parts of a low surface brightness elliptical galaxy in the Fornax cluster, which is suggested to harbour a nuclear star cluster. The preliminary results from our adaptive optics assisted IFU observations reveal a clear rotation of the cluster and enhanced near-IR line strengths as compared to the main body of the galaxy.

Small scale velocity dispersion and/or line strength drops, similar to the one we observed in NGC 1399, have been seen in other early-type galaxies (e.g. Pinkney et al. 2003; Davidge et al. 2008; Nowak et al. 2008), posing the question how common are such phenomena in the nearby Universe. We plan to explore this issue using adaptive optics assisted near-IR IFU observations. Natural targets are the galaxies, which already have been identified as having small scale velocity dispersion drops.

Bibliography

Alves, D. R. 2004, New Astronomy Review, 48, 659

Anderson, A. J. 1997, PhD thesis, University of California, Berkeley

Bacon, R., Copin, Y., Monnet, G., et al. 2001, MNRAS, 326, 23

Barnes, J. E. 1992, ApJ, 393, 484

Barnes, J. E. & Hernquist, L. E. 1991, ApJ, 370, L65

Beasley, M. A., Hoyle, F., & Sharples, R. M. 2002, MNRAS, 336, 168

Bedin, L. R., Piotto, G., Anderson, J., et al. 2004, ApJ, 605, L125

Bekki, K. & Chiba, M. 2005, MNRAS, 356, 680

Bender, R., Burstein, D., & Faber, S. M. 1993, ApJ, 411, 153

Bender, R., Surma, P., Doebereiner, S., Moellenhoff, C., & Madejsky, R. 1989, A&A, 217, 35

Bernardi, M., Alonso, M. V., da Costa, L. N., et al. 2002, AJ, 123, 2159

Bertelli, G., Nasi, E., Girardi, L., et al. 2003, AJ, 125, 770

Bessell, M. S. & Brett, J. M. 1988, PASP, 100, 1134

Bica, E., Claria, J. J., Dottori, H., Santos, Jr., J. F. C., & Piatti, A. E. 1996, ApJS, 102, 57

Bica, E. L. D., Schmitt, H. R., Dutra, C. M., & Oliveira, H. L. 1999, AJ, 117, 238

Blanco, V. M. & McCarthy, M. F. 1983, AJ, 88, 1442

Bonnet, H., Abuter, R., Baker, A., et al. 2004, in The ESO Messenger, Vol. 117

Bottema, R. & Gerritsen, J. P. E. 1997, MNRAS, 290, 585

Bower, R. G., Benson, A. J., Malbon, R., et al. 2006, MNRAS, 370, 645

Brott, I. & Hauschildt, P. H. 2005, in ESA Special Publication, Vol. 576, The Three-Dimensional Universe with Gaia, ed. C. Turon, K. S. O'Flaherty, & M. A. C. Perryman, 565

Bruzual, A. G. & Charlot, S. 1993, ApJ, 405, 538

Bruzual, G. & Charlot, S. 2003, MNRAS, 344, 1000

Burstein, D., Davies, R. L., Dressler, A., et al. 1988, in Towards Understanding Galaxies at Large Redshift, 17–21

Burstein, D., Faber, S. M., Gaskell, C. M., & Krumm, N. 1984, ApJ, 287, 586

Buta, R. J. & McCall, M. L. 1999, ApJS, 124, 33

Buzzoni, A. 1989, ApJS, 71, 817

Cappellari, M., Bacon, R., Bureau, M., et al. 2006, MNRAS, 366, 1126

Cappellari, M. & Copin, Y. 2003, MNRAS, 342, 345

Cappellari, M. & Emsellem, E. 2004, PASP, 116, 138

Carlberg, R. G. 1984, ApJ, 286, 403

Carollo, C. M., Danziger, I. J., & Buson, L. 1993, MNRAS, 265, 553

Carrera, R., Gallart, C., Hardy, E., Aparicio, A., & Zinn, R. 2008, AJ, 135, 836

Cassisi, S., Castellani, V., Degl'Innocenti, S., Piotto, G., & Salaris, M. 2001, A&A, 366, 578

Chiosi, C. & Carraro, G. 2002, MNRAS, 335, 335

Cioni, M.-R. L., Girardi, L., Marigo, P., & Habing, H. J. 2006, A&A, 448, 77

Coelho, P., Barbuy, B., Meléndez, J., Schiavon, R. P., & Castilho, B. V. 2005, A&A, 443, 735

Coelho, P., Bruzual, G., Charlot, S., et al. 2007, MNRAS, 382, 498

Cole, S., Lacey, C. G., Baugh, C. M., & Frenk, C. S. 2000, MNRAS, 319, 168

Colless, M., Burstein, D., Davies, R. L., et al. 1999, MNRAS, 303, 813

Côté, P., Ferrarese, L., Jordán, A., et al. 2007, ApJ, 671, 1456

Côté, P., Piatek, S., Ferrarese, L., et al. 2006, ApJS, 165, 57

Da Costa, G. S. 1991, in IAU Symposium, Vol. 148, The Magellanic Clouds, ed. R. Haynes & D. Milne, 183–+

Davidge, T. J., Beck, T. L., & McGregor, P. J. 2008, ApJ, 677, 238

Davies, R. I. 2007, MNRAS, 375, 1099

De Lucia, G., Springel, V., White, S. D. M., Croton, D., & Kauffmann, G. 2006, MNRAS, 366, 499

de Zeeuw, P. T., Bureau, M., Emsellem, E., et al. 2002, MNRAS, 329, 513

Decressin, T., Meynet, G., Charbonnel, C., Prantzos, N., & Ekström, S. 2007, A&A, 464, 1029

Denicoló, G., Terlevich, R., Terlevich, E., et al. 2005, MNRAS, 356, 1440

D'Ercole, A., Vesperini, E., D'Antona, F., McMillan, S. L. W., & Recchi, S. 2008, MNRAS, 1228

Dirsch, B., Richtler, T., Geisler, D., et al. 2003, AJ, 125, 1908

Dirsch, B., Richtler, T., Gieren, W. P., & Hilker, M. 2000, A&A, 360, 133

Dubath, P., Meylan, G., & Mayor, M. 1997, A&A, 324, 505

Eisenhauer, F., Abuter, R., Bickert, K., et al. 2003, in Proceedings of the SPIE, ed. M. Iye & A. F. M. Moorwood

Emsellem, E., Cappellari, M., Peletier, R. F., et al. 2004, MNRAS, 352, 721

Emsellem, E., Greusard, D., Combes, F., et al. 2001, A&A, 368, 52

Faber, S. M., Friel, E. D., Burstein, D., & Gaskell, C. M. 1985, ApJS, 57, 711

Falcón-Barroso, J., Bacon, R., Bureau, M., et al. 2006, MNRAS, 369, 529

Ferrarese, L., Côté, P., Dalla Bontà, E., et al. 2006, ApJ, 644, L21

Ferrarese, L. & Merritt, D. 2000, ApJ, 539, L9

Ferraro, F. R., Origlia, L., Testa, V., & Maraston, C. 2004, ApJ, 608, 772

Fingerhut, R. L., McCall, M. L., De Robertis, M., et al. 2003, ApJ, 587, 672

Fioc, M. & Rocca-Volmerange, B. 1997, A&A, 326, 950

Förster Schreiber, N. M. 2000, AJ, 120, 2089

Frogel, J. A., Mould, J., & Blanco, V. M. 1990, ApJ, 352, 96

Frogel, J. A., Persson, S. E., Matthews, K., & Aaronson, M. 1978, ApJ, 220, 75

Frogel, J. A., Stephens, A., Ramírez, S., & DePoy, D. L. 2001, AJ, 122, 1896

Gebhardt, K., Bender, R., Bower, G., et al. 2000, ApJ, 539, L13

Gebhardt, K., Lauer, T. R., Pinkney, J., et al. 2007, ApJ, 671, 1321

González Delgado, R. M., Cerviño, M., Martins, L. P., Leitherer, C., & Hauschildt, P. H. 2005, MNRAS, 357, 945

Gorgas, J., Efstathiou, G., & Aragon Salamanca, A. 1990, MNRAS, 245, 217

Goudfrooij, P., Hansen, L., Jorgensen, H. E., & Norgaard-Nielsen, H. U. 1994, A&AS, 105, 341

Graham, A. W., Colless, M. M., Busarello, G., Zaggia, S., & Longo, G. 1998, A&AS, 133, 325

Grocholski, A. J., Cole, A. A., Sarajedini, A., Geisler, D., & Smith, V. V. 2006, AJ, 132, 1630

Harris, W. E. 2008, in IAU Symposium, Vol. 246, IAU Symposium, 387–393

Houdashelt, M. L., Frogel, J. A., & Cohen, J. G. 1992, AJ, 103, 163

Houghton, R. C. W., Magorrian, J., Sarzi, M., et al. 2006, MNRAS, 367, 2

Hubble, E. 1936, The Realm of the Nebulae (New Haven: Yale University Press)

James, P. A. & Mobasher, B. 1999, MNRAS, 306, 199

James, P. A. & Mobasher, B. 2000, MNRAS, 317, 259

Johnson, J. A., Ivans, I. I., & Stetson, P. B. 2006, ApJ, 640, 801

Jordán, A., Blakeslee, J. P., Côté, P., et al. 2007, ApJS, 169, 213

Kauffmann, G., White, S. D. M., & Guiderdoni, B. 1993, MNRAS, 264, 201

Kawata, D. & Gibson, B. K. 2003, MNRAS, 346, 135

King, I. R. 1966, AJ, 71, 64

Kodama, T. & Arimoto, N. 1997, A&A, 320, 41

Kormendy, J. & Bender, R. 1996, ApJ, 464, L119+

Kormendy, J. & Richstone, D. 1995, ARA& A, 33, 581

Kruijssen, J. M. D. & Lamers, H. J. G. L. M. 2008, A&A, 490, 151

Kuntschner, H. 1998, PhD thesis, University of Durham

Kuntschner, H. 2000, MNRAS, 315, 184

Kuntschner, H. 2004, A&A, 426, 737

Kuntschner, H. & Davies, R. L. 1998, MNRAS, 295, L29+

Kuntschner, H., Emsellem, E., Bacon, R., et al. 2006, MNRAS, 369, 497

Kuntschner, H., Lucey, J. R., Smith, R. J., Hudson, M. J., & Davies, R. L. 2001, MNRAS, 323, 615

Lançon, A. & Mouhcine, M. 2002, A&A, 393, 167

Larson, R. B. 1974, MNRAS, 166, 585

Lauer, T. R., Ajhar, E. A., Byun, Y.-I., et al. 1995, AJ, 110, 2622

Lauer, T. R., Faber, S. M., Gebhardt, K., et al. 2005, AJ, 129, 2138

Lee, Y.-W., Demarque, P., & Zinn, R. 1994, ApJ, 423, 248

Mackey, A. D., Broby Nielsen, P., Ferguson, A. M. N., & Richardson, J. C. 2008, ApJ, 681, L17

Mackey, A. D. & Gilmore, G. F. 2003, MNRAS, 338, 85

Maraston, C. 1998, MNRAS, 300, 872

Maraston, C. 2005, MNRAS, 362, 799

Mármol-Queraltó, E., Cardiel, N., Cenarro, A. J., et al. 2008, A&A, 489, 885

Márquez, I., Masegosa, J., Durret, F., et al. 2003, A&A, 409, 459

McLaughlin, D. E. & van der Marel, R. P. 2005, ApJS, 161, 304

Mieske, S., Hilker, M., Infante, L., & Jordán, A. 2006, AJ, 131, 2442

Mihos, J. C. & Hernquist, L. 1994, ApJ, 437, L47

Milone, A. P., Bedin, L. R., Piotto, G., & Anderson, J. 2008, ArXiv e-prints

Mobasher, B. & James, P. A. 1996, MNRAS, 280, 895

Mobasher, B. & James, P. A. 2000, MNRAS, 316, 507

Modigliani, A., Hummel, W., Abuter, R., et al. 2007, ArXiv Astrophysics e-prints

Mouhcine, M., Rejkuba, M., & Ibata, R. 2007, MNRAS, 381, 873

Mucciarelli, A., Carretta, E., Origlia, L., & Ferraro, F. R. 2008, AJ, 136, 375

Mucciarelli, A., Origlia, L., Ferraro, F. R., Maraston, C., & Testa, V. 2006, ApJ, 646, 939

Munari, U., Sordo, R., Castelli, F., & Zwitter, T. 2005, A&A, 442, 1127

Norris, M. A., Sharples, R. M., & Kuntschner, H. 2006, MNRAS, 367, 815

Nowak, N., Saglia, R. P., Thomas, J., et al. 2008, ArXiv e-prints

O'Connell, R. W., Martin, J. R., Crane, J. D., et al. 2005, ApJ, 635, 305

Oliva, E., Origlia, L., Maiolino, R., & Moorwood, A. F. M. 1999, A&A, 350, 9

Olsen, K. A. G., Hodge, P. W., Mateo, M., et al. 1998, MNRAS, 300, 665

Olszewski, E. W., Schommer, R. A., Suntzeff, N. B., & Harris, H. C. 1991, AJ, 101, 515

Peletier, R. F., Falcón-Barroso, J., Bacon, R., et al. 2007, MNRAS, 379, 445

Persson, S. E., Aaronson, M., Cohen, J. G., Frogel, J. A., & Matthews, K. 1983, ApJ, 266, 105

Pessev, P. M., Goudfrooij, P., Puzia, T. H., & Chandar, R. 2006, AJ, 132, 781

Pinkney, J., Gebhardt, K., Bender, R., et al. 2003, ApJ, 596, 903

Pipino, A., D'Ercole, A., & Matteucci, F. 2008, A&A, 484, 679

Puzia, T. H., Kissler-Patig, M., Thomas, D., et al. 2005, A&A, 439, 997

Puzia, T. H., Saglia, R. P., Kissler-Patig, M., et al. 2002, A&A, 395, 45

Rayner, J. T., Cushing, M. C., & Vacca, W. D. 2007, in preparation

Reda, F. M., Proctor, R. N., Forbes, D. A., Hau, G. K. T., & Larsen, S. S. 2007, MNRAS, 377, 1772

Rejkuba, M., Greggio, L., Harris, W. E., Harris, G. L. H., & Peng, E. W. 2005, ApJ, 631, 262

Renzini, A. 1981, in Galaxy Formation, ed. J. Silk & J. Vittorio, 303

Renzini, A. 1998, AJ, 115, 2459

Renzini, A. & Buzzoni, A. 1986, in Astrophysics and Space Science Library, Vol. 122, Spectral Evolution of Galaxies, ed. C. Chiosi & A. Renzini, 195–231

Renzini, A. & Fusi Pecci, F. 1988, ARA& A, 26, 199

Rousselot, P., Lidman, C., Cuby, J.-G., Moreels, G., & Monnet, G. 2000, A&A, 354, 1134

Saglia, R. P., Kronawitter, A., Gerhard, O., & Bender, R. 2000, AJ, 119, 153

Sánchez-Blázquez, P., Forbes, D. A., Strader, J., Brodie, J., & Proctor, R. 2007, MNRAS, 377, 759

Sánchez-Blázquez, P., Gorgas, J., Cardiel, N., & González, J. J. 2006, A&A, 457, 787

Schiavon, R. P. 2007, ApJS, 171, 146

Schweizer, F. 1989, in Dynamics and Interactions of Galaxies, ed. R. Wielen (New York: Springer), 60

Searle, L., Wilkinson, A., & Bagnuolo, W. G. 1980, ApJ, 239, 803

Silva, D. R. & Bothun, G. D. 1998a, AJ, 116, 85

Silva, D. R. & Bothun, G. D. 1998b, AJ, 116, 2793

Silva, D. R., Kuntschner, H., & Lyubenova, M. 2008, ApJ, 674, 194

Simien, F. & Prugniel, P. 1997, A&AS, 126, 519

Simien, F. & Prugniel, P. 2002, A&A, 384, 371

Skrutskie, M. F., Cutri, R. M., Stiening, R., et al. 2006, AJ, 131, 1163

Smith, R. J., Lucey, J. R., Hudson, M. J., Schlegel, D. J., & Davies, R. L. 2000, MNRAS, 313, 469

Steinmetz, M. & Navarro, J. F. 2002, New Astronomy, 7, 155

Stoehr, F., Fraquelli, D., Kamp, I., et al. 2007, Space Telescope European Coordinating Facility Newsletter, Volume 42, p.4, 42, 4

Thomas, D. 1999, MNRAS, 306, 655

Thomas, D., Maraston, C., & Bender, R. 2003, MNRAS, 339, 897

Thomas, D., Maraston, C., Bender, R., & Mendes de Oliveira, C. 2005, ApJ, 621, 673

Thomas, D., Maraston, C., & Korn, A. 2004, MNRAS, 351, L19

Tinsley, B. M. 1980, Fundamentals of Cosmic Physics, 5, 287

Tinsley, B. M. & Gunn, J. E. 1976, ApJ, 203, 52

Toomre, A. 1977, in The evolution of Galaxies and Stellar Populations, ed. B. M. Tinsley & R. B. Larson (New Haven: Yale University Press), 401

Trager, S. C., Faber, S. M., Worthey, G., & González, J. J. 2000, AJ, 119, 1645

Trager, S. C., Worthey, G., Faber, S. M., Burstein, D., & Gonzalez, J. J. 1998, ApJS, 116, 1

van den Bergh, S. 1998, PASP, 110, 1377

van Dokkum, P. G. & Franx, M. 1995, AJ, 110, 2027

Vazdekis, A. & Arimoto, N. 1999, ApJ, 525, 144

Vazdekis, A., Casuso, E., Peletier, R. F., & Beckman, J. E. 1996, ApJS, 106, 307

Ventura, P., D'Antona, F., & Mazzitelli, I. 2002, A&A, 393, 215

Wehner, E. H. & Harris, W. E. 2006, ApJ, 644, L17

White, S. D. M. 1980, MNRAS, 191, 1P

Wilson, C. P. 1975, AJ, 80, 175

Worthey, G. 1994, ApJS, 95, 107

Worthey, G., Faber, S. M., & Gonzalez, J. J. 1992, ApJ, 398, 69

Worthey, G., Faber, S. M., Gonzalez, J. J., & Burstein, D. 1994, ApJS, 94, 687

Wozniak, H. & Champavert, N. 2006, MNRAS, 369, 853

Wozniak, H., Combes, F., Emsellem, E., & Friedli, D. 2003, A&A, 409, 469

Zaritsky, D., Harris, J., & Thompson, I. 1997, AJ, 114, 1002

Zhang, F., Li, L., & Han, Z. 2005, MNRAS, 364, 503

Acknowledgements

First of all I would like to thank my supervisors Harald Kuntschner and David R. Silva for their support and invaluable guidance over the last three years, for offering me the opportunity to explore such an exciting field of modern astrophysics, for always being there to answer my questions, and for their endless patience in improving my writing.

I would also like to express my gratitude to Marina Rejkuba for providing me with moral support, valuable source of ideas, and being such a nice person. I am indebted to Markus Kissler-Patig, my first ESO supervisor, for showing me the excitement of scientific research. I am also grateful for the many useful discussions on various topics to Andrés Jordán, Karina Kjaer, Steffen Miske, Maria-Rosa Cioni, Bruno Leibundgut, Claudia Maraston, Daniel Thomas, and many others.

These three years in Munich would not have been the same without Karina, Michael, Daniela, Marcelo, my Slavic souls Anna, Yuri and Jarek. Thanks to my most recent colleagues, Ana, Giuseppina, Iva, Nadine, and Silvia for their warm words.

I would like to thank my family for their continuous support and trust in me. I am happy that I fulfilled my father's dream.

Finally, I would like to thank my husband Lyubomir for his immense love and patience, for encouraging me and following my way to the stars.